A.A. 2004/2005

Università degli studi di Roma
"Tor Vergata"

The Sun: dynamics and topology in the upper convection layer.

January 2005

Thesis Author:
Dott. Dario Del Moro

Thesis Advisor:
Prof. Francesco Berrilli

Thesis Coordinator:
Prof. Roberto Buonanno

A thesis submitted to
The University of Rome “Tor Vergata”
in partial fulfillment of the requirements for the degree
of
Doctor of Philosophy in Astronomy.

Version 1.2

Contents

List of Figures

List of Tables

Acknowledgements

While writing this thesis I realized to be in debt with many, many people.
Then I realized that most probably I was still forgetting someone...
Thank you all, especially the ones I forgot!
In particular, I would like to acknowledge the help of some special persons.

As my thesis advisor, Prof. Francesco Berrilli introduced me to solar physics research and then encouraged my professional self-direction without interferences, just a nudge here and there to prevent me going too far astray.

In "Tor Vergata" University solar group my knowledge of solar physics was greatly extended by the teaching of Prof. Alberto Egidi and Prof. Bruno Caccin.
Bruno, we miss you so much and we do hope you found something very interesting to study there.

Many thanks to Dr^2. Valentina Penza for great assistance on solar line formation and, above all, for being a so kind and bright friend of mine, one with whom I can share many and many good talks.

I want to acknowledge support and great patience from Dr. Silvia Giordano, quasi-Dr. Bartolomeo Viticchié and Dr. Stefano Russo, for helping me with a lot of work, substituting me for teaching when I was in need and for bearing my inexcusable manners.
These three guys have recently (or probably would in a short time) embarked on a very mistaken activity: I want to warn them that no-one knows how much harm a Ph.D. course can do to you!

I would also give a special thank you to Dr. Giuseppe Consolini, who always has been willing to share his viewpoint on scientific and professional matters and spent a lot of his time working for me, often, as he himself would says, 'fighting the burocracy'.

I am also grateful to Dr. Arnaldo Florio for fruit-ful discussions on complexity, for chocolate-ful discussions on chaos and alcohol-ful discussions on Murphy's laws.

I acknowledge the massive amount of work of Dr. Ermanno Pietropaolo, who introduced me to wavelets and other delights, reduced part of the data used in this thesis, but still, I regret, did not fulfill his promise. But I am a patient guy and I will wait.

Special thanks to the CVS crew at Monte Porzio OAR, especially Mauro Centrone, Dr. Fabrizio Giorgi and Dr. Corrado Perna for a lot of good time spent together.

I would be, of course, forever in debt with my parents, Federico Del Moro and Angela Gasparini, for unwavering financial support and lodging!
Special thanks also to my brother Carlo, for his patience in putting up with me for all these long years. Maybe one day we will discuss about this topic, if he will be able to read it!

I have also to acknowledge a special collaboration from Dr. Andrea De Gaetano and Dr^2. Valerio D'Elia: thank you for leaving me enough spare time to finish my thesis.

Very special thanks to Viviana Rempicci and Alessandro Pieralisi for being the best friends one could hope to have (OK, maybe I'm exaggerating, but just a little bit).

Of my time spent in Tenerife I have lots of beautiful memories:
I absolutely must acknowledge the support, the teaching and the friendship of Prof. Guido Ceppatelli and Dr. Giovanni Mainella: they showed me how to perform sensible observations, how to work with solar telescopes and introduced me to the most fascinating topic of discovering the island hidden treasures.

I did deeply appreciate all the time spent at IAC with Prof. Jose Antonio Bonet Navarro as a teacher, and, if possible, I appreciated even more the time spent with him as a friend. Dear Antonio, I owe you a lot, and, particularly for this thesis, I owe you the SVST95 dataset!

I would not forget Prof. Inez Márquez Rodriguez for interesting conversations about music and mathematics and for a few good dinners had together with me and Antonio!

Sincere thanks to Dr. Carine Briand for all the explanations she gave me.

At HAO I enjoyed the interest and the insight of Dr. Mark Peter Rast about my work: we probably would have slept there if it weren't for the shuttle leaving at 18.00.
By the way, Figure 1.3 is Mark's.
I wish also to thank Christie, Jacob, Luke, Zack and Rosemary for a charming Thanksgiving dinner. Please, tell them.

All my appreciation to Prof. Fabio Cavallini for the IPM and the IBIS: they are two marvelous instruments.

I am cosmically grateful for their creations to Therry Pratchett and Neil Gaiman, and not exclusively for what they did together.

I thank Dr. Gianna Cauzzi, Prof. Luigi Smaldone and Dr. Thomas Straus for the NSO96 dataset.
I thank Prof. Alexander Kosovichev and Prof. Thomas Duvall for the MDI-SOHO helioseismological dataset.
I acknowledge Prof. Vittorio Castellani a very deep insight on stars, and I guess I am not the only one. I thank him for the knowledge.
I acknowledge Prof. Giuliano Natali a very deep insight on telescopes. I thank him for the knowledge and I guess I could be the only one.
I acknowledge Figure 1.1 by Prof. Åke Nordlund.
I acknowledge Figures 2.1, 2.2, 2.3, 2.4 and 2.5 have been obtained from spectral syntheses performed by Dr. Valentina Penza.
I acknowledge Figures 2.6 and 2.7 by Prof. Fabio Cavallini.

Special thank also to the THEMIS crew and to NSO-Sacramento Peak observatory crew, in particular to Dough for his kindness and user-friendliness.

The THEMIS is operated on the island of Tenerife by CNRS and CNR in the Spanish Observatorio del Teide of the Instituto de Astrofsica de Canarias.
The Dunn Solar Telescope is operated by the Association of Universities for Research in Astronomy, Inc. (AURA) at the National Solar Observatory in Sacramento Peak (New Mexico).
The Swedish Vacuum Solar Telescope is operated on the island of La Palma by the Royal Swedish Academy of Science in the Spanish Observatorio del Roque de Los Muchachos of the Instituto de Astrofisica de Canarias.
I was supported partially by the Italian National Research Council (CNR) grant Agenzia2000 CNRC0084C4 and by the MIUR grant COFIN02.

I also acknowledge Dr. Serena Criscuoli's support, but this will be discussed privately.

Abstract

Observation of the solar photosphere and explanation of its appearance has been a major field of research for many years. Only recently, observation techniques have improved to allow high resolution studies in time, space and wavelength. Such observations revealed that the solar surface consists of a hierarchy of interacting MHD structures with highly dynamic patterning. The understanding of global and local properties of the convective solar layer is essential to comprehend how the energy transfer process is modified by magnetic field and to precisely evaluate the upper and lower overshooting zones extent to improve our comprehension of stellar evolution. Moreover, photospheric motions have a major role in the process of energy and mass injection from low solar atmosphere to corona, since the advection of magnetic foot-points by photospheric plasma flows strongly affects coronal organization. Lastly, the spatial configuration of the magnetic field elements on solar surface is produced by the interaction of the magnetic field with photospheric convective motions; therefore changes of the conditions in the convective layer are probably linked to solar irradiance variation trough the solar magnetic cycle. The analysis of surface patterns allows the characterization of their topology and morphology in order to determine the convective regime and system dynamic parameters. In order to achieve a complete and reliable analysis, unbiased image segmentation procedures and topology characterizing functions are needed.

This thesis thus consists of an investigation on the dynamics of photospheric mass motions and on the topology of magnetic field elements.

An introduction to solar convective flows is presented in Chapter 1, illustrating recent models of convection at high Reynolds number and their relevance to the hierarchy of flow pattern of the solar surface. The traditional classification and explanation of such patterns are presented, as well as possible new interpretations. Chapter 2 introduces the reader to up-to-date techniques of solar spectral imaging. In particular, in the first part of the chapter, the theory of line spectroscopy will be introduced, in order to discuss, later in the same chapter, the basic concept and the layout of the IPM and IBIS 2-D spectrographs. In chapter 3, the Phase Diversity technique, able to minimize seeing induced distortion on acquired image, will be described. Chapter 4 is an introduction to helioseismological techniques and, in particular, to time-distance local helioseismology. Chapter 5 specifically discusses solar image analysis, giving details on feature segmentation and local correlation techniques. Several techniques of structure recognition and tracking are presented and confronted. In Chapter 6 some results of the study of the solar photosphere and, in particular, of the solar surface magnetic field via spectroscopic analysis of solar lines are presented. The basic theory of functions suitable to probe the existence of structural organization is presented in Chapter 7, with emphasis on the Pair Correlation Function and on the Normalized Van Siclen's Entropy. In Chapter 8 we discuss the presented results and state our conclusions.

0.1 Forewords

This thesis presents the research works I performed during the three years of my 'Dottorato di Ricerca in Astronomia, XVII ciclo' in the Rome "Tor Vergata" University.

In these years, under the aware supervision of Prof. F. Berrilli, I principally investigated the solar photosphere structure and dynamics, using many different points of view and applying many different tools, developing collaborations with several colleagues in Europe and USA. Actually, my research led me to observe and study in several astronomical observatories and institutions, both in Italy and abroad. In particular, I had the opportunity to stay almost a year in Tenerife, observing and developing instrumentation in THEMIS (Heliographic Telescope for Solar Magnetism and Instabilities Studies at Teide Observatory, Spain) and a couple of months in the USA, observing at DST (Dunn Solar Telescope at Sacramento Peak, New Mexico) and working at HAO (High Altitude Observatory).
I also acknowledge productive collaborations with Dr. G. Consolini at IFSI (Institute for Interplanetary Space Physics) and Dr. V. Penza and Dr. S. Criscuoli at INAF (National Institute for Astrophysics)

In order to tackle the appealing subject of the nature of solar surface convection, I had in mind to adapt some analysis tools, usually employed in other research fields (matter physics, computer vision…), to obtain some new results about solar photosphere. Therefore, during these years, I developed some procedures able to objectively detect solar photospheric features and some others able to analyze their properties.

One of the most useful tools a solar observer can employ is, no surprise, light. By means of spectroscopic analysis, it is possible to recover the line-of-sight velocity of the emitting matter, i.e., at solar disc centre, the vertical velocity of solar surface structures. And, as wavelength can be somehow translated to depth in the solar atmosphere, I saw the possibility to transform a bidimensional image in a 3-D field. Obtaining a high spectral resolution was, therefore, a must. And, as a consequence, it was compulsory to understand the concept and implementation of tuneable filters and come to terms with the theory of line formations.
Unfortunately, the tunable filters tend to be a little 'obscure', that is, not transparent. As a consequence, image integration times were longer, degrading the image quality. Moreover, their complex optical set-up may limit your field of view. I observed several times at THEMIS with the IPM (Italian Panoramic Monochromator) instrument, obtaining some excellent images. Applying the TST (Two-level Structure Tracking) procedure to THEMIS data, I tested and gauged my analysis tools and obtained some interesting results presented in this thesis.

In the mean time, I was performing observations, developing a new insight in this topic, enjoying the guidance and the support of Prof. G. Ceppatelli and Dr. G. Mainella. Experience led me to the conclusion that observation quality was a major part in a good research work. Therefore, I lernt the basics (and, hopefully, something more) on image restoration, information transmission and

Fourier optics. More, I witnessed the data quality that can be reached by Phase-Diversity restoration of seeing-degraded images.
As a consequence, I tried myself to implement a Phase-Diversity set-up at THEMIS secondary focus and developed a modified software to account for the telescope's characteristics. I obtained some promising results, a few high quality images and a somewhat accurate estimation of the telescope optics aberration. Furthermore, the understanding and the know-how collected in this experience helped me in several other tasks, above all in image restoring.

Additionally, during the time spent in Tenerife observing, studying and working on Phase-Diversity, I had the privilege to establish a stable collaboration with Prof. J.A. Bonet in the IAC (Instituto de Astrofisica de Canarias), who gave me the opportunity to verify the stability of the 'apparatus' I was developing on an exceptional granulation time series from SVST (Swedish Vacuum Solar Tower), and thus to obtain some more results, presented in this thesis, too.

As something unexpected, it came a collaboration with a Prof. A. Kosovichev's helioseismological group and an analysis on a helioseismology dataset. Again, the fee was some more study to understand how could they measure solar supergranulation a couple of megameters below the solar surface, but it was a good benchmark for my toolset and, again, I present some results of this investigation in this thesis.

In the Fall of 2003 I had the possibility to observe at DST telescope using the new 'IBIS' (Interferometric BIdimensional Spectrometer). This observation run bestowed me with a large and promising amount of data to reduce and some extra study to understand the quite complex instrument.
In this thesis, I also present some preliminary results of an analysis carried out using part of this dataset and, to my knowledge, the very first 3-D velocity field of the plasma motions in the solar photosphere. In particular, a fraction of this analysis has been performed during my visit at the HAO, in the very last months of my Ph.D., hosted by Prof. M.P. Rast.

Chapter 1

Solar convection

The exact structure of the convective zone of the Sun is not known because it cannot be directly observed. Our understanding of solar convection derives from optical observations of the surface, from helioseismological observations of the interior, and from theories and simulation of compressible convection. In the last years, major progresses have been attained in all these fields. In this chapter we will introduce the reader to recent results of the theories and simulations of compressible convection and to new conclusions on convective patterns obtained from solar photosphere observations.

1.1 Theory

1.1.1 Convection onset

The reason of the convective instability is the buoyancy provided by plasma density fluctuations in the deeper layers of the Sun. This buoyant force onsets matter upflows which rise to the surface and overshoot into the photospheric layers producing several observable features as temperature gradients, line of sight velocities and divergences (Bray et al., 1984; Spruit et al., 1990). The Rayleigh-Bénard convection theory, though superseded in later years (Pearson, 1958), has played a crucial role in guiding both theories and experiments towards the comprehension of the complex dynamics arising in dissipative (i.e. far-from-equilibrium) systems (Cross and Hohenberg, 1993; Chiam et al., 2003). In the Rayleigh-Bénard scheme, a viscous fluid heated from the bottom and cooled at the top in a gravitational field, produces a Bénard pattern due to the organization of convective cells into a lattice-like arrangement. But the formation of the cells does not automatically ensue. In fact, the convection onset depends on the fluid physical properties and depth, and on the temperature gradient. In other words, the fluid remains homogeneous (spatial invariance) and steady (temporal invariance) until some critical conditions are fulfilled. Actually, the onset of convection must cope with at least two more modes of energy dissipation: 1) The thermal conductive transfer between the warmer rising matter and the surrounding matter, that reduces the temperature difference and therefore density difference; 2) The viscous drag between the rising fluid and the surrounding fluid. In order to guarantee convective flow onset, it is required that the buoyant force, produced by temperature gradient, exceeds the dissipative

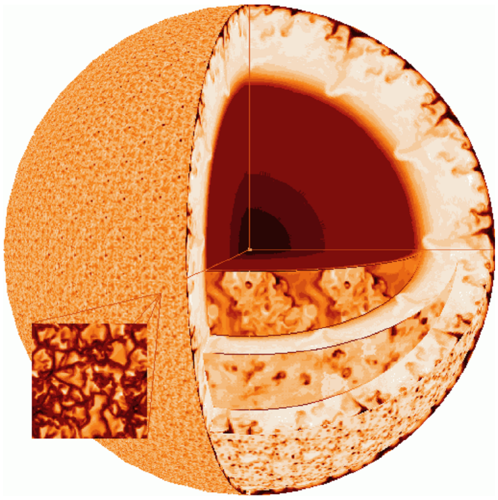

Figure 1.1: Simulation of solar convection by Å. Nordlund.

forces of heat diffusion and viscous drag by a critical amount. The fluid condition can be quantitatively described by a non-dimensional number R, called Rayleigh Number, which is the ratio of buoyant force to heat diffusion rate and viscous drag.

$$R = \frac{\mathrm{g}\alpha d^3 \Delta \mathrm{T}}{\nu\kappa} \tag{1.1}$$

where g is the acceleration of gravity, α is the coefficient of thermal expansion, d is the vertical length scale, ΔT is the temperature difference between the planes, ν is the *kinematic* viscosity and κ the thermal diffusivity. When R exceeds a critical value R_c, convection occurs. Therefore, the Rayleigh Number essentially measures when the energy transport switches from conductive to convective. The efficiency of convective heat transport with respect to thermal diffusion is represented by another adimensional number: the Nusselt number N_u.

$$N_u = \frac{F_{conv}}{F_{diff}(\bar{v} = 0)} \tag{1.2}$$

For the inner Sun R is about 10^{23} and whenever convection occurs, it becomes the dominant heat transport mechanism by far.

The standard criterion adopted to study convective instabilities in a stellar interior derives from the *blob theory* that considers fluctuations from an average state (Schüssler, 2002). When considering rising matter packets (blobs), we can define three different characteristic times related to three different blob physical properties:

- Blob timescale: $\tau_i = d/v$
- Thermal timescale: $\tau_{th} = (c/\sigma)d^2$
- Dynamical timescale: $\tau_{dyn} = d/c_s$

where d is the typical dimension of the blob, v is the blob vertical velocity, c is the specific heat, σ is the thermal conductivity, and c_s is the speed of sound.

Figure 1.2: Spiral waves in a Belousov-Zhabotinsky reaction.

Since in the interior of the Sun the following relations hold:

$$\tau_i << \tau_{th}$$
$$\tau_i >> \tau_{dyn}$$

we can assume that convective elements rise adiabatically and in pressure equilibrium with the surroundings.

Therefore,

$$S_i = S_i^*$$
$$P_i = P_i^*$$

where S_i and S_i^* are the entropies of the surroundings and the blob, respectively, while P_i and P_i^* are the pressures of the surroundings and the blob, respectively. The instability follows from the request $\rho_i = \rho_i^*$.
By including the equation of state for the plasma in this latter relation, we obtain the *Ledoux* criterion for dynamic instability:

$$\frac{dT}{dr} < \left(\frac{dT}{dr}\right)_{ad} + \frac{T}{\mu}\left[\frac{d\mu}{dr} - \left(\frac{d\mu}{dr}\right)_{ad}\right] \tag{1.3}$$

In case of homogenous chemical composition, i.e.$\frac{d\mu}{dr} = 0$, the *Ledoux* criterion reduces to the more known *Schwarzschild* criterion.

$$\frac{dT}{dr} < \left(\frac{dT}{dr}\right)_{ad} \tag{1.4}$$

But for a few exceptions, both criteria can be applied using local P, T, and ρ without considering the rest of the star (Kippenhahn and Weigert, 1994)). These instability criteria, while describing the conditions required for convective motion onset in the solar deeper layers, cannot account for the observed convective features emerging at solar surface. In fact, when R_c is exceeded and the convective instability sets in, the system *reacts* to the simultaneous attempts of hot layers to rise and of cold layers to sink, separating itself into a pattern of convective cells. At small spatial scale, single plasma particles move quite randomly, though, large scale correlation among particle movements emerges and convective cells exhibit a statistical average behaviour. The origin of *interesting forms* in such dissipative systems, as for example the coloured spirals of Belusov and Zabotinski (Figure 1.2) in chemical reactions or the patterns obtained by numerical simulation of Rayleigh-Bénard convection (Chiam et al., 2003), demands elaborated models of pattern formation (Prigogine and Kondepudi, 2002; Cross and Hohenberg, 1993) in order to be interpreted.

For our purpose, it is central to notice that these systems show a macroscopic order (i.e. spatial correlations) and the initial spatial invariance, or symmetry, is lost. This suggests the existence of correlations, i.e., of statistically reproducible relations between distant parts of the system (Nicolis, 1989).

1.1.2 Convective regimes

We have introduced the concept of the Rayleigh number R as describer of the physical system status for what concerns convection. As R increases, the system undergoes rapid changes in heat conduction efficiency and in flow complexity. Roughly speaking, as R increases the system develops more and more 'disorder'.

The Kolmogorov's theory of turbulence recognizes five flow patterns: still, steady convection, periodic convection, chaotic convection and turbulent convection.

Since the late 1980s, a series of experiments with gaseous and liquid Helium (Libchaber, 1987; Chavanne et al., 2001), led to a revision of the turbulence theory and to the splitting of Kolmogorov's turbulent convection into 'soft' turbulence and 'hard' turbulence (Glazier et al., 1999). The soft turbulence regime is reached as R exceeds 10^5 and is characterized by a power law relation between R and N_u: $N_u \propto R^{1/3}$. The hard turbulence regime starts at $R \sim 10^8$ and a ratio $N_u \propto R^{2/7}$ is expected. Recent studies by Siggia (1994) suggest that increasing further R, a new regime of *ultra*-hard turbulence would be reached (Chavanne et al., 1997). The existence of such a regime would have major consequences in thermal transport in stars (Glazier et al., 1999).

At present time the highest R values reached in laboratory do not go beyond 10^{14}-10^{15} and are still several order of magnitude below the values we expect in stellar interior. In addition, such experiments can not achieve realistic physical properties of stellar structure, as stratification and boundaries conditions. Nevertheless, a complete understanding of convective turbulence would have considerable relevance in astrophysics, as discussed by Spruit (1997).

Advances in parallel computing, numerical algorithms and data storage are such that direct numerical simulations of a full three-dimensional time dependent convection are feasible for experimentally realistic situations. So, numerical simulations have been performed, reproducing the laboratory experiment conditions, in order to study the fluid convection in all its details (Kerr, 1996). These simulations agreed closely with experiments and revealed the *thready* nature of convective flow at very high R (Nordlund and Stein, 1995; Nordlund et al., 1997; Spruit, 1997). They suggest that solar convection is instead driven on the scale of granulation by radiative cooling at the stellar surface. This process generates thin, cool downdrafts that descend through smooth upflows and merge as they traverse the convection zone.

Such results imply that the concept of turbulent convection in stellar convective zones as a Kolmogorov's cascade is eventually wrong, despite the success of Mixing Length Theory (MLT) (Canuto and Mazzitelli, 1991, 1992; Ludwig et al., 1999; Palmieri et al., 2002) in reproducing the convective energy transport in

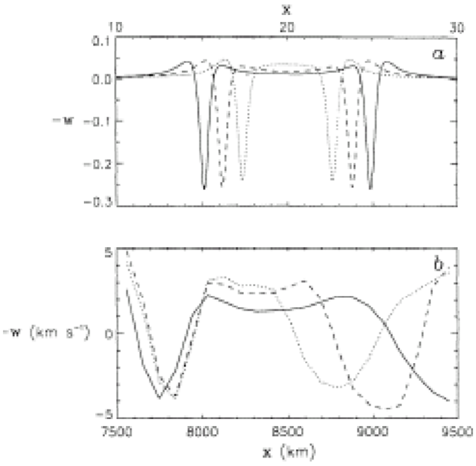

Figure 1.3: (a) Vertical velocity along a horizontal cut through three 2-D compressible two-plume simulations of increasing plume separation and equal plume strength. (b) Horizontal cuts of photospheric vertical velocity across an expanding granule at three successive times from 3-D hydrodynamic simulation by Stein and Nordlund (1989). Figures from Rast (2003a).

stellar models. MLT was adapted to astrophysical settings by (Biermann, 1948; Vitense, 1953; Böhm-Vitense, 1958) and has enjoyed widespread acceptance as a model for calculating the structure of stellar convection zones. Nevertheless, MLT gives no information on dynamic phenomena, such as penetration and mixing into adjacent stable layers, or on the correlation of dynamic properties inside the convection zone and cannot adequately describe the upper and lower overshooting from convection zones.

Instead, the new insight of solar convection reveals coherent plasma structures (threads, plumes, thermals) in turbulent convection, connecting the topmost and bottommost layers of a stellar convective zone. More in detail, coherent plasma features would be responsible for heat exchange, by crossing the entire convective region, while the bulk of the fluid remains essentially passive and has near-zero temperature fluctuations. Such downdraft may overshoot deeply in the radiative transport layer dramatically affecting the stellar evolution. Moreover, adiabatic 2D numerical simulations showed that whenever the distance between two adjacent downward plumes exceeds a critical limit, a new plume spontaneously forms in between (Rast, 1999, 2003a). Therefore, the typical gap between plumes would be related to the distance over which downflow induced pressure fluctuations drive upward convective heat transport at a level sufficient to sustain the radiative cooling of the surface. Such a downflow behaviour imposes some order to the turbulent flow, stimulating the formation of organization and visible patterns.

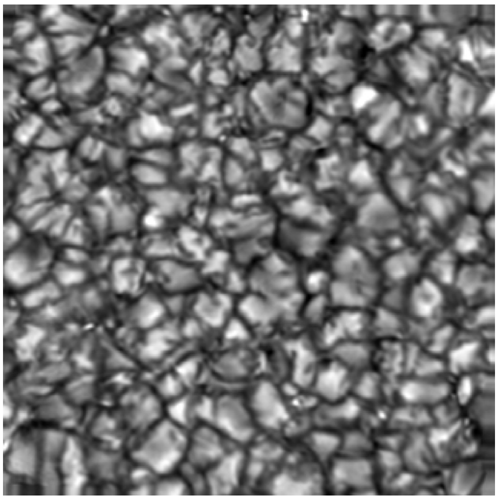

Figure 1.4: Solar granulation as observed with the 50 cm Swedish Vacuum Solar Telescope on the island of La Palma, Spain, in 1995.

1.2 Observations

1.2.1 The solar photospheric velocity fields hierarchy

The observed hierarchy of solar photospheric velocity fields is thought to be the direct manifestation of the convective plasma motion in the lower layers.

In order to comprehend how turbulent convection transports energy and momentum in the solar upper layers, it is essential to study and understand both the dynamic and the origin of these outflow patterns.

The traditional classification of such patterns distinguishes between granulation (typically ∼5 minutes time scale and ∼1 Mm spatial scale), mesogranulation (typically ∼1 hour time scale and ∼5 Mm spatial scale) and supergranulation (typically ∼24 hour time scale and ∼30 Mm spatial scale).

Granulation (Figure 1.4) was discovered long ago by Herschel (1801) and identified as convection by Unsöld (1930). It is in fact the only one of these patterns for which a correlation between intensity and velocity patterns, and thus a direct verification of its convective origin, has been unambiguously provided (Richardson and Schwarzchild, 1950; Stuart and Rush, 1954; Plaskett, 1954; Leighton et al., 1962; Canfield and Mehltretter, 1973). High-resolution observations of continuum intensity (de Boer et al., 1992; Wilken et al., 1997; Hirzberger et al., 1997, 2002) and Doppler velocity (Nesis et al., 1992, 1993, 1997; Krieg et al., 2000; Berrilli et al., 2001; Hirzberger et al., 2002) indicate that granules consist of an ascending part, flowing seemingly in laminar regime, surrounded by more turbulent downflow lanes. However, the detailed structure of granulation is not as simple as suggested by its convective origin. Single granules vary in size and shape from nearly circular blotches to elongated and bent curls, showing a broad distribution of areas, ranging from 2 Mm^2 down to current resolution limits.

The analysis of granule internal structure revealed that the brightness peak is often localized near the border, rather than near the centre, as expected for 'classic' convective features. It is the upflow associated with these bright borders which penetrates into the higher photospheric layers (Wilken et al., 1997). Its velocity seems to decrease linearly from 1.0 km·s^{-1} at the basis of the photosphere to zero at about 250 km of height (Keil, 1980b,a; Berrilli et al., 2001). Conversely, the downflows seem to be more intense and coherent, with typical vertical velocities of $\sim$2.0 km·s^{-1} at the basis of the photosphere. As discussed in section 1.1.2, these downflows are thought to organize below the solar surface in threads and plumes, possibly reaching the other end of the convective layer (Spruit, 1997).

Neither the temporal evolution of granulation is simple as suggested by its convective origin. Most granules (85% (Hirzberger et al., 1999a)) are produced by fragmentation of previous granules and all the others (13% (Hirzberger et al., 1999a)) by merging. Many granules (40% (Dialetis et al., 1986); 31.2% (Hirzberger et al., 1999a)) evolve by expansion, central darkening and fragmentation through the formation of dark lanes (Rösch, 1959; Rösch and Hugon, 1959; Carlier et al., 1968; Namba and Diemel, 1969; Mehltretter, 1978; Kitai and Kawaguchi, 1979; Kawaguchi, 1980; Bray et al., 1984; Namba, 1986; Hirzberger et al., 1999b).

If such a fragmentation process occurs quickly and vigorously (expansion to 3"–5" in $\sim$8 minutes, with radial velocities up to 1.5 km·s^{-1}) the granule is defined an 'exploding' granule.

The origin and even existence of mesogranulation is still an open topic. It was first reported in time-averaged disk-centre Doppler images (November et al., 1981) but it was extensively studied only after the introduction of correlation tracking of granular features: mesogranulation is indeed easily detected in horizontal flow divergence maps (November and Simon, 1988; November, 1989; Muller et al., 1992; Roudier et al., 1998; Ueno and Kitai, 1998a,b; Shine et al., 2000).

In order to sustain such horizontal flows, associated vertical flows of the order of 50 m·s^{-1} are ascribed to mesogranulation. Reported sizes for mesogranular cell diameters range from 3 to 8 Mm, lasting for few hours (Title et al., 1989; Roudier et al., 1998, 1999). The spectral analyses of photospheric Doppler velocity fields in order to recover the spectral signature of mesogranulation are, however, uncertain.

Most power spectra analyses do not reveal a distinct mesogranular scale (Wang and Zirin, 1989; Chou et al., 1991; Straus et al., 1992; Straus and Bonaccini, 1997; Hathaway et al., 2000), but a continuum of scales from granulation to supergranulation sizes.

Conversely, Ginet and Simon (1992) stated that a mesogranular component is required to reproduce the power distribution in a solar model. Successively, others succeeded in reproducing the spectral shape by employing only granular and supergranular scale motions (Straus et al., 1992; Hathaway et al., 2000).

The analysis of the correlation of mesogranular intensity fluctuations with mesogranular vertical velocity provided indications consistent with convection (Deubner, 1989; Straus et al., 1992), but due to this unclear range separation it was impossible to discern whether these were produced by the broad granular distribution or by a distinct scale.

Numerous observations report that granule properties vary on mesogranular

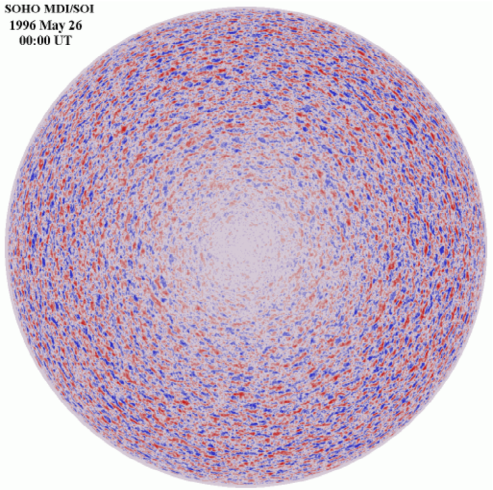

Figure 1.5: Solar supergranulation as observed with the MDI instrument on SOHO on May, 26 1996.

scales (Oda, 1984; Dialetis et al., 1988; Title et al., 1989; Muller et al., 1990; Brandt et al., 1991; Abdussamatov, 1993, 2000; Abdussamatov and Zlatopolo'skii, 1997; Hoekzema and Brandt, 2000; Müller et al., 2001). Such observations are usually drawn on to infer that granular dynamics are influenced by the underlying mesogranular flow. An alternative interpretation could be that mesogranulation is just an effect of granulation, creating a secondary spatial scale by cooperative organization (Rast, 1995, 1999; Rieutord et al., 2000; Müller et al., 2001; Cattaneo et al., 2001).

The solar supergranulation has been discovered by self-correlating solar dopplergrams (Hart, 1954, 1956) and it has been studied since by observations of its horizontal and vertical flow components.

Full disc Doppler imaging clearly reveals the supergranulation vertical velocity pattern, while its horizontal counterpart is detected either by direct Doppler measurements away from disk centre (Leighton et al., 1962; Deubner, 1971; Giovanelli, 1980; Rimmele and Schroeter, 1989; Srikanth et al., 2000; Hathaway et al., 2002) or, near disk centre, by tracking the advection of magnetic elements or smaller scale flows (Simon, 1967; November and Simon, 1988; Simon et al., 1988; Wang and Zirin, 1989; Muller et al., 1992; November, 1994; Wang et al., 1996; Zhang et al., 1998b,a; Roudier et al., 1999; De Rosa et al., 2000; Shine et al., 2000; Lisle et al., 2000). Such studies revealed an advection flow from the centre of the supergranules to their periphery of $\sim$400 $\text{m}\cdot\text{s}^{-1}$.

The supergranular flow pattern is outlined by strong photospheric magnetic fields and chromospheric network (Simon and Leighton, 1964). Such network boundaries are incomplete, with discontinuous sites of high magnetic flux density generally associated to strong flow convergence sites, situated at the vertexes of supergranular cells.

Velocity measurements near the cell boundary are complicated by the presence of such strong magnetic fields (Schrijver et al., 1997; De Rosa et al., 2000;

Berrilli et al., 1999). Spatially intermittent downflows at supergranular boundaries have been reported with amplitudes ranging from tens to hundreds of meters per second (Frazier, 1970; Musman and Rust, 1970; Deubner, 1971; Skumanich et al., 1975a; Worden and Simon, 1976; Giovanelli and Slaughter, 1978; Küveler, 1983; Wang and Zirin, 1989; Hathaway et al., 2002). However, such results remain not conclusive due to the spectral line distortions caused by the presence of magnetic fields (Miller et al., 1984; Stenflo et al., 1984; Solanki and Stenflo, 1984; Stenflo and Harvey, 1985).

A different approach to the detection of supergranulation was employed by Kosovichev et al. (2001), by inverting time-distance helioseismology measurements. They probed a layer a few megameters deep, retrieving the horizontal divergence beneath the solar surface, clearly displaying a flow pattern congruent with supergranulation.

Applying another inversion technique, Zhao and Kosovichev (2003) also measured convergent flows at depth $\sim$10 Mm, therefore concluding that supergranules are cellular convective structures with an estimated average depth of 15 Mm.

1.2.2 Granulation: surface convection

Small scale convective features occurring on the solar surface (i.e. the granulation phenomenon) can be explained by this physical framework: the granular pattern is driven by strong downward features, possibly consequence of hydrodynamic Rayleigh-Taylor instabilities taking place at the top of the photosphere.

In these layers colder collapsing matter is smoothly replaced by warm plasma; therefore borders between upward and downward plasma features develop into strong shear layers where small scale turbulence is concentrated, mainly below the resolution limit (Nesis et al., 1997).

Granule size is determined by the positions of downward plumes bordering the upward feature. It is opinion of several authors that small scale downflows associated to granules provide the driving force for larger scale flows (Spruit, 1997; Rast, 2003b).

As a consequence, the usual picture of hot bubbles arising from lower layers is no longer correct.

In recent years, a considerable amount of fully compressible convection numerical simulations has been performed in order to reproduce and understand observed granular features (see Gadun et al., 2000, and references therein).

Several aspects of surface convection have been investigated in these works, ranging from spectral properties of photospheric lines to granular dynamics (Cattaneo et al., 2001). Nevertheless, the important subject of convective pattern, i.e. the arrangement of individual convective structures in clusters, and possibly in a hierarchy of structures, has been almost disregarded. In our opinion, this topic and the possible existence of regularity in the granular pattern are essential to characterize the convection and derive the system physical properties.

Recently, Getling and Brandt (2002) investigated this argument. In their work is considered the existence, in time-averaged photospheric brightness fields, of quasi-regular structures associated with photospheric convective flows. In particular, they report that '*averaged images are far from completely smeared* *and contain a multitude of bright, granular-sized blotches even if the averaging period is as long as 8 h'*. This evidence has been used to evince that granules prefer to rise from particular sites. Moreover, they stated that time-averaged fields display quite regular arrangements similar to patterns observed in Rayleigh-Bénard convection experiments. They deduced that in the solar atmosphere a previously unknown type of self-organization is present and that *granules are associated with overheated blobs carried by the convective circulation.*

The idea that small scale convection implies some kind of self-organization and topological order (geometrical texture) has been challenged by Rast (2002). In his *Comment on 'Regular structures of the solar photosphere'*, the author shows that all the granulation properties reported in Getling and Brandt (2002) are consistent with a *non-physical* model of features with typical granular lifetime and completely random motion. Therefore, the main conclusion is that the features observed by Getling and Brandt (2002) should be interpreted as statistical properties of a granular random field.

In order to quantitatively study the topological properties of convective flows, it is possible to use statistical methods able to automatically distinguish regular textures (van Siclen, 1997). By applying such approach to photospheric granular patterns, the presence of correlations between convective structures has been retrieved (Berrilli et al., 2003a,b; Consolini et al., 2003) and, as suggested by Nicolis (1989), the occurrence of statistically reproducible relations between distant parts of the system implies the existence of some kind of regularity.

1.2.3 Mesogranulation and Supergranulation: larger scale convective cells?

In the past years, significant results have been obtained by reproducing granular scale convection by numerical simulations and, as discussed in the previous section, there is essential agreement in considering the granulation as the result of recurrent formation of downward plumes induced by hydrodynamic instabilities in the higher photospheric layers.

Conversely, the flows at larger scales, namely mesogranular and supergranular structures, are not satisfactorily reproduced by numerical models. At present time, computer capacity is the limiting factor in reproducing small scale convection in large domains in order to test its efficiency in generating larger scale cellular patterns or the interaction with larger scale convective flows.

In past years, the origin of larger flow patterns on the solar surface, namely mesogranulation (November et al., 1981) and supergranulation (Leighton et al., 1962), has been explained by two different physical mechanisms:

1. The traditional explanation of larger convection cells.
2. The more recent idea of collective interactions between smaller features.

Many of the traditional Kolmogorov's convective theories invoke the mean depths of hydrogen and helium ionization (two such depths for helium) for granular, mesogranular and supergranular scale selection (Leighton et al., 1962; Simon and Leighton, 1964; November et al., 1981). However, such theories suffer of several flaws, as remarked by Rast (2003b). Firstly, they fail to explain why mesogranular and supergranular features have a narrow distribution in size whereas the layers where ionization occurs are quite broad due to perturbations associated with cool downdrafts; secondly, the thermodynamic perturbation caused by helium ionization is generally believed insufficient to produce hydrodynamic instabilities and not well separated in depth from that caused by hydrogen ionization; lastly, all ionization effects on convective flow dynamics are destabilizing and contribute to a reduction in convective scales (Rast, 1991; Rast et al., 2004).

Indeed, numerical models resolving horizontal scales up to 5-10 Mm (Ploner et al., 2000) show that mesogranulation is not rooted in the layers where ionization occurs, but closer to the solar surface, similar to granulation. Notwithstanding, a convective origin of mesogranulation is supported by Lawrence et al. (2001) that applied wavelet spectral analysis to a 2-hour sequence of MDI high-resolution Doppler images near disk centre and concluded that wavelets allow the detection of individual local flow patterns corresponding to mesogranular convection cells. Instead, the non-convective origin of the *mesogranulation phenomenon* has been suggested, in two different papers, by Straus et al. (1992) and by Straus and Bonaccini (1997) invoking, respectively, the middle photosphere overshooting and internal gravity waves in the solar atmosphere as origin of mesogranular scale intensity signature.

A different non-convective origin of greater scales has been invoked by Rast (1995). In this work, the observed association between *exploding* granules and mesogranular flows supported the deduction that granulation dynamics can be identified as the source of mesogranulation. Rieutord et al. (2000) reached a similar conclusion by studying intense positive divergences in the photosphere: they concluded that the mesogranulation signal observed in previous works was a spurious combination of both highly energetic granules, as also acknowledged by Rast (1995), and of averaging effects of data processing.

The viewpoint that the mesogranules owe their origin to collective interactions between the granules is also derived by numerical experiments on turbulent convection by Cattaneo et al. (2001). In their work, the authors supported this conclusion analyzing three-dimensional convection simulations in a very large domain. As a natural corollary of this mesogranulation explanation, both mesogranulation and supergranulation are suggested to be the manifestations of small scale convective features interactions.

Shine et al. (2000), investigated the relation between mesogranules and supergranules by analyzing horizontal divergence maps obtained from a very long timeseries of MDI-SOHO photospheric dopplergrams. The authors concluded that mesogranules, appearing as local maxima in such flow maps, are advected within each supergranule, thus supporting the convective origin of supergranules. Therefore, the dynamics of supergranulation is driven by strong divergences, with narrow boundaries of negative divergence outlining the supergranular cells.

Preliminary results, derived from PSPT-RISE dataset, indicate that while the supergranular magnetic network contribution to the continuum intensity is small but measurable, supergranulation convective contribution lies very near or below detection limits and no clear conclusions could be achieved (Berrilli et al., 1999; Rast et al., 2002). It is necessary, in order to discern the real nature of supergranulation, to disentangle the magnetic network contribution to the continuum intensity from the contribution of the presumed underlying convective supergranular flow. Alternatively, a quantitative study of supergranulation topological properties can reveal similarities or dissimilarities with granulation in order to support or disprove its convective origin.

Reference	Spatial Resolution	Temporal Resolution	Field of View
Herschel (1801)			
Secchi (1870)			
Janssen (1878)			
Hansky (1908)	?		?
Chevalier (1908)	≤0.5”		?
Keenan (1938)	0.14”		?
Macris (1953)	0.08”	10 sec	?
Leighton (1963)	0.3”	1 sec	80”×90”
Mehltretter (1978)	0.4”	8 sec	5”×43”
Roudier and Muller (1987)	0.25”		64”×44”
Title et al. (1989)	0.2”	2 sec	140”×250”
Schrijver et al. (1997)	0.13”		65”×65”
Roudier et al. (1999)	0.25”	20 sec	58”×48”
Hirzberger et al. (1999a)	0.062”	15 sec	30”×30”
Nesis et al. (2001)	0.13”	15 sec	106”

Table 1.1: Granula

Reference	Spatial Resolution	Temporal Resolution	Field of View	Te W
November et al. (1981)	1”	85 sec	60”×160”	60
November et al. (1982)	1”	85 sec	166”×140”	60
Oda (1984)	0.25”	30 sec	54”×52”	
Koutchmy and Lebecq (1986)	0.5”-1”	43 sec	206”	46
November et al. (1987)	1”	10 sec	166”×250”	27
Dame and Martic (1987)	1”	12 sec	90”×90”	20
Wang (1989)	1”	60 sec	250”×250”	10
Frank et al. (1989)	0.25”	20 sec	50”×60”	18
Deubner (1989)	0.5”	6 sec	224”	32
Brandt et al. (1991)	0.25”	12 sec	14”×12”	79
Chou et al. (1991)	1”	90 sec	512”×240”	38
Straus et al. (1992)	1”	94 sec	240”×120”	20
Muller et al. (1992)	0.25”	20 sec	58”×48”	18
Chou et al. (1992)	0.7”	60 sec	136”×100”	18
Abdussamatov (1993)	0.6”	60 sec	138”	18
Abdussamatov (1993)	0.25”		44”×70”	18
Wang et al. (1995)	0.25”	20 sec	31”×31”	60
Straus and Bonaccini (1997)	0.5”	70 sec	90”×90”	24
Bachmann et al. (1997)	1.3”	17 min	200”×200”	
Roudier et al. (1998)	0.25”	45 sec	60”×65”	20
Ueno and Kitai (1998a)	0.6”	15 sec	100”×100”	90
Roudier et al. (2003)	0.25”	21 sec	64”×64”	52

Reference	Spatial Resolution	Temporal Resolution	Field of View
Hart (1956)	∼5”	3.5 min	Full Disk
Leighton et al. (1962)	∼5”	2 h	Full Disk
Simon and Leighton (1964)	∼5”	2 h	Full Disk
Janssens (1970)	∼1”	2 h	∼200”
Sýkora (1970)	∼5”		Full Disk
Duvall (1980)	2”	10 min	400”×512”
Giovanelli (1980)	1”		150”×512”
Singh and Bappu (1981)	∼5”		Full Disk
Singh and Bappu (1981)	∼5”		Full Disk
Brune and Woehl (1982)	∼3”		Full Disk
Rimmele and Schroeter (1989)	∼1”	7.5 min	Full Disk
Hagenaar et al. (1997)	2.14”		840”×560”
Raju et al. (1999)	1.6”	10 min	1400”×140
Berrilli et al. (1999)	2”		Full Disk
Srikanth et al. (2000)	2”	1 min	Full Disk
Srikanth et al. (2000)	1.6”	10 min	1400”×140
Zhao and Kosovichev (2003)	1.1”	1 min	270”×270”

Table 1.3: Supergranu

Chapter 2

Line Diagnostic and Instrumentation

In order to study exhaustively solar atmosphere dynamics, observation at high spatial, spectral and temporal resolution are needed. Such constraints imply the use of suitable instruments and techniques to achieve such purpose.

This chapter will introduce the reader to solar spectroscopy and the instruments able to acquire spectroscopic images. We will recall the notions of line formation and Contribution and Response Functions in order to understand how depth information can be retrieved by spectrum analysis. We will then describe the implementation and capacities of two 2-D solar spectrographs, namely the IPM and the IBIS.

2.1 Line Diagnostic Techniques

The main task of the interpretation of spectra is the 'translation' of observational data into physical quantities commonly used for the description of the stellar atmosphere.

In particular, the interpretation technique determines how to assess the impact of stellar atmosphere parameters on spectrum line profiles.

Therefore, in order to draw the correct conclusions from the observed stellar spectrum, it is necessary to have a proper understanding of how atmospheric phenomena modify the atmospheric mean structure and consequently the spectral line formation.

Among such phenomena, we may mention the variation with depth of temperature, pressure, turbulence, magnetic field, oscillations, rotation and ion species densities.

2.1.1 Contribution and Response functions

As pointed out since a long time (de Jager, 1952), it is extremely important, studying the formation of Fraunhofer lines, to distinguish between the region where the emergent radiation is originated and that where the line depression is formed.

Contribution Functions (hereafter, *CFs*) give the relative contribution of different atmospheric layers to the observed quantity. For example, for the emergent radiation intensity I, that means:

$$I(\lambda)_{\tau=0} = \int_{0}^{+\infty} CF_p^I(\lambda, \tau) d\tau \tag{2.1}$$

More in detail, if I is the specific intensity at wavelength λ, the radiative transfer equation can be written as :

$$\frac{\mu}{\rho}\frac{dI}{dz} = -\kappa[I(z) - S(z)] \tag{2.2}$$

where $\mu = cos\theta$ (θ is the incidence angle), ρ is the gas density, z the geometrical depth, κ the absorption coefficient and S is the Source Function.

Introducing the Optical Depth: $d\tau = \kappa\rho dz$, the solution for $\tau = 0$ is:

$$I(\lambda)_{\tau=0} = \int_{0}^{+\infty} S(\tau) e^{-\tau/\mu} d\tau/\mu \tag{2.3}$$

that is the formal solution of the transfer equation, where $S(\tau)e^{-\tau/\mu}$ is the fraction of the emergent intensity originated in the layer between τ/μ and $\tau/\mu + d\tau/\mu$ or, equivalently, between z and $z+dz$, i.e. the Contribution Function to I: the CF^I.

Instead, in the case of R, defined as the relative depression in an absorption line:

$$R(\lambda)_{\tau=0} = \frac{[I_c(\lambda)_{\tau=0} - I_l(\lambda)_{\tau=0}]}{I_c(\lambda)_{\tau=0}} \tag{2.4}$$

where subscripts c and l indicate the continuous and the line intensities, respectively, the CF^R has a somewhat more complicate expression:

$$R(\lambda)_{\tau=0} = \int_{0}^{+\infty} S_R(\tau) e^{-\tau_R/\mu} d\tau_R/\mu \tag{2.5}$$

where

$$S_R = \left(1 - \frac{S_l}{I_c}\right) / \left(1 + \frac{\kappa_c}{\kappa_l}\frac{S_c}{I_c}\right) \tag{2.6}$$

and

$$d\tau_R = \rho(\kappa_l + \kappa_c \frac{S_c}{I_c}) dz \tag{2.7}$$

The CF^R can be used to infer the average depth $< z(\lambda) >$ of formation of line depression at a given wavelength:

$$< z(\lambda) >= \frac{\int_{-\infty}^{+\infty} z' CF^R(\lambda, z') dz'}{\int_{-\infty}^{+\infty} CF^R(\lambda, z') dz'} \tag{2.8}$$

In a similar way, it is possible to compute the average of other physical quantities.

Response Functions (hereafter, *RF*s) describe the effect that perturbations of a given physical parameter have in an emergent line characteristic (Mein, 1971; Beckers and Milkey, 1975; Canfield and Stencel, 1976; Canfield, 1976; Caccin et al., 1977). If RF_p^C is the response function of the feature C for a certain parameter p, the feature fluctuation that corresponds to a small disturbance Δp, can be written as:

$$\Delta C(\lambda) = \int_0^{+\infty} RF_p^C(\lambda, z)\Delta p(z)dz \tag{2.9}$$

In brief, the RF_p^I is, at each depth, the function we must use for weighting the perturbation p in order to get the variation of the emergent intensity I.

The use of the *RF* or of the *CF* depends on what is analysed. For example, the variation of the line depression due to a change in turbulent velocity should be studied through the corresponding *RF*, but that function does not reveal where the line is formed: the latter information should be derived from the *CF*.

Let's consider the case of Doppler shifts due to a convective velocity field V perturbing the line profile (Buonaura and Caccin, 1982): assuming that such a velocity field will not affect other state variables, we have the perturbation $\Delta p = v(z)/c$, and the RF_V^I given by (to the first order):

$$RF_V^I(\lambda, z) = c\frac{\partial\eta(\lambda, z)}{\partial v}(S(z) - I(\lambda, z))e^{-\tau(\lambda, z)} \tag{2.10}$$

where $\eta(\lambda, z)$is the ratio of line to continuum opacity and c is the velocity of the light.

In the past years *RF*s have been extensively used for the inversion of line profiles and Stokes spectra (Ruiz Cobo and del Toro Iniesta, 1992; Bellot Rubio et al., 1997). By means of *RF*s one can estimate the heights of formation for measurements that are obtained from observed quantities (Sanchez Almeida et al., 1996a,b; Caccin and Marmolino, 1980; Caccin and Penza, 2000, 2002).

2.1.2 2D solar spectroscopy

Most of our astrophysical knowledge is therefore due to spectroscopy, i.e. to the spectral analysis of the radiation emitted by celestial bodies that reach us. This analysis is performed by an instrument called spectrograph, which shows the spectrum of the incoming radiation by means of prisms, gratings or other devices.

Conventional spectrograph need an enter slit and thus provide a 1-D spectrum of the source. This constraint, minor for not resolved sources, is a major limitation for the analysis of resolved objects, as the sun.

To overcome this limitation, 2-D spectrographs, able to acquire monochromatic images of the source, have been built. Two of such instruments, the IPM (Italian Panoramic Monochromator), currently working at THEMIS (Teide Observatory – Izaña – Tenerife – Spain), and the IBIS (Interferometric BIdimensional Spectrometer), installed at the DST (National Solar Observatory – Sacramento Peak – New Mexico – USA), are described later in this chapter.

The basic idea of 2D spectroscopy is to obtain filtergrams at different wavelength in the range of a spectral line, so that the line information (i.e. the spectral line profile) is obtained for each data point across the field of view. By appropriately tuning the transmission wavelength of a narrow band filter, filtergrams can be acquired from the continuum through the line core and forward to the next continuum.

The advantage of 2D spectroscopy compared to classical spectroscopy based on a grating spectrograph is that the spatial and spectral information is obtained almost instantaneously for a 2D field of view. However, this usually provides lower resolution spectra and requires higher photon fluxes, in order to achieve a useful SNR, which can currently be obtained only at solar telescopes. The line profile for each data point is successively obtained by plotting the intensity at a certain position for each filtergram. Therefore, each spectral scan consists of two spatial dimensions, a spectral and a temporal dimension, since the scanning through the line requires some time. If the scanning through the line is performed in a time much smaller than the typical evolution time of the target, it can be assumed that the spectral images have been acquired simultaneously, removing the temporal dimension. Moreover, Doppler map can be obtained computing the line shifts at each pixel, obtaining a Line of Sight (hereafter, LoS) velocity field. Each spectral image and the LoS velocity map can roughly be associated with a given layer in the solar atmosphere which can be estimated by studying the Temperature and Velocity RFs. Therefore, by scanning several feasible lines the 2D spectroscopy provides a tomography of the solar atmosphere (Berrilli et al., 2002).

Line	Wavelength nm	E_{ion} eV	E_{ex} eV	$Log(g_f)$	Γ km	ξ km$\cdot s^{-1}$
C I	538.02	11.26	7.68	-1.64	7	1.5
Fe I	537.96	7.87	3.695	-1.58	5.5	1.5
Fe I	557.61	7.87	3.43	-1.48	30	0.0
Fe I	709.0	7.87	4.23	-1.30	17	1.0
Fe II	722.4	16.18	3.89	-3.28	50	2.0

Table 2.1: Line synthesis parameters.
E_{ion} and E_{ex} are the ionization and excitation energy of the atom/ion, $Log(g_f)$ is the absorption oscillator strength, Γ is the damping factor and ξ is the microturbulence parameter. Line profile reported in Figs. 2.2, 2.1, 2.3, 2.4, 2.5 have been computed employing the parameters reported in this table.

2.1.3 Velocity fields formation height

In order to obtain information about the depth dependence of the photospheric velocity fields by associating to any line a suitable 'formation zone', it is possible to regard their effects on the line profiles as linear perturbations and to study the velocity response functions RF^I_V of the emergent intensity at the observed wavelengths within the lines (Caccin et al., 1977).
In particular, this approach was employed by Berrilli et al. (2002) to derive the

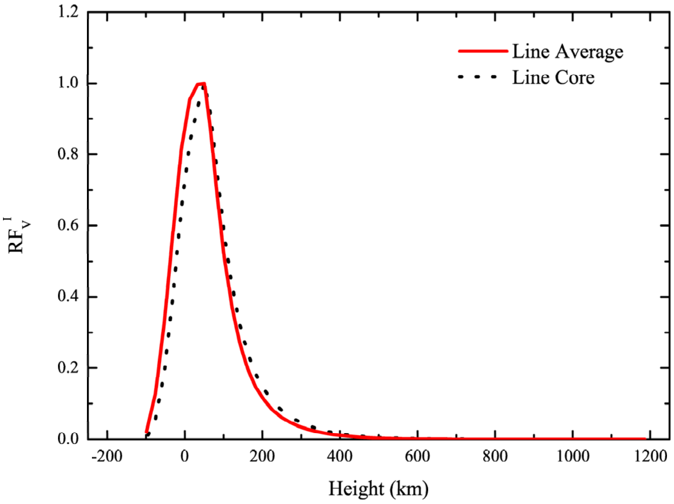

Figure 2.1: Velocity response function RF_V^I for Fe I line 538.02 nm relative to line core (black dotted) and mean line profile (red continuous). RF_V^Is are in arbitrary units.

RF_V^I for three particular spectral lines: Fe I 557.61 nm, Fe I 537.96 nm and C I 538.02 nm. Their calculations were made with the Harvard-Smithsonian Reference Atmosphere (HSRA; Gingerich et al. (1971)) assuming LTE, so that the source function is velocity independent.

They acknowledged some evidence of NLTE effects for the Fe I 557.61 line (Shchukina et al., 1997), which might cause a slight overestimation of the line formation heights, especially in the line core. Therefore, they mimicked NLTE effects in the core of such line by using a monotonically decreasing extrapolation of the HSRA photospheric temperature above $h=$ 550 km, similar to that of the HOLMUL model (Holweger and Mueller, 1974). In Table 2.1.2 we report the position of the peak $< h_\lambda >$ and the full width at half maximum for the mean RF_V^I and the peak position $h_{\lambda_{core}}$ for the line core RF_V^I derived by Berrilli et al. (2002).

The rather large FWHM of the mean RF_V^I imply a broad formation zone for the Fe I velocity fields, while the formation zone for the C I field results more clearly confined.

2.2 IPM

Solar physics derives a large amount of its experimental evidence from a detailed analysis of the Fraunhofer spectrum.

In the past, many aspects of the relationship between the three-dimensional pressure, temperature, velocity and magnetic fields have been derived by mono-dimensional spectral measurements in connection with broad-band imaging (spectral resolving power $\mathcal{R} \leq 50000$) of the solar atmosphere.

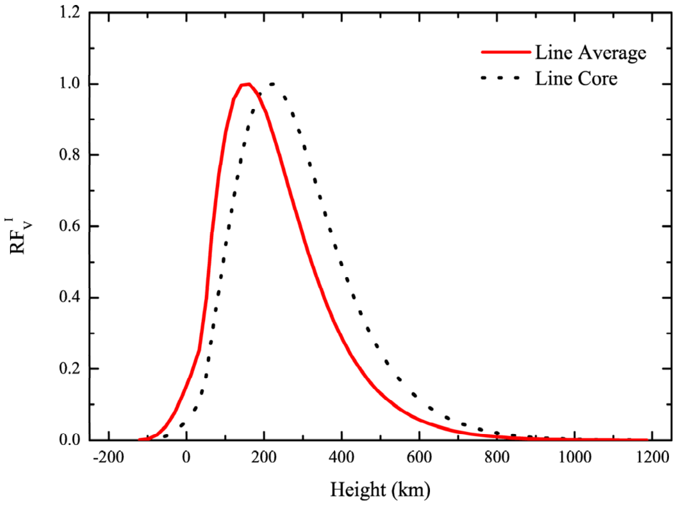

Figure 2.2: Velocity response function RF_V^I for Fe I line 537.96 nm relative to line core (black dotted) and mean line profile (red continuous). RF_V^Is are in arbitrary units.

These attempts were performed via spectroeliographic analysis of the spectrum and successive composition of the spectral image from the single slit images. However, this method is intrinsically slow in image acquisition, while solar observations need high temporal resolution in order to take advantage of good seeing moments and to employ post-facto restoration techniques.

Several attempts to obtain spectral imaging devices by birefringent filters (Öhman, 1938; Lyot, 1944) allowed an exhaustive study of chromospheric structures via H_α and other broad lines images. Unfortunately, due to the poor spectral resolving power of these filters and to the large amount of stray light which leaks from the filter passband side lobes, many questions on the physics and depth structure of the phenomena were unaddressed. Moreover, conventional birefringent filters show very small wavelength tunability, preventing the observation in lines differently sensitive to the solar atmosphere parameters.

In order to cope with such limitations, the IPM is built of a Fabry-Perot (FP) interferometer in tandem with a Lyot-Ohman filter (Universal Birefringent Filter, UBF hereinafter).

The IPM has been build in Arcetri with the contribution of the Department of Physics of the Rome 'Tor Vergata' University.

2.2.1 The concept

From the spectroscopic point of view, the instrument consists of two filters mounted in series.

The overall passband function $W(\lambda)$ will be:

$$W(\lambda) = W_{UBF}(\lambda) \cdot W_{FP}(\lambda) \tag{2.11}$$

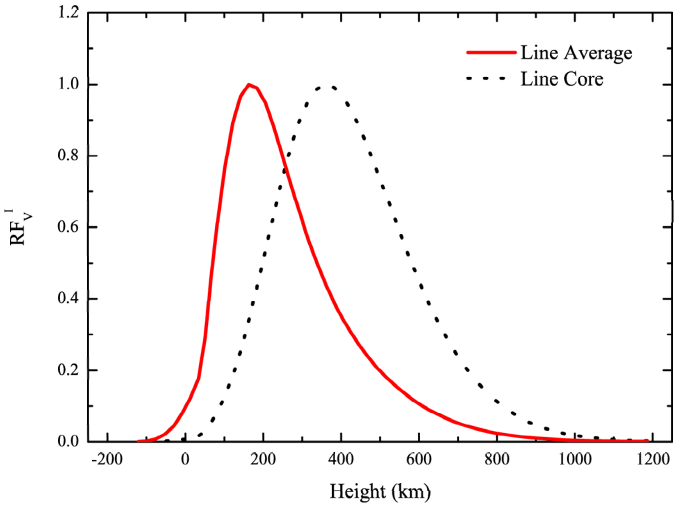

Figure 2.3: Velocity response function RF_V^I for Fe I line 557.61 nm relative to line core (black dotted) and mean line profile (red continuous). RF_V^Is are in arbitrary units.

where $W_{UBF}(\lambda)$ and $W_{FP}(\lambda)$ are the UBF and FP passband functions, respectively.

The UBF and the FP passband function are periodical; in the case of the UBF, each passband order has a shape resembling that of a sinc^2 function, while the FP, each passband order is described by an Airy function with parameters defined by the plate spacing. If the maximum of the UBF transmission profile coincides with one of the FP's, it follows that the overall profile consists of one main peak and some side lobes. The contribution of these side lobes can be minimized by a suitable matching of the interferometer Free Spectral Range (FSR) with the spacing of the UBF zeroes. This constraint and the interferometer quality set the lower obtainable FWHM of the filter passband. Moreover, the instrumental profile is widened by the wavelength shifts introduced when non-axial beams are allowed through the filter system.

This configuration requires a careful tuning of both the UBF and FP. The tune solution of each crystal composing the UBF has to be found and temperature drifts must be taken into account. The FP must be carefully calibrated to allow the required wavelength setting and must be servo-controlled to guarantee the proper plate parallelism and separation. So, a single UBF+FP passband order can be suitably isolated by a simple interference filter with a FWHM $\approx$ 50 Å.

The UBF

The UBF is build of 9 two-beams interferometers mounted in series. Each interferometer is a monoaxial birefringent calcite crystal, mounted between two linear polarizer oriented at 45° with respect to the ordinary and extraordinary

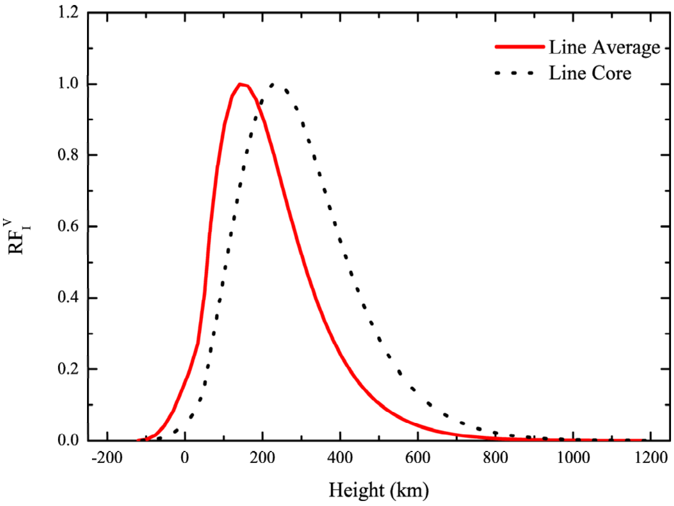

Figure 2.4: Velocity response function RF_V^I for Fe I line 709.0 nm relative to line core (black dotted) and mean line profile (red continuous). RF_V^Is are in arbitrary units.

axis.

Each of these interferometers has an axial passband given by:

$$T(\lambda) = \cos^2\left(\pi d\Delta n/\lambda\right) \tag{2.12}$$

where Δn is the difference between ordinary and extraordinary refractive indexes and d is the physical thickness of the crystal. In the case of the UBF, the optical thickness $d\Delta n$ increases by a factor two from each calcite to the next.

Therefore, the resulting passband is:

$$T(\lambda) = \prod_{i=1}^{9} \cos^2\left(2^{(i-1)}\pi d_1 \Delta n/\lambda\right) \tag{2.13}$$

where d_1 is the thickness of the first and thinnest crystal. When the wavelength λ is such that the ratio $d\Delta n/\ \lambda$ is an integer number, the transmission is maximum. The passband is therefore periodic and the FSR is given by:

$$\Delta\lambda = \lambda^2/(d\Delta n) \tag{2.14}$$

Considering the wavelength of the $H_\alpha$line (6563 Å), the FSR is 128 Å, while the filter FWHM is only 0.25 Å. Such values provide high spectral contrast C = 2.88, defined as the ratio of energy falling inside the FWHM and that falling outside.

Besides the high spectral contrast, the large separation of the side lobes from the band centre with respect to the photospheric line widths, allows minor energy contribution from the nearby continuum while scanning absorption lines.

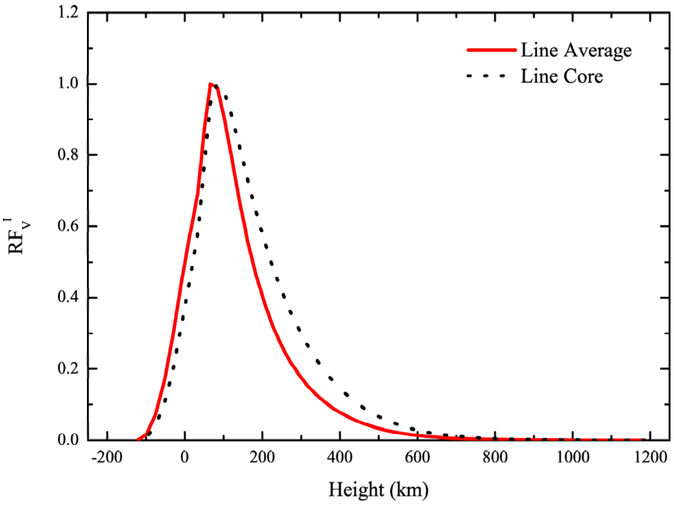

Figure 2.5: Velocity response function RF_V^I for Fe I line 722.4 nm relative to line core (black dotted) and mean line profile (red continuous). RF_V^Is are in arbitrary units.

The rotations of the crystals are performed by nine step motors (500 steps/turn). As in the use of UBF it is essential to exactly know the absolute angular position of each crystal, an optical sensor system monitors each magnetic clutch. It is therefore obtained a positioning repeatability of ± 1 step (0.36 °). The motors are mounted outside the thermally stabilized housing of the optic parts, whose temperature is monitored via the resistance of a platinum wire wound on the crystal group, with sensitivity on 1 mΩ.

The FP

A Fabry-Perot interferometer is an optically resonant cavity. It consists of a pair of quasi-parallel transparent optical plates, whose facing surfaces have been coated with high reflectance layers. As previously mentioned, the normalized transmission passband is given by an Airy function set,

$$T(\lambda) = \left[1 + 4R(1-R)^{-2}\sin^2\left(2\pi\mu t\cos\left(\theta/\lambda\right)\right)\right]^{-1} \tag{2.15}$$

with a FSR given by

$$\Delta\lambda = \lambda^2/2\mu t \tag{2.16}$$

where R is the coating reflectance, μ is the refractive index of the medium inside the cavity, t is the plate separation and θ is the angle of incidence.

The parameters of the FP have been chosen in order to minimize the contribution of the UBF passband lobes in the overall instrumental profile, taking into account that the ratio of the UBF and FP FSRs increases as λ increases.

The plate positions are modified by a piezo-tuned and servo-regulated device. In this device the changes of the plate parallelism and of the interferometer gap

Line	Wavelength nm	$h_{\lambda_{core}}$ km	$< h_\lambda >$ km	FWHM km
C I	538.02	50	30	~150
Fe I	537.96	200	150	~250
Fe I	557.61	320	110	~250
Fe I	709.0	230	140	~300
Fe II	722.4	80	70	~200

Table 2.2: Line formation depths.
These values have been computed on the basis of the plots reported in Figs. 2.2, 2.1, 2.3, 2.4, 2.5.

are sensed by capacitance micrometers and corrected by a suitable controller. The same controller allows linear increase of the gap under computer control, up to 8 interference orders. The parallelism and the spacing are kept with precision better then 10 pm$\cdot$Hz$^{-1/2}$.

2.2.2 The optical mounting

The choice of the optical interface between the telescope and the UBF-FP tandem, as well as the optical coupling of the UBF and the FP, is mainly constrained by the angular properties of the interferometer.

In fact, the relative wavelength shifts $\delta\lambda/\lambda$, due to non axial propagation for the FP and for a UBF element, are respectively given by Bonaccini et al. (1989):

$$\left[\frac{\delta\lambda}{\lambda}\right]_{FP} = \frac{\theta^2}{8\mu} \tag{2.17}$$

$$\left[\frac{\delta\lambda}{\lambda}\right]_{FP} = \left[\frac{\theta^2}{4\mu_0}\right]\left[1 - \frac{\mu_0}{\mu_c}\right] \tag{2.18}$$

where μ_0 and μ_c are the ordinary and extraordinary refractive indexes.

These equations show that, for a given propagation angle, the wavelength shift of the FP is about seven times larger than that of a calcite element.
In the case of the so called *classical mounting*, the primary image, formed by the telescope, is collimated and the UBF-FP filter is inserted near the image of the entrance pupil.
Each image point is formed by a camera lens which focuses a beam of rays propagating trough the filter at the same angle with respect to the optical axis. As a consequence of the different angular sensitivity, a progressive detuning of the FP passband relative to UBF arises when moving from the centre to the rim of the field.
Moreover, if the FP has wedged plates, the insertion in the pupil image produces multiple images. This effect can be avoided by using non-wedged plates and antireflection coating, still a small amount of interference effects remain and produce an unwanted spectral modulation.
Instead, in the *telecentric mounting*, the aperture is collimated onto the interferometer, which is inserted close to the image plane. Consequently, all image points are formed by ray cones containing all the possible directions allowed by

the system.
In this case, if the relay optics has been properly calculated, the multiplicity introduced by wedged plates may be removed in the exit pupil plane by a suitable field stop. *Telecentric mounting* provides spectral homogeneity and uniform illumination on the image at the expense of the passband filter FWHM broadening (Bousquet, 1969).
For IPM a *telecentric mounting* has been chosen, imposing a spectral resolution $\mathcal{R} \approx 300000$ at 5500 Å. Given these constrains and the UBF and FP diameters (28 mm and 50 mm, respectively), the available field amounts to 1.15° per centimetre of the telescope diameter.
The maximum number of resolved elements on a field diameter, following the Rayleigh criterion, is independent from the telescope diameter and is given by:

$$\frac{\delta\beta}{\beta} = \frac{\Phi_{FP}}{1.22\lambda}\theta_{FP} \tag{2.19}$$

where $\delta\beta$ is the angular size in the sky of the resolved element, θ_{FP} is the incidence angle over the FP, whose diameter is Φ_{FP}. In the IPM case, $\beta/\delta\beta$ is about 410 at 4000 Å, therefore, assuming two pixel per resolved element $\delta\beta$, a 1k×1k CCD detector is required to completely exploit the IPM spatial resolving power.

2.2.3 The IPM setup as implemented at THEMIS

The THEMIS telescope is an alto-azimuthal mounting where all the post-focus instrumentation is contained in a cylindrical tank rotating with the telescope around a vertical axis.

The primary mirror is 0.9 m in diameter with an equivalent focal length of 54.861 m (f/61). A transfer optics forms an image, ≈ 4' in diameter, on a secondary focus (F2), where the scale is 0.266 mm·arcsec^{-1} and the FWHM of the point spread function, for diffraction limited optics, is 0.15" at 5500 Å. A moveable mirror, just before F2, horizontally folds the sunlight coming from the telescope towards the IPM. The IPM setup consists of two main optical paths (principal and reference) and several control paths.
Here we briefly account only for the principal and the reference paths.

The telescope forms an image just after the moveable mirror (M1), where a field diaphragm (D1) corresponding to 51" has been placed. This image is collimated by a first lens (L1), followed by a shutter (S1) and by an achromatic polarizing beam-splitter cube (C1), which ends the common part of the principal and reference paths.

The reference paths continues as the polarized lights passes trough an achromatic half plate (WP2) and then trough a lens (L6), forming an image on the reference white-light CCD (CCD1). Between the lens and the CCD, several optical devices are placed: two crossed linear polarizers (LP1), in order to adjust the light level; a filter wheel (W2), carrying several broad-band filters; and a shutter (S5), controlling the exposure time.

The principal path continues trough another achromatic half plate (WP1), a folding mirror (M2) and a second lens (L2). This lens collimates the pupil, forming on a successive diaphragm (D2) an enlarged image of the observed solar region. The FP interferometer (FPI), used in axial mode and telecentric mounting, is placed after this diaphragm, in an image space where the pupil

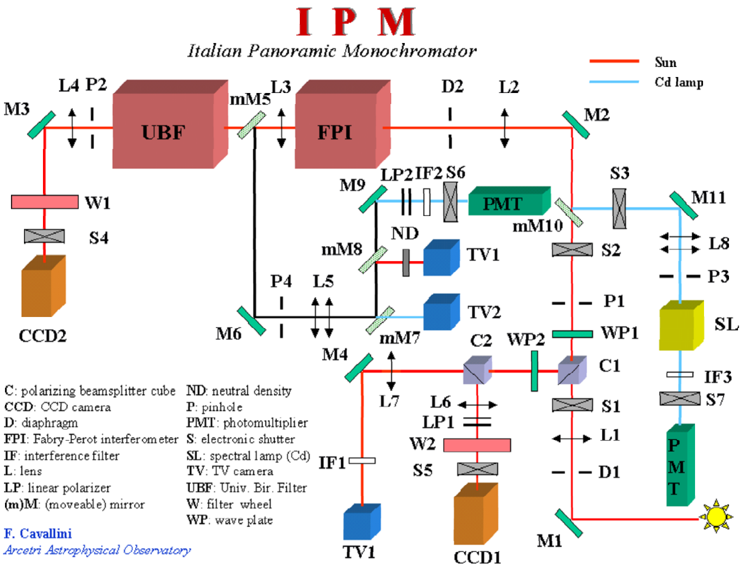

Figure 2.6: The IPM setup as implemented at THEMIS.

is collimated. Just after the FP, a lens (L3) forms an image of the pupil on a pinhole (P2) placed beyond the UBF. After this pinhole, the light passes trough another lens (L4) and reflects on a folding mirror (M3) to from a monochromatic image on the CCD camera (CCD2). This camera is preceded by shutter (S4), which controls the exposure time, and by a filter wheel (W1), carrying the interference filters for the wavelength ranges for which the UBF has been calibrated. Due to its very complex construction, the UBF calibration procedure demands a lot of time to be performed and the use of a spectrograph with a medium-high spectral resolution. Hence, the IPM has been calibrated only on five wavelength ranges, 40 Å wide, centred on lines of astrophysical interest (Mg b1, C I, Fe I, Na D2, H_α). Plus, the range at 6438 Å has been calibrated to allow the measurement of the spectral dishomogeneities of the focal plane. The controller of the FP allows positioning the interferometer plates in few milliseconds, therefore the wavelength setting of the FP is very fast (typically ~ 1.5 ms). The instrumental wavelength setting time is imposed by the UBF and depends on the angular rotations of the calcite crystal groups necessary to set the demanded wavelength passband. If a different wavelength range is requested, also the two filter wheels, preceding the CCD cameras, must be re-positioned. Therefore, the setting time for small wavelength steps is about 0.1 s, while the setting time for changing the spectral range is about 1 s, so that, if a sequence of images acquired at equal time intervals is desired, a minimum wavelength setting time of 1 s must be used.

Wavelength range	460.0 - 680.0 nm
Available spectral lines	518.4 nm Mg b1
	538.0 nm C I
	557.6 nm Fe I
	589.0 nm Na D2
	643.8 nm Cd red line
	656.3 nm H_α
Range width	± 2.0 nm
Spectral resolving power	260000 - 270000
Passband FWHM	1.7 pm - 2.6 pm
Wavelength drift of the instrumental profile	$\leq 10 m \cdot s^{-1}$ on 10 h
Field of view	51" (circular)
Peak transparency	0.7% - 2.0%
Image scale	0.06" pixel^{-1}
Exposure time (for S/N $\sim$ 100 and 2 pixels/resolved element)	200 - 300 ms
Acquisition rate (1024 x 1024 pixel^2 @5 Mpixels/sec)	$\sim$ 1.0 frames$\cdot s^{-1}$

Table 2.3: IPM Instrumental Characteristics

2.3 IBIS

At the end of 1999 started in Arcetri the construction of IBIS (Interferometric BIdimensional Spectrometer), a new instrument for solar spectroscopy, built with the contribution of the Arcetri Astrophysical Observatory, the Department of Astronomy and Space Science of the Florence University and the Department of Physics of the Rome 'Tor Vergata' University.

IBIS is an instrument designed to obtain monochromatic images of the solar surface, designed to overcome the limitations of IPM, mainly due to the use of the UBF to isolate one order of the interferometer. The role of UBF is, in the IBIS configuration, undertaken by a second Fabry-Perot interferometer. This solution, adopted in other solar monochromator (Kentischer et al., 1998; Tritschler et al., 2002), did not accomplished sufficiently good results, mainly due to the difficulty in achieving the correct tuning. Such a problem has been solved in the IBIS configuration implementing two piezo-scanned and capacity servo-controlled Fabry-Perot interferometers, used in classic mounting and axial mode, in series with a narrow-band interference filter (band-pass 3/5 Å). The images are acquired by two high speed 1317×1035 pixels 12-bits CCD cameras. The unique electronic shutter, placed near the pupil plane, guarantees simultaneous acquisition and same integration time for the two cameras.

2.3.1 The concept

Due to its passband profile, a single FP cannot be used as a spectroscopic device and an order sorter is necessary to isolate only one interference order. On IPM, this function is performed by the UBF, imposing a long wavelength setting time, strong limitation on the useful spectral range and a decreased optical quality. However, a single interference order can be isolated also by employing an interference filter and a series of FP interferometers with suitably different spacing.

The overall instrumental profile of N FPs and an interference filter is:

$$T(\lambda) = T_{IF}(\lambda) \prod_{i=1}^{N} T_i\,(\lambda) \tag{2.20}$$

where T_{IF} and T_i are the transmission profiles of the interference filter and of the i-th FP, respectively.

In designing a multi-FP, the problem to be addressed is to finding the ratio between the spacing of the FPs which minimizes the parasitic light, while considering two main problems: the presence of spurious images produced by inter-reflections between pairs of FPs and the difficulty of guaranteeing the correct tuning between the various interferometers.

2.3.2 The optical mounting

On IBIS the FP interferometers are piezo-scanned and capacity servo-controlled, with a clear aperture of 50 mm, a maximum flatness error The FPs are used in *classic mounting*, therefore the image points are formed by collimated ray bundles, incident at different angles on the interferometers plates. That allows higher spectral resolution and guarantees the same shape of the instrumental profile on all the points of the final image plane.

Between the two FPs, a filter wheels carries a set of narrow-band interference filters (FWHM $\sim$ 5 Å) with the double purpose of isolating the instrumental profile and of reducing the ghost images produced by inter-reflection between the FPs plates. Due to the filter, the intensity of the ghost images is lowered to $\approx 1\%$. This allows the use of the interferometers in axial-mode, avoiding the unwanted effects by relative tilt, essentially consisting in an asymmetry of the instrumental profile, a greater width of the passband FWHM and a lowered transparency (Loughhead et al., 1978).

The high transparency of the whole system allows very short exposure time and hence the reconstruction of the seeing distorted wavefront by means of post-facto (*phase diversity*, for example) techniques applied to monochromatic images.

2.3.3 The IBIS setup as implemented at DST

The Dunn Solar Telescope (DST) is a 76 cm f/72 coelostat with alt-azimuth mounting. The two 45 degree plane mirrors move in order to guide the light of the sun down a 41 m tower in an evacuated tube. Its primary mirror is situated 72 m underground and focuses the light to the exit of the vacuum tube, where a moving folding mirror switches the light path over the optical bench where IBIS has been assembled.

The IBIS setup consists of two main optical paths (principal and reference) and several control paths.

Here we briefly account only for the principal path.

After the folding mirror, a lens (L0) forms an image just after two other folding mirrors, where a field stop (FS) corresponding to 80” has been placed. A lens

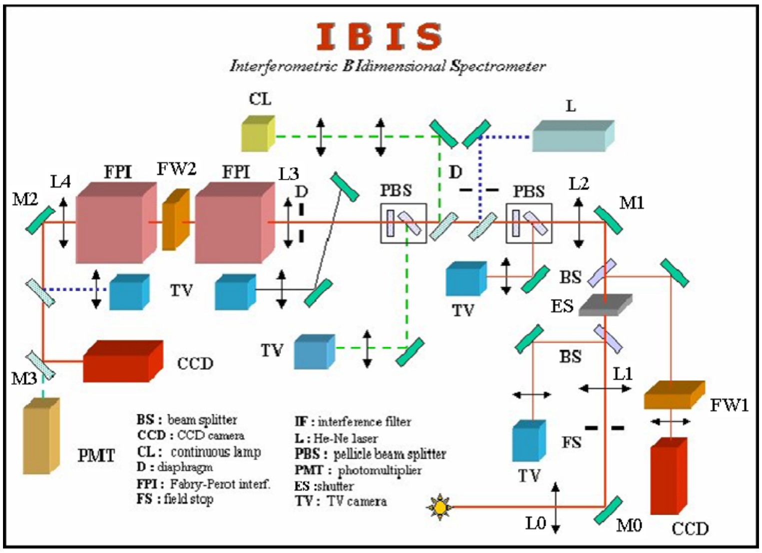

Figure 2.7: The IBIS setup as implemented at DST.

L1 is used in order to obtain a pupil plane on the successive shutter (ES), which controls the exposure time, and then two more lenses (L2 and L3) are used to obtain the classic mounting configuration. This last couple of lenses focuses the image amid the two FPs, where the filter wheel (FW2), carrying the narrow-band interference filters, is positioned. A diaphragm (D) has been placed before the FPs in order to reduce stray light. Beyond the FPs, a last lens (L4) focuses the image on the CCD, through two folding mirrors (M2 and M3).

The useful range of wavelength investigable with IBIS is limited only by the presence of suitable interference filters in order to isolate the right double-FP order.

As the positioning of the FPs plates is very fast, the wavelength setting time is defined by the filter wheel repositioning time. Hence, if a sequence of image acquired within the same line profile is desired, a mean wavelength setting time of $\sim$ 20 ms must be expected, whenever is necessary to change the interferential filter in the configuration, the wavelength setting time may increase to 0.5 seconds.

Finally, due to the high transparency and the consequent short exposure time ($\leq$ 20 ms vs. 200 - 300 ms of IPM, for S/N $\geq$ 100), a high temporal resolution (3 frames per second) can also be obtained. Moreover, such exposure times are sufficiently short to freeze the seeing, therefore, by using post facto restoring procedures, such as the Phase Diversity (cfr. Chapter 3) technique, it is possible to obtain high spatial resolution, up to the nominal limit of the telescope.

Wavelength range	580.0 - 860.0 nm
Available spectral lines	589.6 nm Na D1
	630.2 nm Fe I
	709.0 nm Fe I
	722.4 nm Fe II
	854.2 nm Ca II
Range width	± 200 pm (580.0 - 750.0 nm) ± 350 pm (750.0 - 860.0 nm)
Spectral resolving power	212000 - 274000
Passband FWHM	2.1 pm - 4.2 pm
Wavelength drift of the instrumental profile	$\leq 10 m \cdot s^{-1}$ on 10 h
Field of view	80" (circular)
Peak transparency	15% - 20%
Image scale	0.08" pixel^{-1}
Exposure time (for S/N $\sim$ 100 and 2 pixels/resolved element)	7 - 18 ms
Acquisition rate (1024 x 1024 pixel^2 @5 Mpixels/sec)	3 frames$\cdot s^{-1}$

Table 2.4: IBIS Instrumental Characteristics

Chapter 3

Phase Diversity

In order to reach a high spatial resolution in solar observation, it is important to take into consideration and minimize the aberrations introduced by the seeing. Moreover, as optical paths are growing more and more complicated, also aberrations stemming from the instrument itself can concur in spoiling the image quality. Phase Diversity (PD) techniques are post-processing procedure for correcting aberrations induced by both instrument and atmosphere in individual isoplanatic patches. These techniques do not require sophisticated observing instrumentation and are not based on theoretical models describing atmospheric degradation, but rely on simple optical principles. Their purpose is to determine the wavefront aberrations at the entrance pupil of the telescope from the information contained in two simultaneously acquired images, one focused and the other affected by a known amount of defocus.

In this chapter we will introduce the basic principles of Phase Diversity and present a particular implementation of PD speckle imaging. We will give detail about the application of such PD procedure by the author to images acquired at THEMIS in order to enhance their quality and estimate the telescope intrinsic aberrations.

3.1 Introduction

An important task in ground-based astronomy is to improve the angular resolution that can be achieved. The angular resolution is almost always limited by phase aberrations introduced by terrestrial atmosphere turbulence.
For the particular case of ground-based solar astronomy, the spatial resolution is typically limited to about 0.5" for short exposure images. ($\leq$20 ms). Many processes on the Sun, however, take place at scales well below 1.0", as the photon mean free path in the lower photosphere corresponds to about 0.1" at the disk centre. Magnetic structures may occur on even smaller scales (typical diameter of magnetic flux tubes is 0.2" (Keller, 1995). Despite such a small size, these small magnetic structures are believed to play an important role in large-scale phenomena such as the solar magnetic dynamo, irradiance variation or solar coronal heating. To understand a variety of solar phenomena, it is, therefore, essential to reach a spatial resolution well below the seeing imposed limit and

possibly approaching the diffraction limit of existing and future large solar telescope.

Recently developed methods, which estimate the wavefront over isoplanatic areas from multiphase (or 'phase diverse') images, address this problem.
The technique of phase diversity (PD) was first proposed by Gonsalves and Childlaw (1979) as a method for simultaneously estimating the wavefront aberrations and the source object from simultaneous images with a known phase difference (most commonly a difference in focus position). Another interesting property of phase diversity methods is that they estimate and correct also for the aberrations stemming from the telescope.
This technique has been successfully used by several authors to determine aberrations (Carreras, 1993; Kendrick et al., 1994; Lee et al., 1997; Thelen et al., 1999; Löfdahl et al., 2000) and also to restore images (Restaino, 1992; Löfdahl and Scharmer, 1994; Seldin and Paxman, 1994).
However, in condition of poor seeing or weak signal levels, a single pair of focused-defocused images may not contain enough information to allow reliable reconstruction of the object and the wavefront. Even under favourable conditions for which phase diversity is able to reproduce fine wavefront estimates, object information at single spatial frequency may be irretrievably lost, resulting in artifacts in the object restoration.
To address this problem, Paxman and Seldin (1993) suggested joint phase-diverse speckle (JPDS), while Löfdahl and Scharmer (1993) developed partitioned phase-diverse speckle (PPDS).
Both methods utilized a joint estimation of the aberrations and the common object via the analysis of a time sequence of phase-diverse data. Those extra realizations provide the missing phase information at spatial frequencies where single optical transfer functions (OTFs) are null. A small number of image couples (3-5 couples, usually) are sufficient for good restorations, considerably reducing the amount of data needed compared to speckle methods (Paxman et al., 1996).

PD techniques are now used by some groups to realize time sequences of fine-scale solar features.
Löfdahl et al. (2001) restored two 44"×80" image sequence of co-spatial and co-temporal 430.5 nm *G*band and 436.4 nm continuum filtergrams, obtained with the 47.5 cm Swedish Vacuum Solar Telescope, lasting 5h and 8h, respectively.
Scharmer et al. (2002) restored a 3.5h G-band and continuum image sequence, targeting NOOA active region 10030 with the Swedish 1-m Solar Telescope (Scharmer et al., 2003). These images achieved the best ever spatial resolution benefiting from both the Adaptive Optics system and the post-processing PD restoration.
Bonet et al. (2004) corrected 2564 images (46"×75") of a sunspot close to disc centre, acquired simultaneously in the *G*-band and in the blue continuum at 450.7 nm, for telescope aberrations and turbulence perturbations by applying PD, realizing a 2h time sequence.

3.1.1 Phase diversity principle

Due to the relationship between the point spread function (PSF) h and the aberrated phase, the estimation of the aberrations from the sole focused image does not ensure the uniqueness of the solution.
Phase Diversity Gonsalves (1982) aims to provide more information and remove this indetermination. The idea is to collect at least one supplementary image, which differs from the focused one by a known phase variation. A possible phase variation, and commonly the easiest to achieve, is the defocus, obtained by introducing a beam-splitter and a prism and recording the focused and defocused images on the same detector Gates et al. (1994). PD employs a low-cost, optically simple set-up, but requires a complex numerical procedure to return the phase aberrations and restore the images.

3.2 Phase Diversity Implementation

3.2.1 Imaging model

In the hypothesis of isoplanatism, the image i is the noisy convolution of the PSF h in the observation plane and the object o:

$$i(\vec{r}) = (h(\vec{r}) * o(\vec{r})) + n(\vec{r}) \tag{3.1}$$

where $*$ denotes the convolution product, $\vec{r}$ is a two-dimensional vector in the image plane and n is additive noise.

The PSF associated with the focused image f is given by:

$$h_f(\vec{r}) = \left| FT^{-1} \left\{ P(\vec{u}) \cdot e^{i\Phi(\vec{u})} \right\} \right|^2 \tag{3.2}$$

where $\vec{u}$ is a two-dimensional vector in the pupil plane, Φ is the unknown aberrated phase function, P is the aperture function and FT^{-1} denotes the inverse Fourier transform.

As aberrations in an optical system can be mathematically represented by Zernike polynomials (Noll, 1976), the phase function is expanded on a set of such polynomials.

$$\Phi(\vec{u}) = \sum_{j=1}^{J_{max}} a_j Z_j(\vec{u}) \tag{3.3}$$

Theoretically, J_{max} should tend to infinity to describe any wave form, but in the particular case of static aberration estimation, the first polynomials (typically the first twenty) are enough to describe both the atmospheric and optical system aberrations.
In the following, we will note $\vec{a} = (a_1, ..., a_{J_{max}})^T$ the unknown aberration coefficients, where T denotes transposition.
In the defocused plane, the PSF of the defocused image d is given by:

$$h_d(\vec{r}) = \left| FT^{-1}(P(\vec{u}) \cdot e^{i[\Phi(\vec{u}) + \Phi_d(\vec{u})]}) \right|^2 \tag{3.4}$$

where Φ_d is the known diversity phase function. In our case, $\Phi_d(\vec{u}) = a_4^d Z_4(\vec{u})$, where Z_4 is the defocus Zernike polynomial. The problem is to estimate the aberration parameters $\vec{a}$ (the set of a_j) from the data (focused f and defocused d images), without knowing the object o.

As the PPDS and JPDS significantly differ in noise model, estimator, regularization and optimization techniques, henceforth we will refer only to the PPDS implementation of phase-diversity speckle imaging.

3.2.2 Aberration estimation principle

The PPDS utilizes extra realizations of the unknown objects to fill in the possibly missing phase information. In practice, N couples of images are used to retrieve N different h; these results are then employed to obtain the best estimate of o.
Moreover, the PPDS relies on two modification of the original error metric proposed by Gonsalves and Childlaw (1979). First, as the estimation of the unknown object is performed implicitly, while the estimation of the aberrated wavefront is performed explicitly, the expression for the optimal object cannot be employed directly into equation 3.7 , because it would lead to unlimited amplification of noise at spatial frequency where the OTF of the couple of image approaches small values. This happens because the restored object is retrieved via a best fit to the data, including its noise. As a consequence, noise filtering is essential. However, for the sake of simplicity, in the next formulation the noise filter is omitted, because its implementation can be explained afterwards easily. Second, the SNR of the two image channels are allowed to be significantly different, as in the case of a beam-splitter that does not divide incoming light into equal parts. With this modification the error metric for a single couple of focused/defocused images can be defined as

$$L = \sum_{\vec{u}} \left| I_f - \hat{H}_f \hat{O} \right|^2 + \gamma \left| I_d - \hat{H}_d \hat{O} \right|^2 \tag{3.5}$$

where $\hat{}$ denotes an estimation, I_i, H_i and O are the Fourier transform of i_i, h_i and o, respectively, and

$$\gamma = \sigma_f^2 / \sigma_d^2 \tag{3.6}$$

where σ_i stands for the RMS values of the noise for the images and $i = [f, d]$.

Obviously, with $\gamma=1$, we recover the original error metric of Gonsalves and Childlaw (1979).

The best estimation for O is the one that minimizes:

$$L_M = \sum_{\vec{u}} \frac{\left| I_d \hat{H}_f - I_f \hat{H}_d \right|^2}{\left| \hat{H}_f \right|^2 + \gamma \left| \hat{H}_d \right|^2} \tag{3.7}$$

Therefore we can compact the problem by defining the new error function E as:

$$L_M = \sum_{\vec{u}} |E|^2 \tag{3.8}$$

which can be minimized using an iterative algorithm.

The expansion of the phase function in terms of Zernike Polynomials and the consequent linearization allows us to write:

$$\delta E = \sum_{j=1}^{J_{\max}} \frac{\partial E}{\partial a_j} \delta a_j \tag{3.9}$$

where $J_{\max}$ is the number of polynomials employed in the expansion. This is equivalent to search for the minimum of

$$\sum_{\vec{u}} \left| E + \sum_{j} \frac{\partial E}{\partial a_j} \delta a_j \right|^2 \tag{3.10}$$

with respect to δa_j. Therefore we obtain a linear system:

$$\left(\frac{\partial E}{\partial a_k} \middle| \frac{\partial E}{\partial a_j} \right) \cdot \delta \vec{a} + \left(\frac{\partial E}{\partial a_k} \middle| E \right) = 0 \tag{3.11}$$

where $(f\,|g) = \sum_{\vec{u}} f g^*$, to solve for each image couple.

Once the N object estimates $\hat{O}$ or, alternatively, the N $\hat{H}_f$s have been obtained, the best estimate of O is obtained by minimizing the sum of the N different metrics L_M with respect to O:

$$O = \frac{\sum_{n=1}^{N} \left(I_{nd} \hat{H}^*_{nf} + \gamma I_{nf} \hat{H}^*_{nd} \right)}{\sum_{n=1}^{N} \left(|\hat{H}_{nf}|^2 + \gamma |\hat{H}_{nd}|^2 \right)} \tag{3.12}$$

where n represents the n^{th} couple of the speckle group.

Spectral bandwidth

The phase diversity concept proposed here is a monochromatic wave-front sensor (theoretically the concept can be applied on polychromatic images but this would induce important modifications (Seldin et al., 2000)).
Nevertheless it has been shown (Meynadier et al., 1999) that the use of broadband filters does not significantly degrade the accuracy as long as $\frac{\Delta\lambda}{\lambda}$ is lower than a few tens of percents (typically$\frac{\Delta\lambda}{\lambda} = 0.15$).

Noise filtering

The error metric defined in equation 3.8 is such that additive white noise does not affect the solution. Noise, however, can affect the convergence of the iterative system and is unlimitedly amplified in equation 3.7. To solve these problems, a filter W is easily introduced into the formulas by replacing the quantities I_i by their filtered counterparts WI_i (Löfdahl and Scharmer, 1994).

Figure 3.1: The THEMIS telescope at Izaña, Tenerife (Spain).

Such a filter is recovered directly from the images in order to minimize the combined rms error (from noise and filter) in the restored object:

$$W = 1 - < |\eta|^2 > \left\langle \frac{\sum_{n=1}^{N} \left(\left| \hat{H}_{nf} \right|^2 + \gamma \left| \hat{H}_{nd} \right|^2 \right)}{\left| \sum_{n=1}^{N} \left(I_{nf} \hat{H}^*_{nf} + \gamma I_{nd} \hat{H}^*_{nd} \right) \right|^2} \right\rangle \tag{3.13}$$

where the summation is performed over the N couples of images, η stands for the noise rms and angle brackets denote an expectation value. In particular, the second expectation value is estimated with a smoothing operator and the elimination of noise peaks in the high-frequency regime.

As the number of couples of focused-defocused images increases, the frequencies spanned by the filter expands, because information is added to complete the combined OTF at frequencies where single OTFs were null.

3.2.3 Phase diversity implementation at THEMIS

On the days 15^{th}, 21^{rd}, 23^{rd} and 29^{th} May 2002 observational runs in PD configuration were performed at THEMIS.

The Phase diversity hardware was implemented at the secondary focus environment of the telescope, using the the reference channel of the IPM instrument. The 1317×1035 pixel^2 Kodak KAF 1400 camera was used to acquire the near

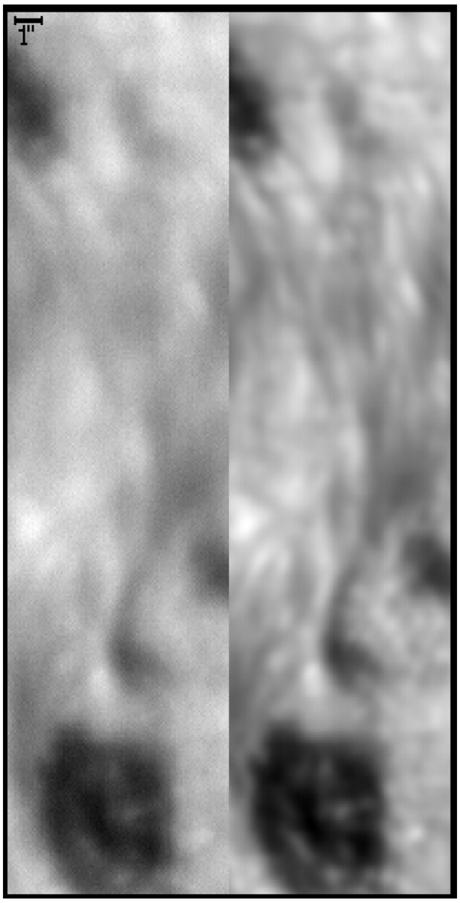

Figure 3.2: Left panel: detail of the best of the focused images employed in the PPDS restoration. Right panel: same detail in the PPDS restored image.

infrared (850 nm) broadband data. The image scale was set at 0.075"·pixel^{-1}, the diffraction limit resolution was 0.19". The exposure time for each image pair was 20 ms.

A suitably placed beam-splitter, increased of ∼24 mm the optical path relative to the defocused image, therefore setting the diversity factor to ∼1.7 waves peak-to-peak. The shutter was placed in a pupil plane in order to give exactly simultaneous exposures to the two channels.

As previous works indicated an isoplanatic angle of ∼5" as a reasonable approximation (Löfdahl and Scharmer, 1994), the error metric and its derivatives were evaluated over 70×70 pixel^2 (∼5"×5") subfields, while the FFTs were calculated on 100×100 pixel^2 subfields. Therefore, each image was divided in 16 isoplanatic patches, which were PPDS processed.

The wavefronts were estimated using the first 21 Zernike polynomials and the apodization of subfields was performed with a modified Hanning window. After the PPDS procedure, the restored sub-fields are mosaicized so to reconstruct the FoV (Field of View).

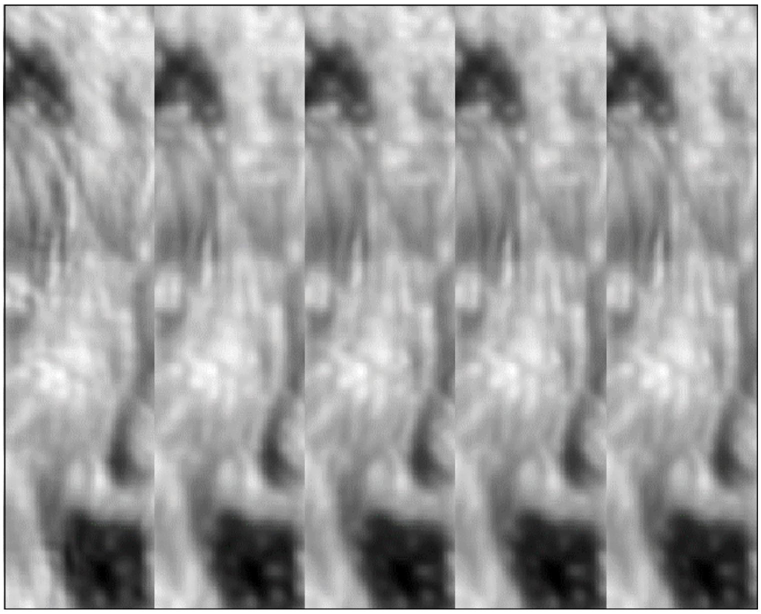

Figure 3.3: PPDS restored images employing 1, 2, 3, 4 and 5 image couples (cfr. 3.2.2).

Although seeing was very variable during the observation runs, the overall quality of the restored data is comparable to the highest quality images acquired at THEMIS. In several cases the analysis of the power spectra of the processed images revealed showed that the spatial frequencies were restored up to the intrinsic telescope diffraction cut-off.

Using the 15 May data a comparison of PPDS data obtained by combining from 1 to 5 image pairs has been performed. We recall that pure PD is the special case of PPDS with 1 pair only. It has been found that some evident restoration artifacts emerge in the restored scene when the pairs are less than 3, while by adding more images in the speckle reconstruction such artifacts disappear, achieving an optimal restoration.

An estimation of the IPM reference paths aberration has been attempt by restoring a 75 image-pair series.

From the single estimate of the wavefront error for each patch a total of 1200 sets of aberration parameters (the Zernike polynomials coefficients) were obtained. For each coefficient the correspondent histogram has been produced. Gaussian distributions are expected for seeing induced aberrations and the mean of such distributions should be zero when observing with a perfect optical set-up. Consequently, the mean of the empirical histograms will reveal the amount of aberration stemming from the instrument. By fitting a Gaussian function to each distribution the mean value $\times_c$ and FWHM were retrieved and it was possible to reconstruct the intrinsic PSF of the optical setup (see Figure 3.5). The FWHM of this PSF is 0.19" at 850 nm wavelength and the Strehl ratio is 81%.

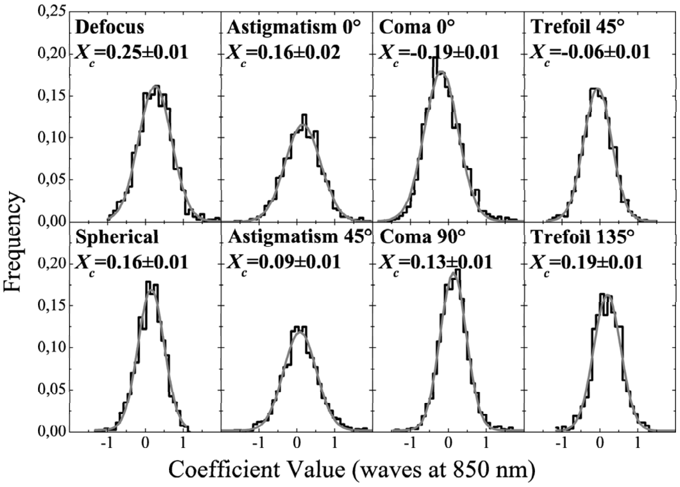

Figure 3.4: Frequency histograms for Zernike coefficients from 4 to 11. Distribution mean values X_c give an estimation of intrinsic optical setup aberrations in units of waves at 850 nm wavelength.

Choice of the defocus distance

The choice of the known defocus distance is essential to obtain accurate results. The RMS defocus coefficient a_4^d depends on the defocus distance d of the second image, the telescope diameter D and the focal length F through:

$$a_4^d = \frac{\pi d}{8\sqrt{3}\lambda(F/D)^2} \tag{3.14}$$

expressed in radians. The corresponding peak-to-valley optical path is equal to

$$\Delta = \frac{\sqrt{3}\lambda a_4^d}{\pi} = \frac{d}{8(F/D)^2} \tag{3.15}$$

As the 'optimal' defocus distance depends on the object structure, the phase amplitude Φ and the *SNR* on the images, it has been shown (Lee et al., 1999) that a defocus equal to λ provides correct results. In practice, a large domain around this value (typically $\lambda \pm \lambda/2$) still provides accurate results (Meynadier et al., 1999). This validates the choice of 24 mm defocus length in the implementation of PPDS at THEMIS.

Pupil shape

An exact knowledge of the pupil shape (diameter, central obstruction, global shape) is required.
In particular, few percents of error in the pupil estimation lead to an error of a few tens nanometres on the phase estimation.

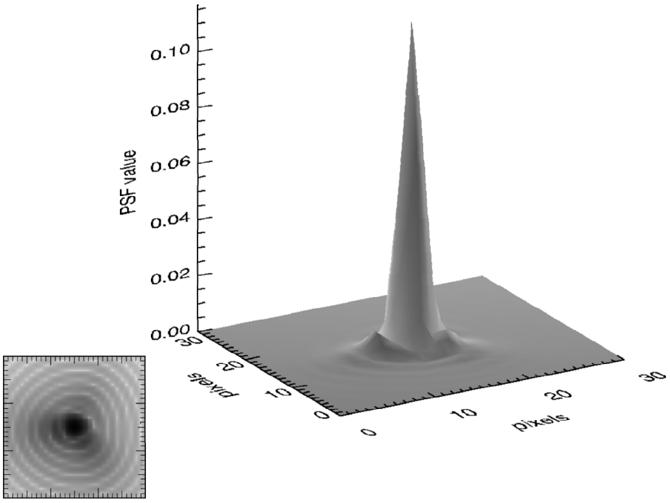

Figure 3.5: 3D and logarithmic (lower left corner) views of the retrieved intrinsic PSF of the PD optical set up. The PSF has been reconstructed by utilizing the Zernike coefficient mean values X_c from Figure 3.4.

In the particular case of the implementation of PPDS at THEMIS, the annular shape of the entrance pupil should be taken into consideration. Therefore, a modified set of Zernike polynomials has been created by the author via the definition of a suitable annular pupil and successive Graham-Schmidt hortonormalization.

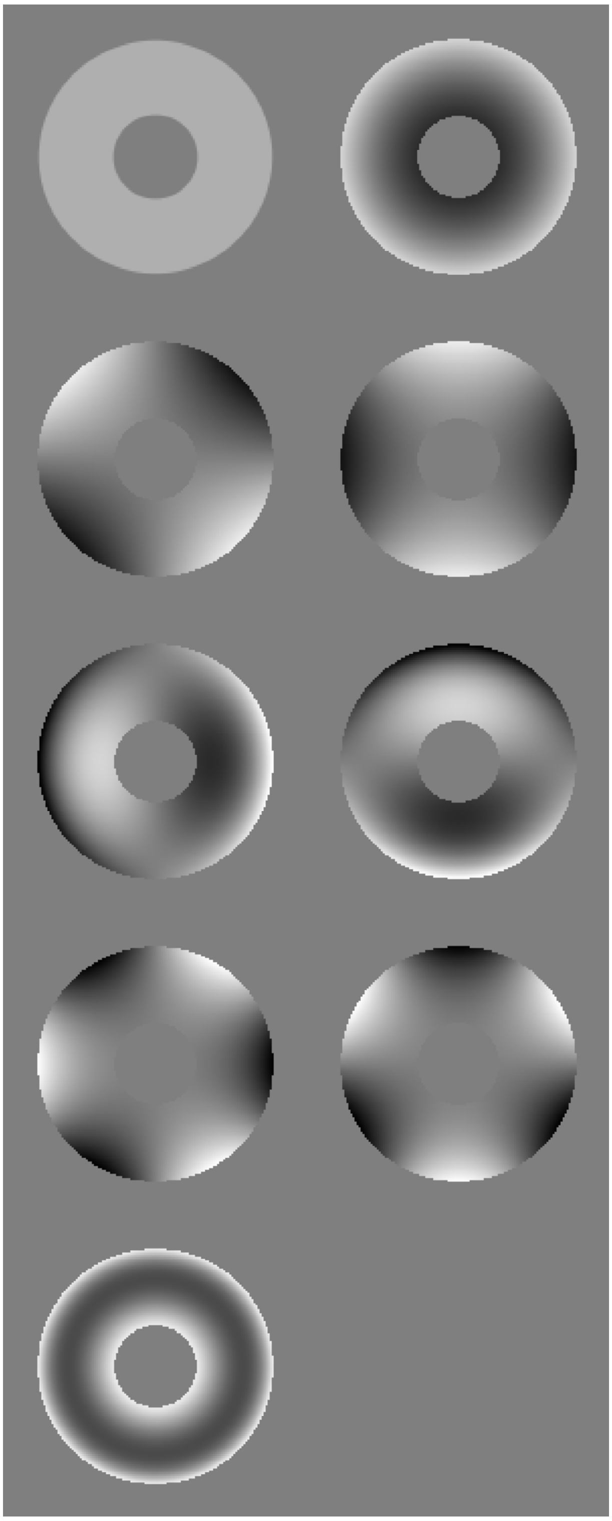

Figure 3.6: Pupil shape and annular Zernike polinomials from 4 to 11. From left to right and from top to bottom: pupil shape, defocus, astigmatism 0°, astigmatism 45°, coma 0°, coma 90°, trefoil 45°, trefoil 135° and spherical aberration.

Chapter 4

Helioseismology

As already stated in chapter 1, the interior of the Sun cannot be directly observed. Nevertheless, a time series of 'images' of the plasma flow below the photospheric surface can be obtained by means of Local Helioseismology. The temporal evolution and the geometric properties of the flow structures present in such a time series can thus be investigated by suitable feature-tracking algorithms. In order to enhance the comprehension of the dataset employed later in this work, this chapter will introduce the reader to the concept of Global and Local Helioseismology. We will begin by describing the oscillation by means of normal modes in order to understand how to derive the internal stratification and rotation by inverting the frequencies of the modes. In particular, the inversion problem for rotational splitting will be discussed. The second part of this chapter is devoted to the description of Local Helioseismology and, in particular, of the time-distance technique. The inversion of time-distance helioseismic data into a supergranular flow field is presented at the end of this chapter.

4.1 Helioseismology Principle

Since the Sun is a ball of hot gas, its interior transmits sound very well. It is generally believed that convection near the surface gives rise to vigorous turbulent flows that produce a broad spectrum of random acoustical noise. Furthermore, since the Sun is essentially spherical, it also forms a spherical acoustical resonator with millions of different normal modes of oscillation.

Due to the waves' long life times, destructive interference filters out all but the resonant frequencies, transforming the random convective noise into a very rich line spectrum in the five-minute range. The oscillation modes are trapped in spherical-shell cavities starting essentially at the visible surface and extending inward. The outer boundaries are defined by the abrupt change in sound speed associated with the steep temperature gradient in the superadiabatic region just below the surface. The inner boundaries result from the refraction of the waves back toward the surface, caused by the inwardly increasing sound speed (essentially, temperature).

While the outer limits of all of the cavities are confined to a narrow region just below the photosphere, the depth of a given cavity depends on both the oscillation frequency and the spherical-harmonic degree of the associated mode.

Consequently, there are modes whose entire cavities are confined very near the surface, while others extend much deeper, even reaching the centre of the Sun itself. Depending on the frequency and degree, these modes sample different, but overlapping, regions of the solar interior. As the precise frequency of a particular cavity depends intimately on the thermodynamic, compositional, and dynamic state of the material in the cavity, they can be used to probe the temperature, chemical composition, and motions throughout the interior of the Sun.

4.2 Global Helioseismology

Helioseismology is the study of the interior of the Sun from observations of the vibrations of its surface. Oscillations of stars have been recognized since the late 1700s. The complicated pattern of the Sun's oscillation was first observed by Leighton et al. (1962). The explanation of the pattern in terms of trapped acoustic waves came by Ulrich (1970); Leibacher and Stein (1970). This explanation predicted certain detailed features of the spectrum of solar oscillations that were confirmed by observations made by Deubner (1975). The Sun is constantly vibrating in a superposition of acoustic normal modes. Oscillations on the solar surface are measured by observing the oscillation of the Doppler shift of a spectral line as the plasma producing the spectral line oscillates back and forth along the line of sight, or by observing the oscillation in intensity produced by the waves. These oscillation are known to have a discrete spectrum (Gough and Toomre, 1991) and can be described by eigenfunctions of the wave equation of a spherical system, therefore can be characterized by the spherical harmonic radial order n, the harmonic degree ℓ and the the azimuthal order m of the oscillation mode. To provide a background for the discussion of local helioseismology, it is compulsory to introduce at least the essential of the global helioseismic theory.

4.2.1 Oscillations and rotational splitting

Small-amplitude oscillations of a spherical star can be separated into normal modes, each of which has a harmonic dependence on time, and depends on the spherical coordinates θ and φ (co-latitude and longitude) as a spherical harmonic.
Therefore, the displacement for a single mode can be written:

$$\delta r(r,\theta,\varphi,t) = Re\left\{\left[\xi_r(r)Y_\ell^m a_r + \xi_h(r)\left[\frac{\partial Y_\ell^m}{\partial\theta}a_\theta + \frac{1}{\sin\theta}\frac{\partial Y_\ell^m}{\partial\varphi}a_\varphi\right]\right]e^{-i\omega t}\right\} \tag{4.1}$$

where a_r, a_θ and a_φ are unit vectors in the r, θ and φ directions, $Y_\ell^m = c_{\ell m}P_\ell^m(cos\theta)e^{im\varphi}$ is a spherical harmonic, as P_ℓ^m is a Legendre function and $c_{\ell m}$is a normalization constant such that the integral of $|Y_\ell^m|^2$ over the sphere is unity. The variation of the displacement with the distance r from the centre is determined by the eigenfunctions $\xi_r(r)$ and $\xi_h(r)$. The mode is characterized by three wave-numbers: n is the radial order which, roughly, gives the number of zeros in $\xi_r(r)$; ℓ is the degree, and m the azimuthal order of the mode. The degree of the mode is related to its horizontal wave-number k_h and wavelength

λ at radius r by:

$$k_h = \frac{2\pi}{\lambda} = \frac{L}{r} \tag{4.2}$$

where $L = \sqrt{\ell(\ell+1)}$. In this description, we neglect processes that damp or excite the oscillations, therefore ω is real, and $\xi_r(r)$ and $\xi_h(r)$ can be chosen to be real. It follows from equation 4.1 that the dependence of the displacement on longitude and time is given by:

$$\cos(m\varphi - \omega t). \tag{4.3}$$

Thus, for $m = 0$ the mode is a standing wave, while for m¿0 it propagates in longitude in the direction of increasing φ (prograde mode), for m¡0 it propagates in longitude in the direction of decreasing φ (retrograde mode).
In general $\omega = \omega_{n\ell m}$, but if rotation and other departures from spherical symmetry are ignored, $\omega_{n\ell m}$ doe not depends on m. In case of slow rotation it is possible to employ a modal description, provided that the rotation axis is chosen as coordinate axis. Therefore, rotation causes a splitting of the frequencies uniformly according to m :

$$\omega_m = \omega_0 + m\Omega \tag{4.4}$$

where Ω is the angular velocity (assumed uniform).
This description explicitly neglects the Coriolis force, since the effect of Coriolis force is considered small. Non-uniform rotation can be treated by replacing Ω in equation 4.4 by a suitable average of the position dependent angular velocity.

4.2.2 Oscillation modes

Employing a standard model for the internal structure of the Sun, it has been shown with linear adiabatic perturbation theory that small-amplitude oscillations of the solar body about its equilibrium state can be classified into three types: pressure modes (p-modes), where the pressure is the dominant restoring force; gravity-modes (g-modes), where gravity or buoyancy is the dominant restoring force; and a class of surface or interface modes (f-modes), which are nearly compressionless surface waves. The p modes are essentially standing acoustic waves; in solar models they have cyclic frequencies between 250 and 5000 μHz. The g modes are standing internal gravity waves with estimated frequencies below the 450 μHz. In the Sun the only modes that have been definitely observed are the so-called 5-minutes oscillations, with frequencies between 1500 and 5000 μHz; these correspond to p modes or, at high degree, also f modes.
P modes are trapped outside a turning point located at $r = r_t$ determined by:

$$\frac{c(r_t)}{r_t} = \frac{\omega}{L} \tag{4.5}$$

where c is the adiabatic sound speed. This corresponds to a point of total internal reflection; for r¿r_t the mode decays exponentially. At the surface the wave is reflected (provided its frequency does not exceed 5500 μHz) by the step density gradient. Thus the wave propagates in a series of bounces between the surface and the turning point. A mode of oscillation, which is a standing wave, is formed as an interference pattern between such bouncing waves. At low degree,

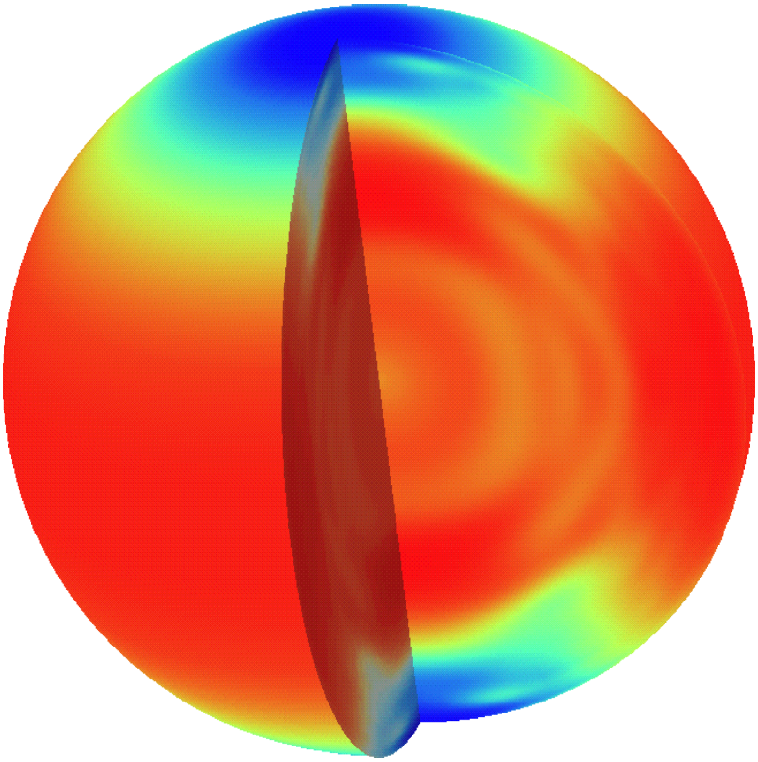

Figure 4.1: Solar non-uniform rotation as retrieved by up-to-date helioseismological measures. Blue denoted slower rotation rate and red faster. Rotation rates span from ~300 nHz at the poles to ~450 nHz at the equator. This image was developed from data acquired using the MDI-SOHO instrument over a period of 12 months ending June 1997.

r_t is small, the modes penetrate effectively into the solar core and hence carries information about the entire Sun. However, the amplitudes are largest near the solar surface and much attention is required to extract that part of information which derives only from the deep solar interior.
Instead, g modes are trapped beneath the solar convection zone, and have large amplitudes in the core, making them potentially very valuable as probes of conditions in the deep solar interior. Unfortunately, their periods are much longer than p mode periods, requiring much longer observational runs, moreover, they have still not undoubtedly detected. Nowadays, most research in global helioseismology is focused on determining the internal stratification and rotation by inverting the frequencies of the modes. This approach has already provided interesting information about the radial structure, large scale asphericity and differential rotation. In the following we focus particularly on the determination of the angular velocity by means of rotational splitting analysis.

4.2.3 An inversion problem

Observation of the rotational splitting for a mode of oscillation provides an integral measure of the angular velocity over the region where the mode is trapped. Because of the variation of the turning point r_t with degree and frequency, different modes sample different parts of the Sun. As a consequence, for example, the difference between m splittings for modes with different r_t should be a measure of the rotation in the region between the turning points of the modes. Therefore, the variation of the splitting degree provides an indication of the variation of Ω with r. The expression 4.4 for the rotational splitting caused by slow uniform rotation is a particularly simple example of a relation between observable properties of oscillation frequencies and properties of the solar interior. Relaxing the condition of uniform angular velocity into $\Omega = \Omega(r)$, the determination of $\Omega(r)$ from $\omega_{n\ell m}$ constitutes an inverse problem.

Inverse problem have a vast literature, covering their application tin geophysics, radiation theory, holography (Parker, 1977; Craig and Brown, 1986), and, of course, helioseismology (Gough, 1978; Christensen-Dalsgaard et al., 1990).

Several inversion techniques for the helioseismic data exist, as an example, here we briefly introduce the *optimally localized averages* method (Backus and Gilbert, 1970).

The inverse problem for a spherically symmetric angular velocity $\Omega(r)$ may be formulated as:

$$\Delta_{n\ell} = \int\limits_0^R K_{n\ell}(r)\Omega(r)dr \tag{4.6}$$

where $K_{n\ell}$ are the rotation kernels

$$K_{n\ell} = \frac{\left[\xi_r^2 + L^2\xi_h^2 - 2\xi_r\xi_h - \xi_h^2\right] r^2\rho}{\int\limits_0^R \left[\xi_r^2 + L^2\xi_h^2 - 2\xi_r\xi_h - \xi_h^2\right] r^2\rho dr} \tag{4.7}$$

and $\Delta_{n\ell}$ is the scaled rotational splitting:

$$\Delta_{n\ell} = \frac{1}{m}\frac{\int\limits_0^R \left[\xi_r^2 + L^2\xi_h^2\right] r^2\rho dr}{\int\limits_0^R \left[\xi_r^2 + L^2\xi_h^2 - 2\xi_r\xi_h - \xi_h^2\right] r^2\rho dr}\delta\omega_{n\ell m} \tag{4.8}$$

(ρ is density and $\delta\omega_{n\ell m}$ are the rotational splittings as functions of n, ℓ and m) in order to obtain:

$$\int\limits_0^R K_{n\ell}(r)dr = 1 \tag{4.9}$$

The principle of the method is to construct a linear combination of the observed data:

$$\hat{\Omega}(r_0) = \sum_{n\ell} c_{n\ell}(r_0)\Delta_{n\ell} = \int\limits_0^R K(r,r_0)\Omega(r)dr \tag{4.10}$$

where

$$K(r,r_0) = \sum_{n\ell} c_{n\ell}(r_0)K_{n\ell}(r) \tag{4.11}$$

with the constrain:

$$\int_0^R K(r,r_0)dr = 1 \tag{4.12}$$

The core of the technique is to choose coefficients $c_{n\ell}(r_0)$ such as to obtain $K(r,r_0) \sim \delta(r-r_0)$.
The coefficients are determined by minimizing:

$$\cos\eta \int_0^R (r-r_0)^2 K(r,r_0)^2 dr + \sin\eta \sum_{n\ell,n'\ell'} E_{n\ell n'\ell'} c_{n\ell} c_{n'\ell'} \tag{4.13}$$

where $E_{n\ell n'\ell'}$ is the covariance matrix of the data. This minimization problem gives a set of linear equation for the $c_{n\ell}$. The effect of the covariance constraint on the minimization is easily understood by considering the case η=0. Minimizing 4.13 subject to 4.12 is essentially searching for the combination of kernels which most resembles to a Dirac function. However, without further constraints, the optimization of the combined kernel may result in numerically large coefficients of opposite signs. Hence the variance in $\hat{\Omega}$, which can be estimated as:

$$\sigma^2(\hat{\Omega}) = \sum_{n\ell,n'\ell'} E_{n\ell n'\ell'} c_{n\ell} c_{n'\ell'} \tag{4.14}$$

would be large. The effect of the second term in 4.13, when η >0, is to restrict $\sigma^2(\hat{\Omega})$. The η value determines the relative importance of the localization and the variance in the result, therefore, providing a sort of trade-off between spatial resolution and error.
A similar inversion problem can be set also for more general angular velocities $\Omega(r,\theta)$, functions of both r and θ. The practical implementation of this procedure is discussed, for example, in (Brown et al., 1989).
The most recent results of global helioseismological inversion of SOHO-MDI Doppler data allowed obtaining solar rotation profiles as function of radius and latitude deep inside the Sun up to r$\sim$0.2R$_\odot$ (Couvidat et al., 2003).

4.3 Local Helioseismology

The first attempts at local helioseismology were really scaled-down versions of the global techniques, in which mode measurements were made over a restricted area. These included the ring diagrams of Hill (1988) and the Hankel function decompositions of Braun et al. (1987).

Recently, different approaches to local helioseismology have been developed, including the helioseismic holography approach of Lindsey et al. (1996), the acoustic imaging technique by Chen et al. (1998) and the time-distance method of Duvall et al. (1993) (See Duvall (1998) for a more extensive review).

In the following, we focus on the time-distance method as an example of local helioseismology.

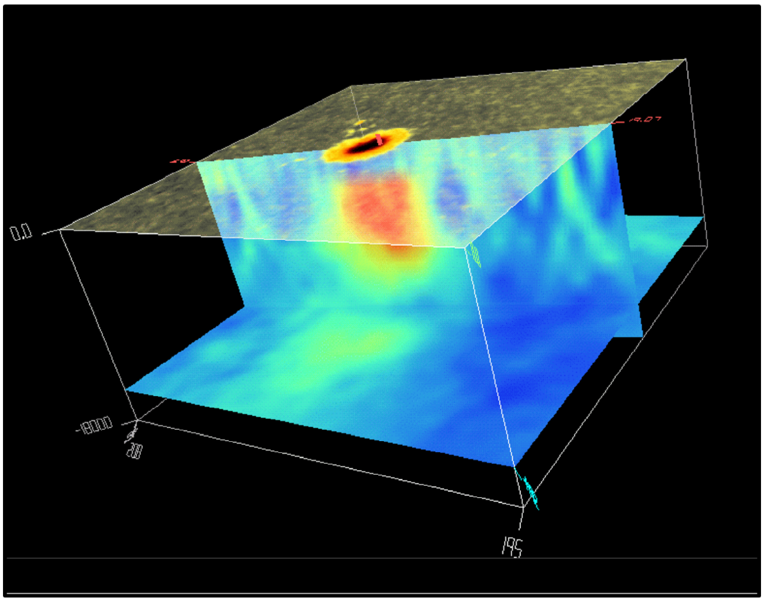

Figure 4.2: Sound speed beneath an active region as recovered by local helioseismological measures. This image was developed from data acquired using the MDI-SOHO instrument in June 1998.

4.3.1 Time-distance Helioseismology

The basic idea of time-distance helioseismology is to measure the acoustic travel time between different points on the solar surface, and then to use these measurements to infer variations of the structure and flow velocities in the interior along the wave paths connecting the surface points. The wave travel time is determined from the cross-covariance function of the oscillation signal between different points of the solar surface (Kosovichev and Duvall, 1997).

$$\Psi(\tau,\Delta)=\int_{0}^{T} f(t,\vec{r}_1)f^*(t+\tau,\vec{r}_2)dt \tag{4.15}$$

where Δ is the angular distance between the points with coordinates $\vec{r}_1$ and $\vec{r}_2$, τ is the delay time, and T is the total time of the observations.
Because of the stochastic nature of excitation of the oscillations, function ψ must be averaged over some areas on the solar surface to achieve a signaltonoise ratio sufficient for measuring travel times τ. The oscillation signal, $f(t,\vec{r})$, is usually the Doppler velocity or intensity.
The oscillation signal is usually filtered to select the pmode or f-mode frequency range using Gaussian transfer function:

$$G(\omega)=e^{-(\frac{\omega-\omega_0}{\delta\omega})^2} \tag{4.16}$$

where ω is the cyclic frequency, ω_0 is the central frequency and $\delta\omega$ is the characteristic bandwidth of the filter. The crosscovariance function represents a solar 'seismogram'. Ideally, the seismogram should be inverted to infer the structure

and flows using a wave theory. However, in practice, like in terrestrial seismology (Aki and Richards, 1980) and oceanography (Munk and Wunsch, 1979), we have to use a different approximation, the most simple and powerful of which is currently the geometric acoustic (ray) approximation. Here, we discuss relations between the modal wave approach and the ray theory.
As already stated, we can represent the solar oscillation signal in terms of normal modes, or standing waves. Using equation 4.15, we express the crosscovariance function in terms of normal modes, and then represent it as a superposition of travelling wave packets. Such a representation is important for interpretation of the timedistance data, and for studying from the data the regional structures in the Sun. The correspondence between the normal modes and the wave packets has been discussed for surface oscillations in Earth's seismology (Ben-Menahem, 1964) and also for ocean waves (Tindle and Guthrie, 1974). Again, to simplify the analysis, we consider the spherically symmetrical case.
Therefore, for a radially stratified sphere, the eigenfunctions can be represented in terms of spherical harmonics, as in equation 4.1.
Then, from the convolution theorem (Bracewell, 1968):

$$\Psi(\tau,\Delta) = \int_{-\infty}^{\infty} F(\omega,\vec{r_1})F^*(\omega,\vec{r_2})e^{i\omega\tau}d\omega \tag{4.17}$$

where $F(\omega,\vec{r_1})$ is the Fourier transform of the oscillation signal $f(t,\vec{r})$, filtered with the Gaussian transfer function in equation 4.16. The time series used in our analysis are considerably longer than the travel time τ, therefore, we can neglect the effect of the window function, and represent $F(\omega,\vec{r_1})$ in the form:

$$F(\omega,r,\theta,\varphi) \approx \sum_{n,\ell,m} a_{n\ell}\xi_r(r)Y_{\ell m}(\theta,\varphi)\delta(\omega-\omega_{n\ell})e^{-(\frac{\omega-\omega_0}{\delta\omega})^2} \tag{4.18}$$

where δ(x) is the deltafunction, and $\omega_{n\ell}$ and $a_{n\ell}$ are the frequencies and amplitudes of the normal modes, respectively.
In addition, we assume the normalization conditions: $|\xi_r(r)|$=1, $\Sigma|a_{n\ell}|^2$=1. Then, the crosscovariance function is:

$$\Psi(\tau,\vec{r}_1,\vec{r_2}) = \sum_{n,\ell} a_{n\ell}[e^{-(\frac{\omega-\omega_0}{\delta\omega})^2-i\omega_{n\ell}\tau}] \sum_{m=-\ell}^{\ell} Y_{\ell m}(\theta_1,\varphi_1)Y^*_{\ell m}(\theta_2,\varphi_2) \tag{4.19}$$

The sum of the spherical function products

$$\sum_{m=-\ell}^{\ell} Y_{\ell m}(\theta_1,\varphi_1)Y^*_{\ell m}(\theta_2,\varphi_2) = \alpha_\ell P_\ell(\cos\Delta) \tag{4.20}$$

where is $P_\ell(cos\Delta)$ is the Legendre polynomial, Δ is the angular distance between points 1 and 2 along the great circle on the sphere, $cos\Delta = cos\theta_1 cos\theta_2 + sin\theta_1 sin\theta_2 cos(\varphi_1-\varphi_2)$ and $\alpha_\ell = \sqrt{4\pi/(2\ell+1)}$. Then, the crosscovariance function in terms of the normal modes is

$$\Psi(\tau,\Delta) \approx \sum_{n,\ell} a_{n\ell}\alpha_\ell P_\ell(\cos\Delta)[e^{-(\frac{\omega_{n\ell}-\omega_0}{\delta\omega})^2-i\omega_{n\ell}\tau}] \tag{4.21}$$

By grouping the modes in narrow ranges of the angular phase velocity, $v = \omega_{n\ell}/\mathrm{L}$, where, as usual, $L = \sqrt{\ell(\ell+1)}$, and applying the method of stationary phase, the cross-covariance function can be approximately represented in the form (Kosovichev and Duvall, 1997):

$$\Psi(\tau,\Delta) \propto \sum_{\delta,v} a_{\delta v} \cos\left[\omega_0(\tau - \frac{\Delta}{v})\right] e^{-\delta\omega^2(\tau-\frac{\Delta}{u})^2} \tag{4.22}$$

where δv is a narrow interval of the phase speed, $u \equiv \frac{\partial\omega}{\partial k_h}$ is the horizontal component of the group velocity, $k_h = 1/L$ is the angular component of the wave vector.

Phase and group travel times are measured by fitting individual terms of Equation 4.22, represented by a Gabor-type wavelet, to the observed crosscovariance function using a leastsquares technique. This technique measures both phase (Δ/v) and group (Δ/u) travel times of the p or f-mode wave packets. The previous time-distance measurements provided either the group time (Jefferies et al., 1994), or the phase time (Duvall et al., 1996).

It was found that the noise level in the phase-time measurements is substantially lower than in the group-time measurements. Therefore, the phase times are more commonly used. The geometric acoustic (ray) approximation is often employed to relate the measured phase times to the internal properties of the Sun. More precisely, the variations of the local travel times at different points on the surface relative to the travel times averaged over the observed area are used to infer variations of the internal structure and flow velocities using a perturbation theory.

In regions of relatively strong magnetic field (sunspot and plages) the acoustic oscillations may experience strong damping which can be due to the interaction with magnetic field, which may lead to transformation of the energy of the acoustic modes into the energy of magnetic modes.

The effect of mode damping can be modelled by adding a damping term, $-\gamma_{n\ell}\tau$, in the square brackets of equation 4.19, where the damping coefficients, $\gamma_{n\ell}$, can be estimated from the power spectra. In quiet sun region, instead, mode damping should not significantly affect travel times of acoustic modes.

In the ray approximation, the travel times are sensitive only to the perturbations along the ray paths given by Hamilton's equations:

$$\frac{d\vec{r}}{dt} = \frac{\partial\omega}{\partial\vec{k}}, \frac{d\vec{k}}{dt} = \frac{\partial\omega}{\partial\vec{r}} \tag{4.23}$$

The variations of the travel time obey Fermat's Principle:

$$\delta\tau = \frac{1}{\omega}\int_{\Gamma} \delta\vec{k} d\vec{r} \tag{4.24}$$

where $\delta\vec{k}$ is the perturbation of the wave vector due to the structural inhomogeneities and flows along the unperturbed ray path, Γ.

Using the dispersion relation for acoustic waves in the convection zone:

$$(\omega - \vec{k}\vec{U})^2 = \omega_c^2 + \vec{k}^2 c_f^2 \tag{4.25}$$

(where $\vec{U}$ is the flow velocity, ω_c is the acoustic cut-off frequency, $c_f^2 = \frac{1}{2}(c^2 + c_A^2 + \sqrt{(c^2+c_A^2)^2 - 4c^2(\vec{k}\vec{c}_A)^2/\vec{k}^2}$ is the fast magneto-acoustic speed, $\vec{c}_A = \vec{B}/\sqrt{4\pi\rho}$

is the vector Alvén velocity, $\vec{B}$ is the magnetic field strength, c is the adiabatic sound speed and ρ is the plasma density) the travel-time variations can be expressed in terms of c, $\vec{B}$ and $\vec{U}$ (Kosovichev and Duvall, 1997).
Assuming that, in the unperturbed state, $\vec{U} = \vec{B} = 0$, we obtain (to the first order approximation):

$$\delta\tau = -\int_\Gamma [\frac{\vec{n}\vec{U}}{c^2} + \frac{\delta c}{c}S + (\frac{\delta\omega_c}{\omega_c})\frac{\omega_c^2}{\omega^2 c^2 S} + \frac{1}{2}\left(\frac{c_A^2}{c^2} - \frac{(\vec{k}\vec{c}_A)^2}{k^2c^2}\right)]ds \qquad (4.26)$$

where $\vec{n}$ is a unit vector tangent to the ray, $S = k/\omega$ is the phase slowness.
The effects of flows and structural perturbations are separated from each other by taking the difference and the mean of the reciprocal travel times:

$$\delta\tau_{diff} = -2\int_\Gamma \frac{\vec{n}\vec{U}}{c^2}ds \qquad (4.27)$$

$$\delta\tau_{mean} = -\int_\Gamma [\frac{\delta c}{c}S + (\frac{\delta\omega_c}{\omega_c})\frac{\omega_c^2}{\omega^2 c^2 S} + \frac{1}{2}\left(\frac{c_A^2}{c^2} - \frac{(\vec{k}\vec{c}_A)^2}{k^2c^2}\right)]ds \qquad (4.28)$$

magnetic field causes anisotropy of the mean travel times, which, allows, in principle, separating the magnetic effects from the variations of the adiabatic sound speed (or temperature).
Typically, times for acoustic waves to travel between points on the solar surface and surrounding quadrants symmetrical relative to the north, south, east and west directions are measured. In each quadrant, the travel times are averaged over narrow ranges of travel distance Δ. Then, the times for northward-directed waves are subtracted from the times for south-directed waves to yield the time τ_{diff}^{NS}, which predominantly measures north-south motions. Similarly, the time differences τ_{diff}^{EW}, between westward and eastward directed waves yields a measure of eastward motion. The time τ_{diff}^{oi}, between outward and inward-directed waves, averaged over the full annulus, is mainly sensitive to vertical motion and the horizontal divergence. The time τ_{mean}, which measures sound-speed and magnetic perturbations is also averaged over the full annulus (for more details see Duvall et al. (1997) and Kosovichev and Duvall (1997)). The next step is to determine the variations of the wave speed, ω, and flow velocity, $\vec{U}$, from the observed travel times using equations 4.27 and 4.28.
It is assumed that the convective structures and flows do not change during the observations and can be represented by a discrete model. In this model, the 3-D region of wave propagation is divided into rectangular blocks. The perturbations of the wave speed and the three components of the flow velocity are approximated by linear functions of coordinates within each block:

$$\vec{U}(x,y,z) = \sum \vec{C}_{ijk}[1 - \frac{|x-x_i|}{x_{i+1}-x_i}][1 - \frac{|y-y_j|}{y_{j+1}-y_j}][1 - \frac{|z-z_k|}{z_{k+1}-z_k}] \qquad (4.29)$$

where x_i, y_j, z_k are the coordinates of the rectangular grid,$\vec{C}_{ijk}$ are the values of the velocity in the grid points, and $x_{i-1} < x < x_{i+1}$, $y_{j-1} < y < y_{j+1}$, $z_{k-1} < z < z_{k+1}$.
So far, most time-distance inversions are done using the ray approximation. The travel time measured at a point on the solar surface is the result of the cumulative effects of the perturbations in each of the traversed rays of the 3-D ray

systems. This pattern is then averaged over a certain number of central points (typically, 4–100), and translated for different surface points in the observed area, so that overall the travel times are sensitive to all subsurface points in the required depth range. The sensitivities of the travel times to the parameters of the discrete model are calculated by averaging equations 4.27 and 4.28 over the ray systems corresponding to the different radial distance intervals of the data, using approximately the same number of ray paths as in the observational procedure.

As a result, two systems of linear equations that relate the data to the sound speed variation and to the flow velocity are obtained, e.g., for the velocity field,

$$\delta\tau_{diff;\lambda\mu\nu} = \sum_{ijk} \vec{A}^{ijk}_{\lambda\mu\nu}\vec{C}_{ijk} \tag{4.30}$$

where vector-matrix $\vec{A}^{ijk}_{\lambda\mu\nu}$ (obtained from solar models) maps the structure properties into the observed travel time variations, and indices λ and μ label the location of the central point of a ray system on the surface, and index ν labels the travel distances.

The spatial resolution of the time-distance inversions based on the ray kernels was studied in 2-D numerical experiments by Jensen et al. (1999). It has been found that shape of the ray-based averaging becomes distorted with depth, which may complicate the interpretation of the inversion results, and that the structures below the lower turning point of the acoustic ray cannot be resolved with the ray approximation. That means that the time-distance data (like other helioseismic data) should not be used for inferring the solar properties below the lower turning points of acoustic waves.

4.3.2 Near surface flows extracted by time-distance Helioseismology

SOHO-MDI full-disk Dopplergrams and magnetograms (Scherrer et al., 1995) were used to derive helioseismographic data for the time period 14 April 1999, 16h UT to 20 April 1999, 16h UT. The region studied was nominally centred at Carrington longitude 180°. Doppler images were calibrated and located in the CCD frame applying the normal MDI pipeline routines. The first step in the analysis was the tracking of the regions to be studied.

Images were interpolated onto Postel's azimuthal equidistant projection (Pearson, 1990) centred on a point in latitude 0°, +40°, -40° and at longitude 180°. The azimuthal equidistant projection is linear in great-circle distance measured from the central point of the projection to outlying points. This projection was used, rather than a longitude-sin(latitude) projection, in order to apply more efficiently the 3-D Fourier filter.

The region was tracked at a rate appropriate for the central latitude and consistent with the supergranule pattern rate measured by Snodgrass and Ulrich (1990). During the time period of the observations, MDI was acquiring both full-disk Dopplergrams and magnetograms with one-minute cadence. The magnetograms were also processed in order to remove cosmic rays and smoothed in time with a three minute median filter and then with a ten minute smoothing filter.

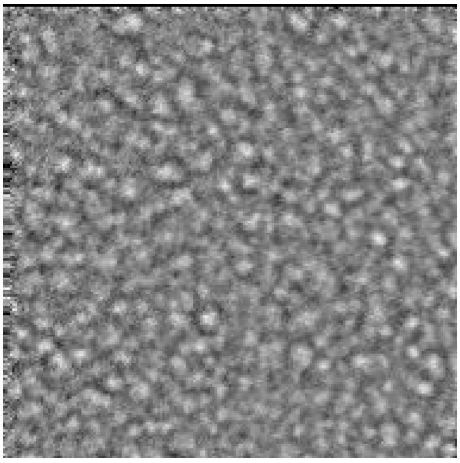

Figure 4.3: An example of the horizontal divergence maps extracted from data acquired from 14 April 1999, 16h UT to 20 April 1999, 16h UT by the MDI-SOHO instrument.

To obtain travel times, the technique described in the previous section was applied, except for the filtering. In fact, for each 8-hour interval, the data-cube was filtered a 3-D Fourier filter that cut off power below 2 mHz, isolated f-modes and filtered the spectrum for a range of horizontal phase speeds.
The resultant spectrum was peaked near $\nu = 2.9$ mHz and spherical harmonic degree ℓ=800. The FWHM were $\Delta\nu = 0.7$ mHz and $\Delta\ell = 400$.
The temporal signal at a spatial pixel is cross-correlated with the signal in the four quadrants of an annulus centred (in arc-distance) on the spatial pixel. These quadrants are centred on the cardinal direction N, S, E, W. For each cross-correlation, the information for waves propagating from the centre to the quadrant is separated from that for waves propagating from the quadrant to the centre, with one showing up at positive shifts of the correlation and the other at negative shifts. Before measuring travel times, average cross-correlation were performed for the waves propagating in the cardinal directions and additional averages were made for waves propagating outwards from the centre and inwards to the centre. As stated in Gizon and Birch (2002) and Kosovichev and Duvall (1997), the difference between outward and inward times should be proportional to the horizontal divergence of the flow. All the cross-correlations for a 2×2 grid of origin were average for each pixel, in order to obtain a suitable SNR. The travel time employed for the inversion was the phase-time. The cross-correlations were then fit by least square to Gabor wavelets. This approach, originally developed for the p-modes only, worked reasonably well also for f-modes.

Chapter 5

Tracking Procedures

This chapter concentrates on the description and comparison of the various techniques used for deriving flow fields from photospheric image timeseries.

The strategy to derive flow fields essentially divides in two subsets: tracking single features and then reconstruct the flow from feature movements, or applying correlation to image subsets in order to directly derive flows.
The archetype of this latter group is the Local Correlation Tracking (LCT), introduced by November (1986) and still widely used.

5.1 Local Correlation Tracking

The LCT technique compares corresponding image parts in two subsequent frames, moving one of them around until the highest correlation with the other one is obtained.

The computed displacement between the two images is then a measure for the velocity of the displayed region of the Sun. In particular, the proper motion is defined as the displacement that maximizes the spatially localized cross-correlation between two frames of a scene separated by a sampling time delay τ that is much smaller than the lifetime of elements in the dataset.

The spatially localized cross-correlation $C(\vec{\delta},\vec{x})$ is therefore a 4-D function: two dimension from the displacement vector $\vec{\delta}= [\ \delta_x,\ \delta_y\ ]$ between the sub-images and the two dimension location $\vec{x} = [x, y]$ of the sub-image centre position. $C(\vec{\delta},\vec{x})$ is defined in terms of the two intensity images $J_t(\vec{x})$and $J_{t+\tau}(\vec{x})$ which sample the dataset at time t and $t + \tau$, respectively:

$$C(\vec{\delta},\vec{x}) = \int J_t(\vec{\xi} - \frac{\vec{\delta}}{2}) \cdot J_{t+\tau}(\vec{\xi} - \frac{\vec{\delta}}{2}) W(\vec{x} - \vec{\xi}) \partial\vec{\xi} \tag{5.1}$$

where $W(\vec{x} - \vec{\xi})$is an apodizing function centred in $\vec{x}$, essentially limiting the integral, analytically defined over the full image, to a restricted area.

The apodizing window size thus defines the spatial resolution of the displacement vector determination. In most of the works employing LCT, such window was taken to be a Gaussian. The maximum of this cross-correlation is a reasonable definition also for the motion of tracers that undergo limited evolutionary changes between two successive image snapshots. Others qualities of this technique are that it is not affected by contrast variations that occur over the area of the apodizing window, the image are compared with the same window attenuation in each displacement $\vec{\delta}$ (due to the symmetry of the Gaussian window), and, as the $C(\vec{\delta},\vec{x})$ is essentially a masked cross-correlation function, a Fourier approach can save lot of computational time.

Of course, this approach requires other effects and movement, such as image drift and seeing motion, to be carefully considered. Before computing the cross-correlation, the images must be spatially filtered to remove any large-scale components, as an intensity gradient over the window usually alters the measured displacement. Spatial filtering to remove scales larger than the apodization window is a practice that can make the measure most sensitive to the horizontal motion of a particular size of tracer (usually the granules).

In order to cope with seeing induced effects, it is favourable to average the cross-correlation in time before locating its maximum: the image products $J_t(\vec{x})$ are averaged in time and the result is smoothed by convolution with the sampling window $W(\vec{x})$. Interpolation in the averaged cross-correlation $\langle C(\vec{\delta},\vec{x})\rangle_t$ in $\vec{\delta}$ is then performed to define the displacement that locally maximizes the cross-correlation in each component of $\vec{\delta}$. As a consequence, only one velocity vector is found for each sub-image used.

It is not possible with LCT to discern velocities resulting from different features in the same sub-image, however it is possible to filter out unwanted spatial scales. The velocity vector stems from a weighted average of the velocities of all the elements present in the sub-image, the weights depending on the elements relative intensity amplitudes and the applied spatial filter scale.

The limits of LCT were pointed out by Roudier et al. (1999), using this technique to reconstruct a synthetic low field to test its ability to restore a given velocity field. They generated an artificial data set where granules were replaced by intensity patterns in the form of ellipses or rectangles. These patterns moved as solid bodies in a pure translational motion; no distortion was introduced. Two frames were extracted from this dataset and the LCT algorithm was applied to them. The result showed that, while recognizing the original flow, some systematic errors were introduced by the processing.

Another peculiarity, already noticed in previous comparisons (Simon et al., 1995; Roudier et al., 1998), was the tendency of LCT to excessively smooth the recovered velocity field.

Their straight conclusion was that mesogranulation, could be a by-product of systematic errors introduced by LCT, because much of the detection of mesogranules was based on divergence measurements (November and Simon, 1988; Muller et al., 1992; Roudier et al., 1998) which were rather sensitive to the way the velocity field was reconstructed.

5.2 Feature Tracking

Feature tracking techniques relay on the idea to track objects advected by an underlying flow which we wish to measure.

The tracked objects are mostly the granules. Of course, granules are not completely passive scalars, but rather coherent structures of turbulent convection, moreover their contour is often undefined and their lifetime is short. Therefore, granules can be used to trace horizontal velocity fields at the sun surface for suitable spatial and temporal scales.

Particularly (Rieutord et al., 2001), granules tend to be Lagrangian tracers when the time and length scales of the flow tend to infinity: proper scale separation is a necessary condition for using granules at representing plasma flows. Quantitatively, the length scale should be larger than 2.5 Mm and the time scale longer than 1h for the correlation to be higher than 0.9. Statistically, they probe a layer 300-400 km beneath the photospheric surface.

Feature tracking techniques can all basically be divided in three steps: feature recognition, movement detection, and field reconstruction. As the most characterizing parts are the first and the last, we concentrate on describing different ways to achieve feature recognition and field reconstruction.

5.2.1 Feature recognition

In order to extract features from solar high-resolution images pattern recognition algorithm must be employed. The identification of a granule strongly depends on the chosen granule-finding algorithm and the definition is a crucial point in each identification technique.

Essentially, two different classes of methods can be employed in order to identify the granules:

- Threshold-based methods,
- Gradient-based methods.

All threshold-based methods are based on exploring a global or local neighbourhood and finding the bright points in the area.

The simplest of these methods is based on pure clipping: defining the granules as the connected areas above some intensity level. This method is very sensitive to intensity variations over the image caused by seeing and solar oscillations. In order to cope with different medium brightness in the images several approaches can be applied.

Roudier and Muller (1987) applied a two-dimensional filter to their images to preserve only those spatial frequencies that are expected to be characteristic for granular structures, so that they could establish a certain threshold to classify the remaining intensity fluctuations as granules or intergranular lanes depending on whether their values lay above or below this threshold. Finally, they rejected all the identified structures whose area was less than 4 pixels.

This same scheme has been used in a modified version, by tuning the filter and the intensity threshold until the result best matched the contours formed by the granular pattern inflection points by Hirzberger et al. (1997, 1999a,b). After filtering and clipping at a threshold equal to the mean intensity value, the resulting granular boundaries are almost identical to granular contours as estimated by an observer via visual inspection.

Another approach was utilized by Title et al. (1989) by searching for local maxima by comparing the brightness of every point in the image with its neighbours. Such a test depended on two parameters: the value of the intensity delta by which a point must exceed its neighbours and the size of the neighbourhood examined.

A similar method was employed by Berrilli et al. (2002), defining a dynamical threshold, to extract compact structures. The procedure was successfully applied both to intensity fields in order to extracted granules and to velocity fields in order to extract upflows. The dynamical threshold value depended on the statistical properties of a moving window centred on the selected pixel. Particularly, they used for a 3"×3" box and an intensity threshold T of the form:

$$T = \langle I_w \rangle + \xi \cdot rms_w \tag{5.2}$$

where $\langle I_w \rangle$ and rms_w denote, respectively, the mean and the rms fluctuations of the intensity in the moving window w, and $\xi = 0.85$.

In order to better adapt to solar intensity features, Bovelet and Wiehr (2001) developed instead a multi-clipping algorithm to perform a photometric 'top-down' approach. Their algorithm started recognizing and labelling structures brighter than an uppermost intensity level. These shapes were extended gradually to adjacent pixels whose brightness exceeded the lower next intensity level. At this lower intensity level a new intensity clip was performed to identify and label fainter structures not recognized by higher clipping. Shapes recognized and extended as intensity levels are lowered, more and more fill the whole image up, while are kept separate by an optional minimum distance of two pixels. This procedure, combining intensity clip, recognition and subsequent extension of shapes, may be repeated until the lowest possible clip or be limited by a 'bottommost' intensity level. However, usually three clip levels proved sufficient to recognize even tiny or complex structures.

Gradient-based methods are built on the idea to detect the image maximum, minimum or inflection points by some operator to define the granules. Alternatively, the Laplacian operator can be applied to the image to determine the zero-curvature points and hold them as the borders defining the granules. Prior to applying such operators, the images usually need to be smoothed to remove the low-contrast granular substructures.

The FT procedure created by Strous (1995) (and developed by Roudier et al. (1998, 1999) and Rieutord et al. (2000, 2001) into the CST procedure) is based on identifying the granules by the local curvature. This criterion uses the intensity of three adjacent pixels to compute a local curvature of the associated quantity (intensity or line-of-sight velocity). This quantity is computed in four directions (x, y and diagonal axis) to get a result invariant under rotations. When the second spatial derivatives have the same sign in the four the pixel belongs to a bright object, otherwise it belongs to a dark intergranule. In order to reduce the noise which could spoil the computation of the curvature, each frame is convolved with a Gaussian window. In addition, they improved the segmentation by applying the opening operator in order to break narrow isthmuses and eliminate thin protrusions.

An approach similar to this one and that of Bovelet and Wiehr (2001) was developed by Berrilli et al. (2005a), who included the image smoothing process in the segmentation procedure by utilizing the Laplacian of Gaussian (LoG) operator. Indeed, the linearity of both the Laplacian and the Gaussian smoothing operators assured the possibility to swap their applying order, and therefore their reduction to a single operator. This approach arose from an analogy with biological sight (Marr, 1982). In biological sight, the scene is examined in a

parallel system analyzing different spatial scales simultaneously.
Those spatial scales are limited by the eye resolution and by the observer's FoV. By focusing its attention to the different resolution scales, the sight process retrieves information about the whole scene or about its details.
In the automated case, instead, the scale range is limited by the device limit resolution and by the FoV dimension (the CCD size). The focusing process can be replicated in several different ways; anyway, in order to maintain the biological analogy, a multiscale approach might be obtained by suitably weighting different scales in the investigated range and looking for maximum correlations. The *LoG* operator,

$$\nabla^2 G_\sigma(x,y) = \quad \Big[\frac{\partial^2}{\partial x^2} + \frac{\partial^2}{\partial y^2}\Big]\Big(\frac{1}{2\pi\sigma^2} e^{\frac{\mathrm{x}^2+\mathrm{y}^2}{2\pi\sigma^2}}\Big) \tag{5.3}$$

also known as *Mexican hat*, can be tuned to a desired scale by varying with its spatial constant σ, without changing its shape.
Therefore, any distinct value of σ in the *LoG* operator corresponds to a different receptive channel and produces a different ROI pattern. The authors found that for solar granulation the significant range of scales was limited between the image pixel resolution and about 1.5 Mm on the solar surface. The σ upper limit was established to force the algorithm to be 'blind' to spatial scales much larger than the typical granular size. In order to establish a rule to weight the patterns obtained with different resolution scales, the authors applied the *spatial coincidence assumption*: *If a zero-crossing segment is present in a set of independent LoG channels over a contiguous range of sizes, and the segment has the same position and orientation in each channel, then the set of such zero-crossing segments indicates the presence of an intensity change in the image that is due to a single physical phenomenon (a change in reflectance, illumination, depth, or surface orientation)* (Marr, 1982) and created a superposition image by summing up each pattern weighted by a function decreasing with σ. In this image, the pixel value tells the frequency of superposition of the zero-crossing borders. The granules are subsequently defined as those structures whose borders at different spatial scales mostly coincide, i.e., whose borders in the superposition image are coincident for more than 63%.

Schrijver et al. (1997), instead, chose to use a 'non-local segmentation algorithm based on the local slope of the intensity', similar to watershed transform algorithm. They used the analogy presented by equating the image intensities with the heights of a mountain area: their procedure arranged pixels into a pattern of 'basins', i.e., areas where rainfall collects at the same point. That accumulation point is found by stepping down from each pixel of the image in the direction of the nearest neighbour with the lowest intensity until a minimum is reached. The starting pixels are labelled and associated to the related minimum, thus defining the cells as areas with the same accumulation point. For the segmentation of granulation fields, the algorithm was applied to negative broadband intensity images.

Another definition of granular cell was used by Hirzberger et al. (1997) to select the granule and its corresponding part of the intergranular lane. They drew a line along the intergranular lanes so that the borders of the adjacent granules remained equidistant to this line, disregarding the intensity distribution. With this method, just by splitting the intergranular lanes into two halves, they obtained one intergranular area corresponding to each granular area. Thus, it was possible to define granular cell areas as a simple sum of granular and intergranular areas.

A hybrid approach was instead developed by Florio and Berrilli (1998), namely the i-MAT procedure. This algorithm, based on an iterative procedure of Medial Axis Transform (MAT) (Blum, 1967), considers grey-level information at the pixels along the selected regions to extract reticular structures. The authors' approach was to reduce photospheric and chromospheric patterns into 1-pixel broad graphs or skeletons and introduced an iterative scheme in the original Zhang and Suen (1984) algorithm in order to take into account grey-level information of the input image.

The skeleton of an image, as discussed in Gonzalez and Wintz (1987), may be defined via the MAT, retaining the topology, extension and connectivity of the investigated region while throwing away most of the pixels belonging to the input foreground structure. The MAT of a region R could be defined in the following way: $\forall p(x, y) \in$ R, its closest neighbour in the region boundary B is searched, if $p(x, y)$ has more than one such neighbour, then $p(x, y) \in$ MAT. In particular, the authors applied the MAT algorithm published by Zhang and Suen (1984) and reported in Gonzalez and Wintz (1987).

To start their algorithm a binarized representation (provided by the same dynamic threshold discussed above) is obtained from the original image and then the closing operator is applied in order to fill in small holes.

The thinning rule of Zhang and Suen (1984) is applied to this image and the retrieved skeleton is stretched in order to adjust itself with respect to the grey-level information of the input image. Then the dilation operator is applied to this skeleton and the 'dilated' image is used as starting binarized image of the next iteration. The iterative process stops when changes on a new skeleton became negligible to respect to the previous one. Moreover, they introduced pruning rules to eliminate undesired *branches*, i.e. part of the skeleton connected by only one junction. The identified reticular structures were then used as the boundary for granular cells.

5.2.2 Movement detection

The position of a segmented object is usually represented by a single point: its geometrical centre, its gravity centre or its extreme in the associated quantity. In general, an object in an image can be identified with an object in the next image by distance or superposition or shape comparison criteria, i.e., if the distance between the representing points does not exceed a fixed maximum displacement, or if there is a minimum overlap of the objects in the two images but no overlap with other objects, or if the shapes of the two objects match above a minimum correlation threshold.

In most cases, in order to cope with spurious movement induced by seeing or instrumental effects, a temporal average of object positions or displacements is performed. Such temporal average must be performed on several images in order to recover a statistic representative of the mean position. This is often the limiting factor for time resolution in horizontal velocity fields recovered by feature tracking.

Complications in movement detection often arise when an object in an image splits up in two objects in the next image. Adopted solutions again vary from procedure to procedure, with some authors disregarding the splitting object at the moment they split (Strous, 1995), some authors linking the old object with the greater or longer-lasting fragment (Hirzberger et al., 1999a), and some authors applying superposition or shape comparison criteria (Del Moro, 2004).

More in particular, Strous (1995) associated the position of a to-be-tracked object by the position of its maximum, therefore connecting this object to an object in the next frame if the distance of their maximum positions did not exceed 1 pixel or if there were at least 1 pixel overlap between the two shape and no overlap at all with other shapes. The author justified the 1 pixel per frame fixed limit in order to exclude structure movements faster than $\sim 6km \cdot s^{-1}$.

The more sophisticated method of Hirzberger et al. (1999a,b) can be split into three consecutive steps. The starting point of this procedure is to randomly select several granules in each image and track them forward or backward in time. In order to follow the same granule, the algorithm computes the centre of mass of the overlap region for the target granule shape in the last five frames. The granule that is closest to this centre of mass is then considered as the granule being tracked.
The tracking stop conditions are obtained by ruling out the structures which move faster than sound speed or deform too much due to real evolution or seeing induced distortion. Therefore, for each tracked structure in a particular frame, the algorithm computes the correlation between the area around the overlap region (as defined above) and a square box centred on the tracked structure in the frame were it was first identified. Subsequently, the mean value of the correlation matrix is calculated, and the tracking process is immediately stopped if this value is smaller than a fixed threshold or if the sum of the mean values of the last five frames is below another threshold.
However, when a granule splits into two or more parts, the resulting portions form a group whose global shape may resemble that of the former structure. Thus, the correlation between images would not necessarily drop to very low values (equivalent considerations are valid for the merging process). In order to deal with this effect and detect rapid changes in structure areas, the authors assumed a simple functional form to be able to model the size evolution of each granule. Specifically, the procedure extrapolates a second-order polynomial fit to the structure area in time and considers acceptable values those within 2σ from the expected value. Then, if more than four consecutive area points are detected beyond the 2σ limit, the tracking is stopped.

The Two-Level Structure Tracking (TST henceforth) procedure, developed by Del Moro (2004), employs a different approach to detect structure movements and achieve tracking. In detail, starting from the first image of the temporal series, the algorithm selects all the binarized structures and tracks them forward in time. Preliminarily, the algorithm computed the $Perimeter^2/(4\pi \times Area)$ ratio for each structure and retained for tracking only those whose ratio was below a fixed threshold. Then, for each structure, a circular region, centred in its barycentre and with a 5" radius, is defined. All the structures of the next image, whose barycentres are inside this region, are compared in shape with the target structure. The one, whose shape closest matches, within a maximum allowed deformation value (10%), is retained and considered as the evolution of the target structure, otherwise the lineage ends. Once all the structures of the actual image have been processed, the TST proceeds to the next, considering all the structures which have not yet been identified as evolutions of previous images granules. With these rules a granular lineage ends as the structure becomes too small (fading) or too large (merging), or it warps too much or too fast (merging or exploding events). In this way the TST procedure generates a database whose entries are ordered by structure number, containing the related structure characteristic at a fixed time. This process is repeated until the last structure in the last image is reached.

5.2.3 Field reconstruction

All feature tracking procedures return a spatially and temporally randomly sampled velocity field, as they depend on trackers position and existence to sample the plasma flows. As a result, a crucial difference between algorithms stems from the transformation of a randomly sampled field to a regular one.

Again, different solutions were implemented by different authors.

In particular, Strous (1995) employed an averaging method to reconstruct the field from the displacements retrieved by FT: he divided the field into boxes approximately 4 Mm wide, simply taking the average of the values of the horizontal velocity which fell in the box in a fixed time interval and thus reconstructing a coarse-grid time-averaged velocity field. Whenever the grid was too fine with respect to the data or the time interval too short, some points were devoid of data. Once the velocity field was reconstructed, they derived the divergence using simple differences between neighbouring points. Such approach, unfortunately, did not exploit distance information nor gave an estimate of retrieved field errors.

Instead, Roudier et al. (1998, 1999) and Rieutord et al. (2000, 2001) have developed two different approaches to the problem within the CST procedure. In the first approach, they figured out that the measure of the velocity components in one site could be completed by the size of the structure used to perform the measurement. Thus, for each point where the velocity is measured, a smallest scale could be defined, so that when reconstructing the field a weighting function for the grid-regularizing process can be characterized. However, in their work (Roudier et al., 1999), they divided the field into equal boxes, we simply taking the average of the values of the horizontal velocity which fell in the box and reconstructing a coarse-grid velocity field.

The second approach was to apply the Local Correlation Tracking to the segmented data as a displacement computing and interpolating procedure. LCT, as described in 5.1, provides a uniformly sampled velocity field and immediately produces 'gridded data'. The author stated that in this way, some problems and sensitivities of the LCT can be avoided. In particular, by applying LCT to already segmented data internal intensity fluctuations, which may be residues of seeing or of 5 min-oscillations, are removed, moreover, the noise classically attributed to granular motion was also reduced. The size of the Gaussian window for the LCT procedure was chosen according to Shannon's criterion: the authors motivated that, since granules are constraining the sampling of data, the window size should be half of the granules' mean size. Utilizing the granular mean size of Roudier and Muller (1987), they therefore choose a window size of 0.700 (5 pixels). By using this spatial sampling, they verified that temporal windows as short as five minutes can be used, suitable to follow the time evolution of the velocity field and of the granules.

An alternative solution was provided by Del Moro (2004), by applying Delaunay linear interpolation to the randomly sampled field in order to recover an evenly sampled grid. The Delaunay linear interpolation weighted the contribution of the sparse sampled points by their distances from the new array intersections and from such distances it was also possible to assess the accuracy of the result.

5.2.4 TST versus CST: a comparison

In order to achieve a deeper insight of Feature Tracking techniques, we present here a comparison of TST and CST characteristics. Both algorithms retrieve the horizontal velocities by tracking the displacements of 'coherent features' (granules), identified by their centre (i.e. without intensity information) in the CST case, or by their intensity barycentre in the TST case. The structures are identified by different methods: CST structures are recognized by searching for the zeros of the second derivative of the intensity field and then by applying both a Gaussian smoothing window to remove noise and an Opening operator in order to remove isthmuses and protrusions. TST structures are instead retrieved by recognition of clusters of pixels which are brighter than their surroundings. Both methods avoid problems caused by large scale intensity variations and efficiently retrieve segmented granular patterns. A common element of both procedures is the evaluation of the regularity of segmented structures by a morphological describer, in order to discriminate true motion from spurious barycentre movement due to structure deformation. This is a crucial point for both procedures: for TST, because tolerating too much structure deformation would forbid discriminating spurious barycentre movement from true structure motion, much more for CST, which relies on minor morphologic changes of structures from one frame to the other. In fact, CST reconstructs granule lineages by searching the surroundings of the barycentre position between successive images and hence would be sensitive to splitting and merging events. TST, instead, while still requiring barycentre proximity in consecutive frames, validates the detection by comparing the structure shapes. Moreover, in order to cope with seeing-induced motion, barycentre positions are averaged over 30 seconds before computing their displacements. However, the most crucial difference is in the field reconstruction, as the transformation of a randomly sampled field to a regular grid can introduce undesirable elements originating from the interpolation algorithm itself. In order to retrieve the uniformly sampled field, the CST algorithm computes the average of the values in an established neighbourhood, therefore not exploiting the distance information. As an alternative solution, the field is reconstructed by using LCT, with a Gaussian averaging window of about half the granules' mean size. The TST procedure instead approximates grid values by Delaunay linear interpolation, thus weighting the contribution of the sparsely-sampled array points by their distances from new grid junctions; moreover, the accuracy of the result can be estimated as a function of the distance from sampling points.

Figure 5.1: The Swedish Vacuum Solar Telescope at La Palma (Spain).

5.3 Applying TST to Granulation and Supergranulation Datasets

We present here some results obtained by applying TST to a flow-map series extracted from MDI data and to a broadband granulation time series acquired at La Palma.

5.3.1 Flow field retrieved from broadband Granulation time-series by TST

The quiet granulation time series (hereafter SVST95) was acquired at the Swedish Vacuum Solar Telescope (Roque de los Muchachos, La Palma, Spain) on June 30, 1995 (from 10:34 UT to 12:50 UT). The series is made up of 220 broadband (central wavelength 525.7 nm, band-pass 3 nm) images with field of view of 18 " × 18 ", (290 × 290 pixels), each taken with an exposure time of 0.011 s. After the standard corrections this series was sub-pixel re-centred, destretched and treated with a $k_h - \omega$ (cut-off velocity 4 $km \cdot s^{-1}$) and a restoration filter. For a more detailed description of this dataset refer to Sobotka et al. (1999). When applied to the SVST95 dataset the TST procedure tracked 1713 granular lineages.

Horizontal velocity fields

As reported in Roudier et al. (1999); Rieutord et al. (2001), the plasma flows can be correctly reconstructed by tracked granules only for spatial scales larger than 2.5 Mm and for temporal scales longer than 30 minutes, otherwise the derived flow would be spoilt by the granule velocity field. Nevertheless, we chose to compute the velocity fields at higher rate and resolution, because we are also interested in the granule proper displacements. The plasma flow can still be obtained by successively averaging the velocity fields, in order to reach

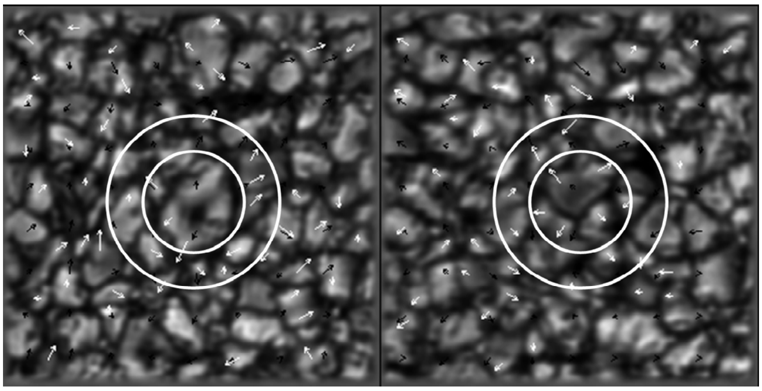

Figure 5.2: A pair of original broad-band SVST95 images, with horizontal velocity field superposed. White arrows represents velocity vectors computed from actual granules displacements, black arrows represent the interpolated velocity field. In the centre of the upper image an exploding granule just after fragmentation is visible. The two extracted velocity fields are 4 minutes apart. It is evident how the explosion event affects the movement of the nearby granules.

the required time and spatial scales. In Fig. 5.2 we present a pair of horizontal velocity fields (both the sparse array (white arrows) and the interpolated one (black arrows)), separated by 4 minutes.

Examining the reconstructed horizontal velocity fields obtained by the TST, we found several roughly ring-shaped structures of divergent flow vectors, corresponding to exploding granules, due to the interaction between the exploder expansion and its neighbours, lasting for several minutes. The pair of images reported here shows an example of such structures.

The interaction of the exploder with its neighbours is highlighted by the pairs of white rings: in the first image the exploder (in the inner circle) has just fragmented and its expansion is now dislocating its neighbours (in the space between the circles). In the second image the TST has already recognized and tracked the five heir fragments (in the inner circle), whose barycentres are the origins of the white arrows and which are still receding from each other; the granules in the space between the circles seem still displaced or at least deflected from the fragments and in the lower-right part a broad intergranular lane has formed. We can therefore define as the typical interaction length for exploders the radius of the outer circle, which is about 4 arcsec. Taking into consideration that a) only very big granules explode, and b) the greater the granule the longer its duration (Hirzberger et al., 1999a; Del Moro, 2004), we can now conclude that these interactions may very well persist several minutes (typically ten-twelve), and may repeat at or very near the same location because, frequently, exploder's fragments undergo repeated fragmentation (Carlier et al., 1968; Roudier et al., 2003).

Even though it cannot be excluded that exploding granules have a tendency to rise near the centre of mesogranular convective cells, whose flow may help them expand, the probable cause of the divergence signal is the exploding granule, as the exploder's fragments are moving with velocities of ∼1 km$\cdot s^{-1}$ at least and up to ∼7 km$\cdot s^{-1}$ (see Hirzberger et al. (1999b) and references therein), while the divergence due to mesogranulation is $\sim$1 km$\cdot s^{-1}$ at most and peaked around 0.5 km$\cdot s^{-1}$ (November and Simon, 1988; Roudier et al., 1998).

Granule lifetime distribution

Another output of the TST are the lifetimes of granules, which can be obtained measuring the time elapsing between their birth and death, deriving the distribution functions reported in Fig. 5.3.
The TST stringent birth and death conditions, set in order to retain only very coherent structures, define a different 'granule' to that used in literature works. As in the case of Roudier et al. (1999), the obtained lifetime is a coherence time scale rather than the proper structure duration.
Following Title et al. (1989) and Roudier et al. (1999) we chose to fit the histograms with a decaying exponential law

$$N(t) = N(0)e^{-t/\tau} \tag{5.4}$$

(Alissandrakis et al., 1987), reported as black dotted and dashed lines in Fig. 5.3, to estimate mean lifetimes, as for a decaying exponential distribution $\bar{t} = \tau$ (Hirzberger et al., 1999a).
Regrettably, this function seems unable to represent the reported lifetime distributions, either for short or for long granule duration. In fact, as can be seen in Fig. 5.3, the decay law of lifetimes seems to be at least twofold, indicating different regimes for $t <\sim 2.5$ or $t >\sim 2.5$ minutes. This double exponential behaviour could account for the presence of at least two different granular populations: a bulk with a very short mean lifetime ($\bar{t} \sim 1$ minute) and a minority with a longer mean lifetime ($\bar{t} \sim 3/4$ minutes).
A comparable distribution is reported by Brandt et al. (1991), and a closer look at the granule lifetime distributions in Title et al. (1989) reveals a similar excess of short lived granules in four out of six reported lifetime histograms.
We observe that granule lifetime histograms may be properly approximated by a stretched exponential (Williams and Watts, 1970) function (continuous line in Fig. 5.3):

$$N(t) = N(0)e^{-(t/\tau_{se})^{\alpha}} \tag{5.5}$$

The parameters τ_{se} and α are a decay time (although not directly related to granule mean lifetime) and a dispersive factor, respectively. Values of $\alpha < 1$ correspond to the existence of a broad distribution of lifetimes which describe the elementary relaxation process. In this framework, the lifetime histograms suggest that we cannot define a typical lifetime for granules, which instead show a continuous distribution of decay times. Here, we report the exponential fits and the stretched exponential fit parameters for the dataset.

5.3.2 Supergranulation parameters from MDI time-distance near-surface flow-maps extracted by TST

The divergence signal maps used in this analysis are described in 4.3.2 and in paragraph 2 of Duvall and Gizon (2000). The application of the TST procedure to this dataset led to identification of 548 SG structures lasting for at least two images.

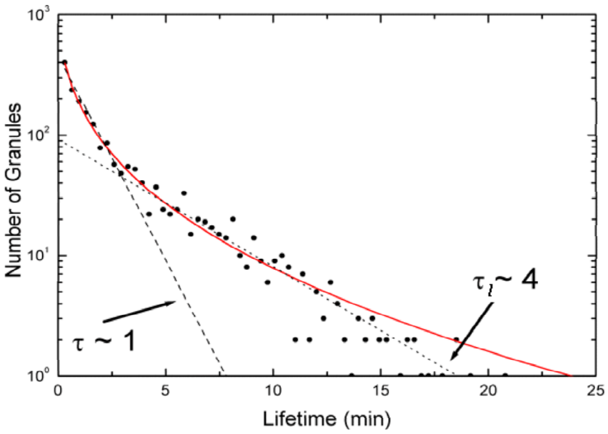

Figure 5.3: Histograms of granule lifetime from the SVST95 series. Dotted and dashed black lines are exponential decay fits for the whole distribution (deriving $\tau \sim 1$) and for points with $t \geq 5$ (deriving $\tau_l \sim 3.5$), respectively. The continuous line is stretched exponential fit to the data (cfr. Eq. 5.5).

τ (min)	τ_l (min)	α	τ_{se} (min)
1.3 ± 0.05	3.6 ± 0.2	0.37 ± 0.02	0.10 ± 0.03

Table 5.1: Fit parameters: we report the values of the significant parameters of the fits: τ is the decay time for an exponential fit taking into account all the points of the lifetime histogram; τ_l is the decay time for an exponential fit taking into account only lifetimes $\geq$ 5 min.; α and τ_{se} are the relaxation parameter and the decay time for the stretched exponential fit, respectively.

Supergranulation lifetime distribution

The scheme adopted to study the lifetime of SG features is similar to that applied to granular structures: the mean lifetime τ_{SG} can be derived using an exponential fit to the lifetime histogram of tracked structures.
In Figure 5.4 we report the number of supergranules versus their lifetime. An exponential decay law fits the data very well (R2 = 0.998) and we derive $\tau_{SG} =$ 1065 min (18 hours) as the estimated mean lifetime. In order to check the effect of the length of the data sample (6 days) on the estimated value τ_{SG}, we studied this effect on the SVST95 granulation time series via the TST procedure. In this case we already know that the granular lifetime ($\tau_l = 3.6$ min) is much shorter than the whole dataset duration (75 min). Therefore we can to derive the τ_l as a function of the temporal window. The result of this analysis is reported in Figure 5.5. Therefore, we can be confident about the lifetime value only when the observation period is much greater (=10 times) than the τ_g. From the Figure 5.5 plot it can be estimated an upward adjustment of about 20% for the supergranulation lifetime. By applying this correction to the previous τ_{SG}, an actual value of $\tau_{SG} \sim 22$ hours is retrieved.

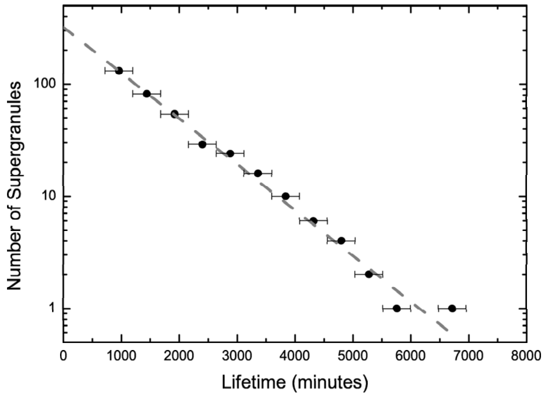

Figure 5.4: SG number (black dots with error bars) vs their lifetime and an exponential decay fit (dashed line).

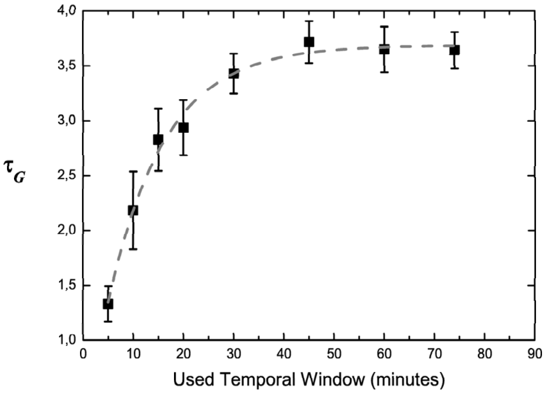

Figure 5.5: τ_l values (black squares with error bars) vs time series length calculated for SVST95 dataset. An exponential growth fit (dashed curve) is superimposed. The asymptotic value of τ_l is 3.6 min and it is reached using datasets longer than 40 min.

Chapter 6

2-D Multiline Spectroscopy

The spatial and temporal behaviour of photospheric convective flows strongly influences the arrangement and evolution of magnetic elements emerging on the solar surface, contributing in the assembly of magnetic features which modulate the solar energy output. On the other side, local magnetic field clustering reduces the efficiency of convection. Therefore, a complete insight of the dynamics of the plasma flows and their interaction with magnetic fields is essential to fully understand solar convective layer.

This chapter will introduce the reader to the use of spectroscopic imaging to retrieve information on solar photospheric layers dynamics. In particular, we will describe some techniques for characterizing the structure and dynamics of photospheric velocity and intensity features at different scales and heights in the solar atmosphere. Moreover, we will present some recent results about the interaction between photospheric velocity field and magnetic elements, obtained from high spatial, temporal and spectral resolution observations, which allowed a tentative 3-D reconstruction of the photospheric velocity field.

6.1 Line Sensitivity to Solar Magnetic Regions

Since all of our information about the solar atmosphere is carried to us in one form or another by the radiation field, it is necessary to understand how various physical processes imprint themselves upon the emergent radiant intensity. Among such process, we are particularly interested in the interaction of solar magnetic field small scale features with radiation fields. The essential physical concepts and the observational techniques which underlie the inference of solar magnetic fields through spectropolarimetry were reviewed by Lites (2001).
Observations have established that the photospheric magnetic field is organized in small fibrils or flux tubes. In these elemental structures, the magnetic field intensity is strong enough to control the local environment, but the flux tubes have a group behavior controlled by the photospheric convective patterns. Flux tubes are the most likely channels for transporting energy into the upper atmosphere, and thereby also influence the solar irradiance.

Following Spruit (1981), we will derive the differences of thermodynamic conditions inside and outside the magnetic flux tube. Neglecting viscosity and resistivity, the equation of motion for a fluid with an arbitrary magnetic field configuration is:

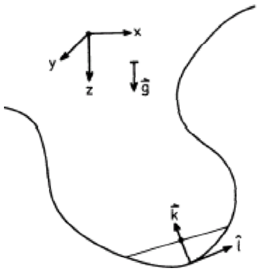

Figure 6.1: Notations and coordinate frames used for the description of a flux tube: $\vec{l}=$ unit vector along the flux tube; $\vec{k}=$ curvature vector.

$$\rho\frac{d\vec{v}}{dt} = -\nabla(p+\frac{B^2}{8\pi}) + \frac{1}{4\pi}(\vec{B}\cdot\nabla)\vec{B} + \rho\vec{g} \tag{6.1}$$

where ρ is the density, p the pressure, $\vec{B}$ the magnetic field and $\vec{g}$ the acceleration of gravity. Since the Lorentz force is perpendicular to $\vec{B}$, the component of $\rho\frac{d\vec{v}}{dt}$ parallel to the tube axis is:

$$\rho(\frac{d\vec{v}}{dt})_{||} = -\partial_l p + \rho\vec{g}\cdot\vec{l} \tag{6.2}$$

where $\vec{l}$ is the unit vector in the direction parallel to the flux tube axis and $\partial_l = \vec{l}\cdot\nabla$. The component of $\rho\frac{d\vec{v}}{dt}$ perpendicular to the tube axis is, instead:

$$\rho(\frac{d\vec{v}}{dt})_{\perp} = -[\vec{l}\times\nabla(p+\frac{B^2}{8\pi})]\times\vec{l} + \frac{B^2}{4\pi}\vec{k} + \rho(\vec{l}\times\vec{g})\times\vec{l} \tag{6.3}$$

The vector $\vec{k} = \partial_l\vec{l}$ is perpendicular to $\vec{l}$ and is the *curvature* of the path of the tube. Assuming pressure equilibrium between the inside of the tube and its surroundings, on a horizontal plane within the tube (perpendicular to $\vec{g}$), we have that $p+\frac{B^2}{8\pi}$ is constant and equal to the external pressure p_e. Consequently, we have:

$$\nabla(p+\frac{B^2}{8\pi}) = \nabla p_e = \rho_e\vec{g} \tag{6.4}$$

where ρ_e is the density of the external fluid. The force $F_\perp$ acting perpendicular to tube axis is then:

$$F_\perp = \frac{B^2}{4\pi}\vec{k} + (\rho-\rho_e)(\vec{l}\times\vec{g})\times\vec{l} \tag{6.5}$$

The magnetic pressure exerted by the field concentration perpendicular to the magnetic lines of force is balanced by a reduced density of the atmosphere inside the tube relative to the surrounding, embedding atmosphere. Such a partial evacuation reduces the opacity of the atmosphere and as a consequence, isosurfaces of optical depth are depressed at the location of the flux tube. Moreover, thermodynamic variables for the atmosphere inside the tube differ substantially from the surroundings' atmosphere, consequently affecting the radiative transfer process. In particular, changes in the thermodynamic structure of solar regions induced by the magnetic field, produce visible brightening or darkenings at specific spectral ranges (Penza et al., 2004).

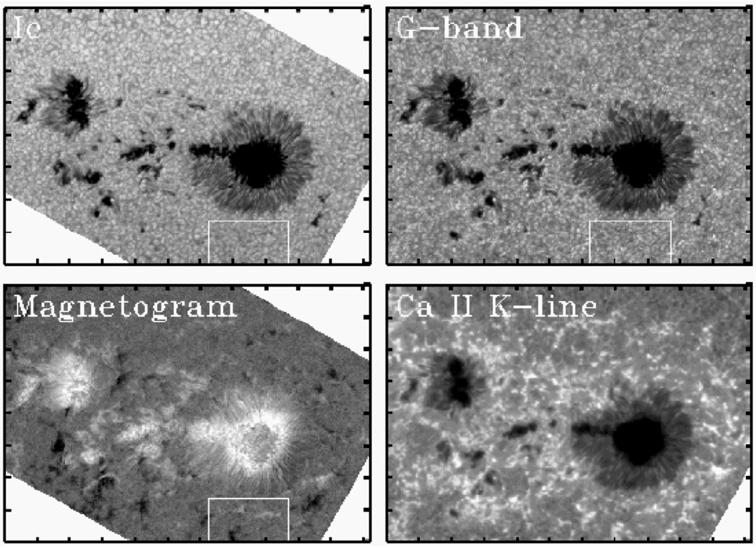

Figure 6.2: Active region 8218 observed on 13^{th} May 1998. Top left panel: intensity continuum. Top right panel: G-band. Bottom left panel: magnetogram. Bottom right panel: Ca II K line. Thick marks are 10" apart.

As a matter of fact, several spectral bands have proved to be good proxy for the photospheric magnetic field. As a consequence, regions of enhanced magnetic fields are often identified by detecting appropriate features on spectral images. For example, the solar chromosphere as displayed by the Ca II H and K resonance lines at $\lambda = 396.849$ nm and $\lambda = 393.368$ nm, or the Ca II infrared triplet near $\lambda = 854.2$ nm shows the irregularly patterned chromospheric network (Skumanich et al., 1975b; Engvold, 1966; Brown, 1975; Chapman et al., 1988). Several works confirmed the correspondence of such a pattern with sites of enhanced magnetic field (Lites et al., 1999). Observations at very high spatial resolution within the so-called $G - band$, formed by the CH lines around $\lambda = 430.5$ nm, shows the granulation pattern with very small (< 0.1") bright grains advected by the convective flow (Muller and Roudier, 1984; Muller, 1985; Steiner et al., 2001; Sánchez Almeida et al., 2004). Such '*bright points*' are at present believed to be the manifestation of the smallest scale magnetic flux concentrations (Berger et al., 1995; Berger, 1996; Berger and Title, 2001; van Ballegooijen and Nisenson, 2002).

As already stated, the flux tubes are advected by the horizontal flows of the granular pattern and possibly concentrated in high flux structures by converging motions due to strong down-flows (Berger et al., 1998). As a consequence, the magnetic network is thought to be the accumulation of small scale flux tubes on the borders of cells produced by the convection. Whether such an accumulation would be the result of the expulsion of flux tubes from a single convective cell (a supergranule) or the effect of the collective action of smaller scale convective cell (the granules) giving rise to a preferential magneto-convective scale, is still not ascertained. Recent models by Rast (2003b) and Rast et al. (2004), taking into account a purely advective interaction between downflows, predict the formation of strong downflows at the vertices of supergranules due to the clustering of feebler granular-scale downflows. Instead, observations of very energetic divergence events, probably responsible of mesogranular scale signal, lead Rieutord et al. (2000) to formulate the hypothesis that also supergranulation may be driven by strong granular-scale divergence at the centre of the supergranular cell. Whatever the case, the net result of the accumulation of magnetic elements on the borders of supergranules is a bright magnetic network, visible in the Ca II and other 'magnetic' lines (Berrilli et al., 1999), which outlines the supergranules (Venkatakrishnan, 1984). Exploiting such a relationship, it is possible to detect supergranular cells using the network as a proxy.

6.2 Magnetic Network Dynamics in Photosphere

As stated in the previous section, the interaction between moving plasma and solar magnetic field determines the spatial configuration of enhanced magnetic field in the outer layers of the Sun. In particular, the concentration of magnetic small scale structures on the borders of convective cell produces the magnetic network. These network structures are associated in the photosphere with bright elements, whose dynamics is determined by granular flows. These bright elements are thought to be single or small groups of small flux concentrations or, so called, magnetic elements. The enhanced brightness of these magnetic elements make it possible to easily identify supergranules.
In order to investigate the interaction between photospheric dynamics and small-scale magnetic features, Berrilli et al. (2005b) studied the line-of-sight plasma velocity and line core intensity associated to magnetic features, confirming the strong correlation between magnetic fields, downflows and modification of line parameters.

In particular, on 16^{th} October 2003, they observed a roundish network cell from 14:24 to 17:32 UT. The observation was carried out with the IBIS 2D-spectrometer (cfr. 2.3) installed at the Dunn Solar Telescope, Sacramento Peak, NM, USA. The dataset consisted of 600 sequences containing a 16 points scan of the Fe I 709.0 nm line, a 14 points scan of the Fe II 722.4 nm line, and 5 spectral images in the wing (line center + 12 nm) of the Ca II 854.2 nm line. The time necessary to acquire a sequence was $\sim$ 19 s. Each monochromatic ($\Delta\lambda = 5$ pm) image was acquired with 25 ms exposure time by a CCD detector, whose pixel scale was 0.17" $\cdot pixel^{-1}$. Each image was corrected for CCD non-linearity effects, dark current, gain table, monochromatic flat-field and blue shift (Reardon and Cavallini, 2003). Vertical velocity fields were computed for the FeI and Fe II lines by computing the Doppler shift: for each pixel a Gaussian fit of the line profile was evaluated. The shift of this Gaussian function relative to a reference mean line profile produced the Doppler shift, while the amplitude of the Gaussian produced the center line intensity fields. The 5-minutes oscillations were removed from the velocity fields applying a 3-dimensional Fourier filter in

Figure 6.3: The Dunn Solar Telescope telescope at Sacramento Peak, New Mexico (USA).

the $k_h - \omega$ domain with a cut-off velocity of $7km \cdot s^{-1}$. Finally, the velocity fields, the line core intensities, the Ca II wing images and a reference continuum image were recentred to a common frame. After the whole reduction procedure, the effective FoV was approximately 51" × 51". Atmospheric seeing strongly affects the effective resolution of the data. In Figure 6.4 is reported the trend of the image quality for a part of the dataset. In order to improve the analysis significance, only some images in the dataset (correspoinding to the red points in Figure 6.4) were selected. The selection was carried out by picking images with the best seeing condition and with a constant time-gap of 10 minutes, in order to have fully independent granulation patterns.

An example synoptic panel of the dataset is reported in Figure 6.5. It is worth to notice how the core intensity of the Fe I 709.0 nm line correlates with magnetic features as identified by the Ca II wing image.

The Contribution Functions for Fe I 709.0 and Fe II 722.4 lines were calculated by Penza et al. (2004), the major contribution to the formation of these absorption lines comes from layers 100 km and 200 km above the photospheric surface, respectively. The Ca II 854.3 line wing observed in this analysis is also essentially formed in the high photosphere (200-300 km) (Qu and Xu, 2002), therefore bright feature on this image can be associated with photospheric magnetic structures. In order to extract such structures, the authors studied the Intensity Distribution Functions (IDFs) of each Ca II image. As the IDFs presented a bimodal distribution, evidence of two separate populations associated

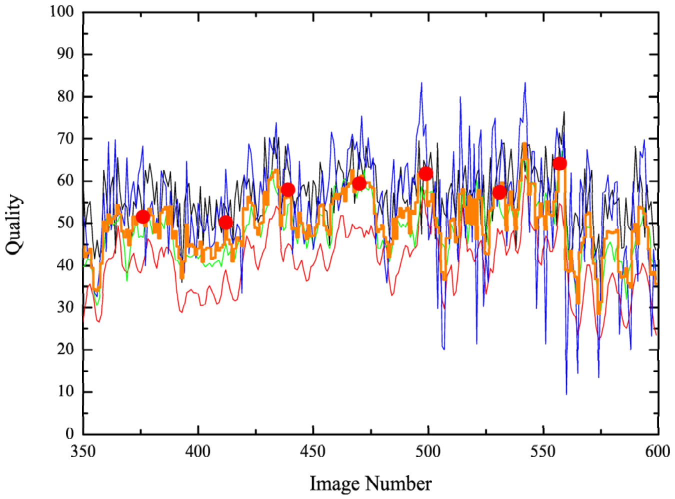

Figure 6.4: Quality factor vs. image number. The quality is evaluated by analyzing the information contents of images power spectrum. Red thin line refers to Fe I line core image; green thin line refers to Fe I Doppler velocity field; blue thin line to Ca II wing image; black thin line to the continuum image. The orange thick line is the mean of the quality factors of these four images. Red dots corresponds to the images selected for the analysis.

with quiet and *magnetic* pixels, it was possible to define an *optimum threshold*, T_{opt}: this was achieved by fitting each IDF with two Gaussian, representing the two pixel populations, and computing T_{opt} minimizing population mixing. Segmented magnetic features, i.e. pixel cluster characterized by Ca II intensity greater than T_{opt}, were used to define Regions of Interest (see left panel of Figure 6.11 for an example) over the Doppler velocity fields and the line core intensity images. Finally, defining the contrast as:

$$C_\lambda = 1 - \frac{I_\lambda}{I_{continuum}} \tag{6.6}$$

they confirmed that magnetic regions correspond to downflows (Domínguez Cerdeña et al., 2003) and to region of reduced contrast in the line core (cfr. Figures 6.6 and 6.7). Moreover, they found a drop of about 30% of the typical downward velocity of such downflows when compared to downflows without magnetic structres.

6.3 3-D Velocity Field

In order to better understand the evolution of supergranules and their bright network counterpart, an extended analysis of the 16^{th} October 2003 observations has been realized, exploiting the full temporal resolution of the dataset.

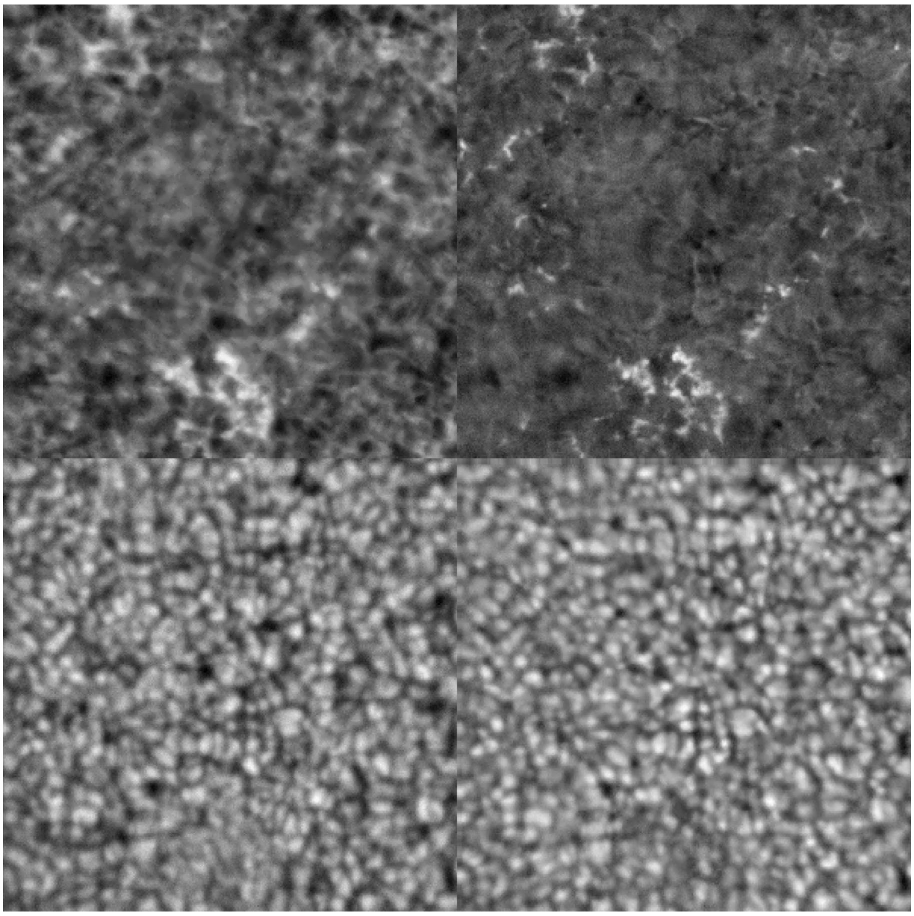

Figure 6.5: A synoptic panel from the 16^{th} October 2003 dataset, corresponding to the first red dot in Figure 6.4. Lower left panel: continuum intensity image. Lower right panel: Doppler velocity field extracted from Fe I 709.0 nm line scan. Upper left panel: Fe I 709.0 nm line core intensity. Upper right panel: Ca II wing intensity image.

In particular, the TST procedure (cfr 5.3) has been applied on the continuum image series and on both the Fe II 722.4 nm and Fe I 709.0 nm Doppler field series, in order to retrieve the horizontal velocity field at different depths of the solar atmosphere. We remember that the major contribution to these Doppler fields comes from the two layers at about 140 km and 70 km above the photospheric surface, respectively for Fe II 722.4 nm and Fe I 709.0 nm lines, as shown by the two RF^I_Vs (cfr. Table 2.1.2 and Figures 2.4 and 2.5).
For each time series the TST produced two horizontal velocity fields, associated to the first and the second 30 minutes of the series. In Figures 6.8, 6.9 and 6.10 the outputs of the TST are presented. The arrows representing the displacement of tracked granules seem to gather on the borders of the supergranule, with the notable exception of the lower border, exactly in correspondence of an extended cluster of bright structures. This seems to suggest that granules on the

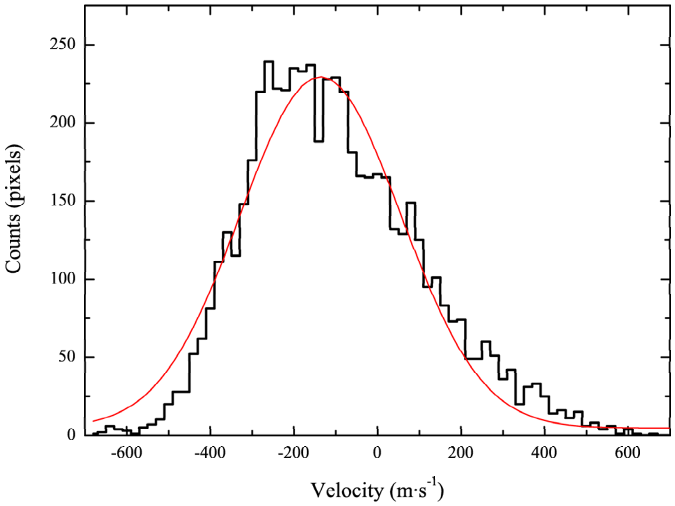

Figure 6.6: Histogram of the Doppler velocity values for the pixel in the *magnetic* region extracted from images of Figure 6.5 (black continuous) and a Gaussian fit to the distribution. The centre of the Gaussian fit is $\simeq\ -250\,m{\cdot}s^{-1}$

edge of the supergranule are in some way different from granules in the centre. In particular, as the TST relies on regular and long lasting structures, granules in the centre of the supergranular cell may be more irregular (a more complex morphology or a faster deformation rate) or with a shorter mean lifetime. This hypothesis is currently under examination.

As already stated, few granular structures have been tracked nearby the bright magnetic cluster in the lower part of the image. While in the tracking of the continuum time series such a lack of tracked structures can be related to the inferior contrast of the region, the same explanation does not hold for the upflows in the Doppler image series.
As a matter of fact, observing the divergence images (right panels of Figures 6.8, 6.9 and 6.10) extracted from the horizontal velocity fields (left panels of Figures 6.8, 6.9 and 6.10), the supergranule is outlined by convergences on $\sim$ 66% of its circumference, while the bright cluster area does not seem to be a region of convergence, despite the fact to be mostly formed of down flows.
Therefore, in order to study the down flows below the bright magnetic cluster, the Doppler and Ca II images were rebinned to a suitable scale, then the pixel forming the cluster were selected on the Ca II images and the mean Doppler velocity of these pixels in each image was computed. The rebinned pixels composing the cluster are shown marked with red crosses in Figure 6.11, superimposed on the average Doppler velocity image and the average Ca II image.
In Figure 6.12 the plot of the mean Doppler velocity (red dashed line) of the cluster pixels against time is reported. Therefore, the average Doppler velocity value of the downflows composing the magnetic cluster is $\simeq\ -100\ m\cdot s^{-1}$ and the estimated volume flow rate of the downflow below the bright cluster is

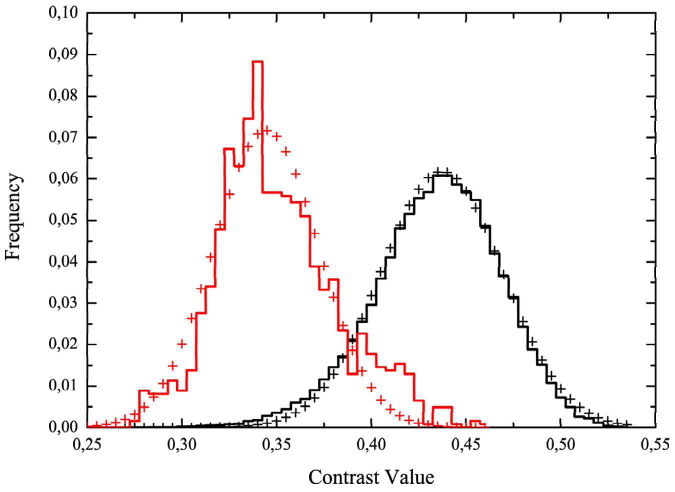

Figure 6.7: Histogram of the contrast value for the quiet sun (black continuous) and the *magnetic* region (red continuous). The crosses represent Gaussian fits to the distributions. The centres of the Gaussian fits are $\simeq$ 0.44 and $\simeq$ 0.34, respectively.

$F_m \sim 8 \cdot 10^{15}\ m^3 \cdot s^{-1}$ over $\sim$ 1 hour. In order to evaluate the significance of these values, a statistical analysis of the distribution of the Doppler mean values on similar clusters has been performed.
In particular, 250 sets of 32 rebinned pixels randomly disposed on an 8×8 sub matrix randomly placed on the image were chosen as reference ensemble, to insure the statistical analysis to be performed on a collection of systems similar to the selected magnetic region. Then the mean $< V >_s$ and the standard deviation $< \delta V >_s$ of the Doppler velocity of such an ensemble were computed for each image (continuous and dotted black lines in Figure 6.12, respectively). The average mean Doppler velocity value (that is the mean velocity value of the ensemble averaged over time) is $<< V >_s>_t\ \simeq 13\ m \cdot s^{-1}$.
As a consequence of this analysis, we can report that the stability and the mass flow of the downflows associated to the bright magnetic cluster in the lower part of the FoV is clearly irreconcilable with a statistical fluctuation and most likely due to a 'magnetic stabilization'.
As this 'magneto-stabilized' region of downflows lasts for the whole duration of the dataset, it can be deduced that, even if velocity fluctuations become feebler in regions of increased magnetic field (cfr. 6.2), the whole region can play an important role in the evolution of the nearby supergranules. Whether or not this region can be organizing the supergranular pattern, as predicted by Rast (2003b), is a question which cannot be addressed by this preliminary analysis.

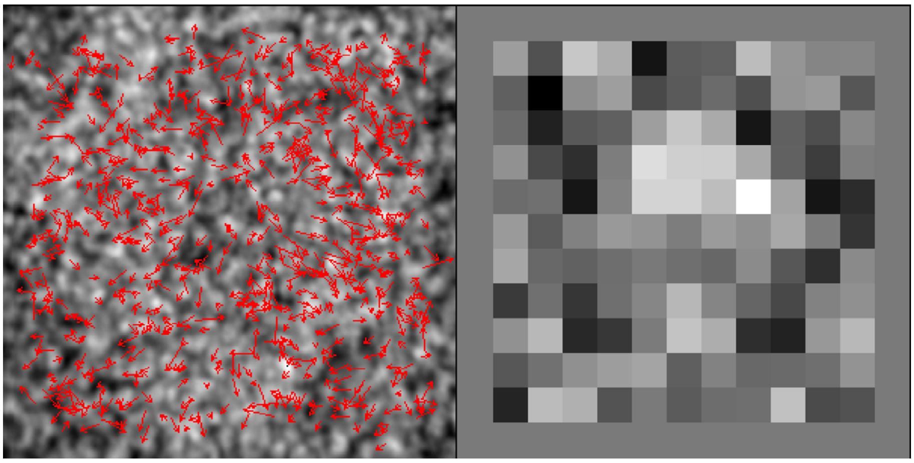

Figure 6.8: Left panel: average continuum image with superimposed the tracked granule displacements represented as red arrows. The granules were tracked by applying the TST to the first half hour of the continuum image time series. Right panel: divergence image obtained from the interpolated horizontal velocity field.

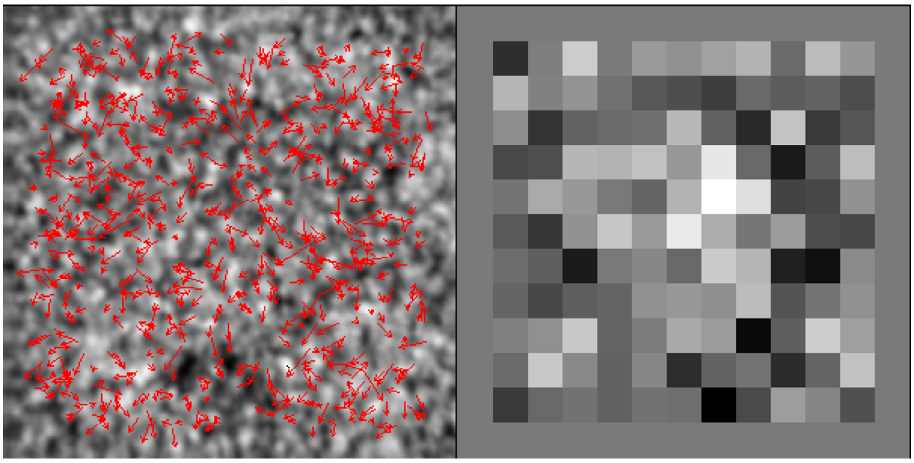

Figure 6.9: Left panel: average Doppler velocity image with superimposed the tracked granule displacements represented as red arrows. The granules were tracked by applying the TST to the first half hour of the Doppler velocity field time series. Right panel: divergence image obtained from the interpolated horizontal velocity field.

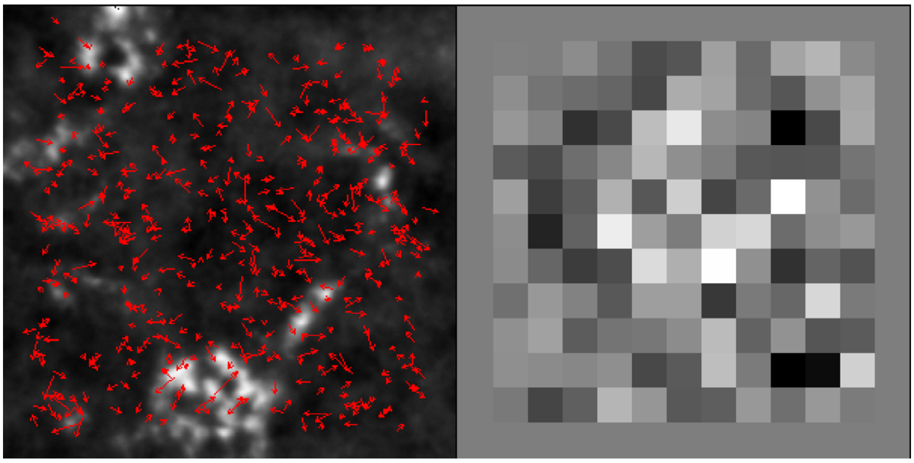

Figure 6.10: Left panel: segmented magnetic regions for the Ca II image in the upper right panel of Figure 6.5 (as described in 6.2) with superimposed the downflows displacements represented as red arrows. The downflows were tracked by applying the TST to the first half hour of the Doppler velocity field time series. Right panel: divergence image obtained from the interpolated horizontal velocity field.

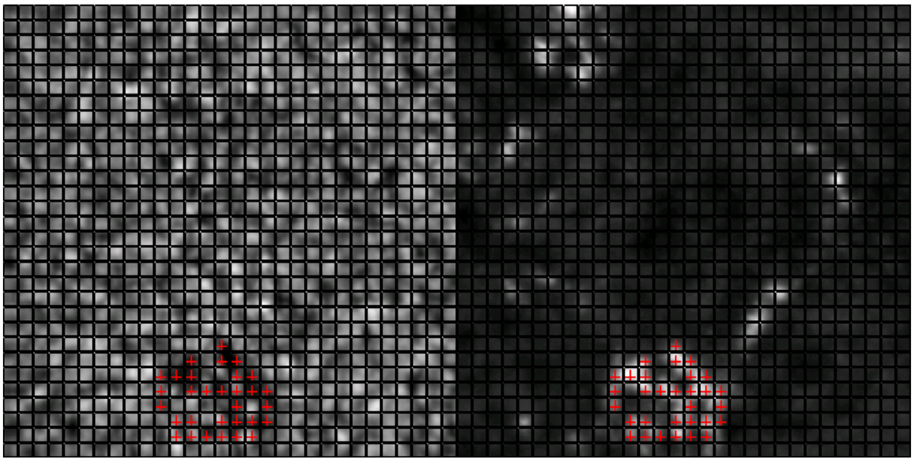

Figure 6.11: Left panel: mean Doppler image averaged over $\sim$ 1 hour. Right panel: mean Ca II image averaged over $\sim$ 1 hour. The rebinned pixels are shown as a superimposed grid and the crosses mark the selected magnetic region.

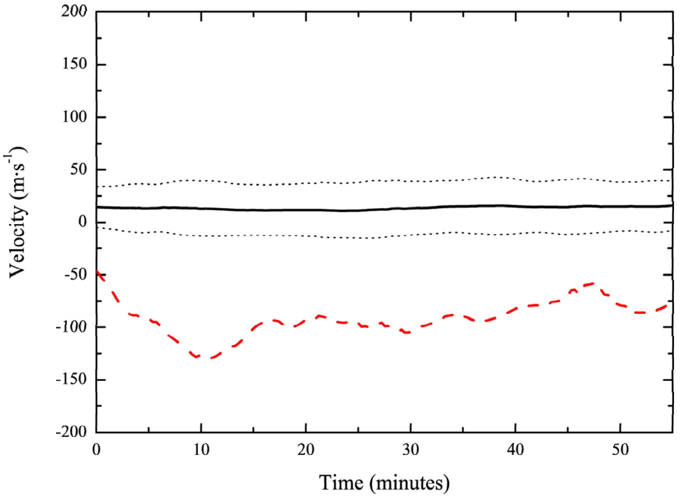

Figure 6.12: Average Doppler velocity in the magnetic pixels vs time (red dashed line), average Doppler velocity in the reference ensemble (black continuous line) and average Doppler velocity ± 1 standard deviation (black dotted lines).

Chapter 7

Convection Topology Describers

This chapter will introduce the reader to the concepts of complexity and organization in patterns and the ways to extract information from pattern viewed as configuration of features via statistical and information theory instruments.

We will start considering the notions of complexity and disorder versus randomness, subsequently we will discuss about pattern organization. In the last part of this chapter we shall consider two approaches for measuring structure organization. First, we will see how information theory provides a measure of the information stored in a system's configurations via the Van Siclen Normalized Entropy. Second, we will examine how it is possible to detect and quantify organization in many-body systems via the Pair Correlation Function.

7.1 Order, Disorder, Complexity

The simplest way to model *order* is through the concept of symmetry, i.e. invariance of a pattern under a group of transformations.

In symmetric patterns one part of the pattern is sufficient to reconstruct the whole. For example, to reconstruct a mirror-symmetric pattern, like the human face, you need to know one half and then simply add its mirror image. The larger the group of symmetry transformations, the smaller the part needed to reconstruct the whole and the more redundant or 'ordered' the pattern. For example, a crystal structure is typically invariant under a discrete group of translations and rotations. A small assembly of connected molecules will be sufficient to describe the whole system: the positions of all other molecules can be generated by applying the different transformations. Empty space is maximally symmetric or ordered: it is invariant under any possible transformation, and any part, however small, can be used to generate any other part. This implies, as we will see later, that a small amount of information is needed to describe the system or, equivalently that the system entropy is small. On the contrary, a disordered system needs a large amount of information to be described and its entropy is high.

It is interesting, however, to note that maximal *disorder* too is characterized by symmetry, not of the actual positions of the components, but of the probabilities that a component will be found at a particular position. For example, a gas is statistically homogeneous: any position is as likely to contain a gas molecule as any other position. The individual molecules will not be evenly spread, but if we look at averages, e.g. the centres of gravity of large assemblies of molecules, the actual spread will again be symmetric or homogeneous, because of the law of large numbers Similarly, a random process, like Brownian motion, can be defined by the fact that all possible transitions or movements are equally probable.

Complexity can then be characterized by lack of symmetry or 'symmetry breaking', by the fact that no part or aspect of a complex entity can provide sufficient information to actually or statistically predict the properties of the others parts.

Natural processes can appear unpredictable to varying degrees and for several reasons.

First, and most obviously, one may not know the 'rules' or equations that govern a particular system. That is, an observer may have only incomplete knowledge of the forces controlling a process. Second, there may be mechanisms intrinsic to a process that amplifies unknown or uncontrolled fluctuations to unpredictable macroscopic behaviour. Manifestations of this sort of randomness include *deterministic chaos.*

Third, if the dynamics are sufficiently complicated it may simply be too computationally difficult to perform the calculations required to go from measurements of the system to a prediction of the system's future behaviour.

Fourth, the measurement process engenders apparent randomness in some way.

A central task is to examine ways to disentangle the different mechanisms responsible for complexity by investigating several of their signatures. This also involves a quantification of the degree of complexity.

We may note that the definition of complexity as midpoint between order and disorder depends on the level of representation: what seems complex in one representation, may seem ordered or disordered in a representation at a different scale. For example, a pattern of cracks in dried mud may seem very complex. When we zoom out, and look at the mud plain as a whole, though, we may see just a flat, homogeneous surface. When we zoom in and look at the different clay particles forming the mud, we see a completely disordered array.

The paradox can be elucidated by noting that scale is just another dimension characterizing space or time (Havel, 1995), and that invariance under geometric transformations, like rotations or translations, can be similarly extended to scale transformations (homotheties).

Havel (1995) calls a system 'scale-thin' if its distinguishable structure extends only over one or a few scales. For example, a perfect geometric form, like a triangle or circle, is scale-thin: if we zoom out, the circle becomes a dot and disappears from view in the surrounding empty space; if we zoom in, the circle similarly disappears from view and only homogeneous space remains.

A typical building seen from the outside has distinguishable structure on 2 or 3 scales: the building as a whole, the windows and doors, and perhaps the individual bricks.

A fractal or self-similar shape, on the other hand, has infinite scale extension: however deeply we zoom in, we will always find the same recurrent structure.

A fractal is invariant under a discrete group of scale transformations, and is as such orderly or symmetric on the scale dimension. The fractal is somewhat more complex than the triangle, in the same sense that a crystal is more complex than a single molecule: both consist of a multiplicity of parts or levels, but these parts are completely similar.

7.1.1 Pattern organization

Due to the inborn capacity of the human visual system to recognize patterns, images are immediately understandable or not, based on the ease by which their message can be processed by our intellect.

This depends on both content (information) and relationships (organization).

Usually, a pattern is easily recognizable if it is mathematically simple, and not so if it is random.

In nature, pattern formation occurs when different types of processes interact to destroy the spatial coherence of the system.

Spatio-temporal patterns appear spontaneously in a wide range of physical, chemical, and biological systems when those systems are driven sufficiently far from thermodynamic equilibrium. Order often arises spontaneously from disorder; patterns can emerge through a process of self-organization.

The classic example is Rayleigh-Bènard convection in a fluid layer heated from below. For sufficiently strong heating fluid motion sets in, typically in the form of convective rolls. As the driving parameter is increased, regular patterns are supplanted by patterns that are more and more irregular in space and time, resulting in states that are intermediate between ordered patterns and turbulence.

Early pattern formation research focused on relatively simple spatially periodic structures, e.g. convective rolls or hexagonal structures. Research challenges include giving precise characterizations of such states, identifying the relevant mechanisms for their creation, and being able to control their evolution.

Fundamental to pattern formation research is the observation that they are determined by cooperative interactions on large scales and hence many aspects of the phenomena can be understood on a 'macroscopic level'. It is therefore necessary to develop instruments able to analyze pattern topology and morphology in order to derive the symmetries of the problem and the important physical parameters.

7.2 The Measurement of Information Quantities

In the late 1940's Claude Shannon founded the field of communication theory (Shannon and Weaver, 1949), motivated in part by his work in cryptography during World War II. His attempt to analyze the basic trade-off in encoding information in ways that still allowed recovery by the receiver, led to a study of how signals could be compressed and transmitted efficiently and error free. His basic conception was that of a *communication channel* consisting of an *information source* which produces *messages* that are encoded and passed through a channel. A *receiver* then decodes the channel's output in order to recover the original messages.

Central in this analysis was the definition of the source's rate of information production, called the source entropy *rate*, and the maximum carrying capacity called the *channel capacity*, of the channel. Shannon's main assumption was that an information source was described by a distribution over its possible messages and that, in particular, a message was 'informative' according to how unlikely its occurrence was. The unlikeness of a message, averaged over the source's messages, is the source entropy rate. Therefore, the Shannon Entropy of a system is related to the amount of information it contains.
A highly ordered system can be described using fewer bits of information than a disordered one. For example, a string containing one million '0's can be concisely described using proper encoding, while a string of random symbols will be impossible to compress.
In practice, if the sending device is equally likely to send any one of a set of N messages, then the preferred measure of '*the information produced when one message is chosen from the set*' is the logarithm of N, because the ratio between a series of instances and the series of their probability is equal to the ratio of an arithmetic progression to a geometric one.
In one of his papers, Shannon stated (1948):

> The choice of a logarithmic base corresponds to the choice of a unit for measuring information. If the base 2 is used the resulting units may be called binary digits, or more briefly bits, a word suggested by J. W. Tukey. A device with two stable positions, such as a relay or a flip-flop circuit, can store one bit of information. N such devices can store N bits...

Shannon's formula gives the entropy $H(M)$ of a message M in bits:

$$H(M) = -\log_2 [p(M)] \tag{7.1}$$

Where $p(M)$ is the probability of message M. The functional form of Shannon Entropy was already been applied by Boltzmann (1872, 1877, 1896, 1897) as a measure of disorder of thermodynamics systems.

The investigation and the characterization of the solar granulation pattern may benefit by statistical-mathematical methods introduced in different physical frameworks. In detail, in the field of matter physics it was clearly shown that the study of the topology and the evolution of correlated random structures may take advantage of the application of Shannon's information theory (Shannon, 1948; Shannon and Weaver, 1949; Beck and Schlogl, 1993).
For example, (Andraud et al., 1994; Andraud et al., 1997) introduced an entropic measure, named *configuration entropy*, as a descriptor of random morphologies. Such configuration entropy is a measure of the local fluctuations of some measurable quantity over the random system, defined as follows.
Let us consider a $L\times L$ binarized (black and white) image of some physical observable quantity, and a square sliding cell of side length l containing $a = l^2$ pixels. If $N_k(a)$ is the number of cells of size a containing k black pixels, and N is the total number of sliding cells, then we can define a set of relative frequencies

$p_k(a)$, as estimates for probabilities, according to the following expression:

$$p_k(a) = \frac{N_k(a)}{N} \tag{7.2}$$

Henceforth, the configuration entropy $H^*(a)$ will follow according to the definition:

$$H^*(a) = -\frac{1}{\log(1+a)} \sum_{k=0}^{a} p_k(a) \log p_k(a) \tag{7.3}$$

Such a definition is equivalent to the usual Gibbs-Shannon entropy (as in Eq. 7.1) normalized by the factor *log(a + 1)*, which plays a role similar to the 'multiplicative renormalization in the theory of critical phenomena' (Andraud et al., 1997).

When applied to a disordered system, this entropic measure is able to extract some useful information dealing with the typical length scale at which inhomogeneities are present and so on.

A more sensitive measure of the morphological complexity in random system was introduced by van Siclen (1997). This measure was called *information entropy* $H(l)$ because of its ability to extract the average information content at a certain length scale l. Moreover, this measure is able to keep information on clustering effects, as well as on periodicity or ordering.

7.3 The Van Siclen's Information Entropy: $H'(m)$

According to the information theory (cfr. 7.2), the information content of a system in a configuration i is directly proportional to *-log*(p_i), where p_i is the a priori probability of finding the system in the i^{th} configuration. When the information content is averaged over all the possible choices it defines the information entropy H.

Moreover, to make such a measure more sensitive to the structures at the different scale Van Siclen introduced the normalized information entropy measure $H' = H - H_r$, where H_r is the expected information entropy for a completely random system and H is the actual information entropy.

Let us briefly resume how to evaluate such a quantity. Consider a two-level image consisting of a collection of N black pixels placed on a square grid of side length L, and a $m \times m$ box. Let it be p_i the probability of finding exactly i black pixels of the N in a $m \times m$ box if the black pixels were perfectly distributed in the random fashion. Then,

$$p_i(m) = \begin{pmatrix} m^2 \\ i \end{pmatrix} \begin{pmatrix} L^2 - m^2 \\ N - i \end{pmatrix} \begin{pmatrix} L^2 \\ N \end{pmatrix}^{-1} \tag{7.4}$$

where i ranges from the greater between 0 and $m^2 - L^2 + N$ to the lesser between N and m^2. From here it follows that the reference information entropy of a finite, perfectly random, system is

$$H^{rnd}(m) = -\sum_i p_i(m) \log(p_i(m)) \tag{7.5}$$

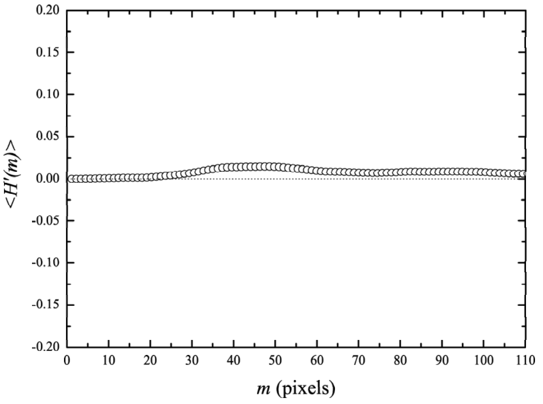

Figure 7.1: $< H'(m) >$ for a pseudo-random distribution of approx. 4000 black pixels. $< H' >$ has been averaged over an ensemble of 100 different pattern realizations.

On the other hand, the information entropy H(m) for the actual configuration is

$$H(m) = -\sum_i P_i(m) \log(p_i(m)) \tag{7.6}$$

where $P_i(m)$ is the actual probability of finding i black pixels in any $m \times m$ box, and $p_i(m)$ is defined according to Eq. 7.4.
Therefore, the normalized information entropy will be

$$H'(m) = H(m) - H^{rnd}(m) = -\sum_i (P_i(m) - p_i(m)) \log(p_i(m)) \tag{7.7}$$

On the basis of the definition of $H'(m)$ we should expect that for a completely random distribution of a collection of N black pixels *H'(m) = 0* at each length scale m. In Fig. 7.1 we report the behaviour of $< H' >$ averaged on an ensemble of several 200×200 two-level images containing approx. 4000 black pixels pseudo-randomly distributed. As expected $< H'(m) >$ is very close to zero over the entire analyzed range of scales. The slight deviations from zero should be read as the effect of a sporadic random aggregation of some black pixels, as well as from finite size effects. We remark that the range of scales investigated has been limited to half of the linear size of the images (m $\leq$ 100) to avoid the artifacts of this analysis at larger scales due to the decreasing box statistics (van Siclen, 1997). It is also worth noting that the investigation of maxima positions can provide information on the existence of a nearly-ordered hidden lattice structure, but it can reveal nothing about the real geometry of the hidden ordering.
The main difference between the more usual techniques based on Fourier and/or wavelet transforms and the normalized information entropy is that the H' analysis, being based on a probability measure, does not require any preliminary choice of an ad-hoc set of functions or waveforms (sine-cosine waves, plane waves, wavelets, etc.) in order to decompose the field/image under investigation.

Moreover, because the Fourier spectrum is related to the autocorrelation function over the field, in order to observe strong signatures of periodicity using these techniques, structures should be all of the same type (i.e. have the same shape), all oriented in the same direction, and all located in the same position inside any elementary cell.

When these conditions are not fulfilled, spurious results may be found in terms of broad-band spectra (i.e. peaks may be indiscernible).On the other hand, although wavelet analysis has a greater capability in finding localized isolated structures and in extracting characteristic scales, when the results are discussed in terms of spectra, this technique does not differ substantially from the Fourier transform (Lawrence et al., 2001; Starck et al., 1998).

Conversely, the normalized information entropy H' analysis, looking for regularities using a probabilistic approach, is less affected by the aforementioned aspects. In other words, while Fourier analysis looks for periodicity in the field and wavelet analysis looks for characteristic scales, the normalized information entropy H' analysis is able to extract information on the presence of statistical regularities in the mutual positions of the structures.

7.3.1 The Normalized Hexagonal Information Entropy: $H'_{hex}(r)$

In order to achieve a more isotropic analysis of the spatial ordering properties of a physical system, the $H'(m)$ can be improved by sampling the system by a matrix with an hexagonal outline.

To define the new entropy measure, we have to redefine a lattice sampling from square to hexagonal. This is accomplished by superimposing an hexagonal grid over the original square matrix and defining how old square pixel value would contribute to new hexagonal pixel values. As we are interested only in the transformation of binarized images, the rule would be particularly simple: one hexagonal pixel would be set at 0 (black pixel) if more than half of its area is covered by square pixel with 0 value, it would be set at 1 (white) otherwise. For the sake of simplicity, one of the two generating vectors of the square lattice can be chosen parallel to one of the two generating vectors of the square lattice. Moreover, the side of an hexagonal pixel has been chosen equal to half the side of the original pixels. The form of the hexagonal sliding matrix, i.e. the new box that substitutes the square $m \times m$ box in the $H'(m)$ measure, must be properly defined as its dimension defines the scales in the new measures. Although it is not possible to employ hexagons of growing size, it is possible to use rosettes of growing dimensions. The area of a rosette is $3m_h(m_h - 1)$, where m_h is the side of the rosette in hexagons. Therefore, the hexagonal sampled image is limited by the largest rosette one can define in the square image. The area of the hexagonal sampled image in hexagonal pixels would be $\frac{3}{4}L^2 + \frac{1}{4}$, where L is the horizontal dimension of the hexagonal image expressed in hexagonal pixels. Taking into account these substitutions, we modify 7.5 into:

$$H^{rnd}_{hex}(m) = -\sum_i p_i(m_h)\log(p_i(m_h)) \tag{7.8}$$

where $p_i(m_h)$ is the probability to find i objects in an hexagonal rosette of side m_h for a random system containing N objects. That is:

$$p_i(m_h) = \begin{pmatrix} m^2_{hex} \\ i \end{pmatrix} \begin{pmatrix} L^2_{hex} - m^2_{hex} \\ N - i \end{pmatrix} \begin{pmatrix} L^2_{hex} \\ N \end{pmatrix}^{-1} \tag{7.9}$$

where

$$m_{hex}^2 = 3m_h(m_h - 1) + 1 \tag{7.10}$$

and

$$L_{hex}^2 = \frac{3}{4}L^2 + \frac{1}{4} \tag{7.11}$$

and i ranges from the greater between 0 and $N - \frac{3}{4}L^2 - \frac{1}{4} + 3m_h(m_h - 1) + 1$ to the lesser between N and $3m_h(m_h - 1) + 1$. The definition of $P_i(m_h)$ maintains the meaning of frequency of hexagonal pixels belonging to a feature (white pixels) inside the hexagonal sliding matrix. Therefore, the formula to compute the hexagonal normalized information entropy is:

$$H'_{hex}(m_h) = H_{hex}(m_h) - H_{hex}^{rnd}(m_h) = -\sum_i (P_i(m_h) - p_i(m_h))\log(p_i(m_h)) \tag{7.12}$$

that is formally equivalent to 7.7.

In order to compare the results obtained by both the square and the hexagonal H', it is suitable defining a common reference spatial scale as the radius of a circle having the same area of the used sliding matrices. That is, $r = m/\sqrt{\pi}$ for square boxes, where m is the side of the box in square pixels; and $r = \sqrt{\frac{3(3m_h(m_h-1)+1)}{\pi}}$ for hexagonal rosettes, where m_h is the side of the rosette in hexagonal pixels.

In full analogy with the $H'(r)$, $H'_{hex}(r)$ is positive for r where structure clustering is greater than that occurring for a random distribution and $H'_{hex}(r)$ is negative for r where structure clustering is more ordered than a random distribution.

7.4 Applying $H'_{hex}(r)$ to a Granulation Dataset

We present here some results obtained by analyzing a broadband granulation timeseries acquired at Sacramento Peak, by means of hexagonal $H'(m)$. This image sequence (hereafter NSO96) was acquired at the NSO Dunn Solar Telescope (Sacramento Peak, Sunspot, New Mexico) on October 16, 1996 (from 14:30 UT to 16:30 UT). This broadband (central wavelength 550.0 nm, bandpass 5 nm) sequence is made of 512 images with field of view of 31.5" × 31.5", $(256 \times 256$ pixels), each taken with an exposure time of 0.008 s. After the standard corrections, this series was treated with a destretching algorithm and the acoustic modes pattern was removed by $k_h - \omega$ filtering with a cut-off velocity of 4.7 $km \cdot s^{-1}$.

For a more detailed description of this dataset refer to Cauzzi et al. (1998).

This dataset has been analized by the TST procedure (cfr. 5.2.2) and the histogram of the granule lifetimes is reported in Figure 7.2. By applying a single exponential fit, taking into account only granules lasting more than 2.5 minutes, we can estimate the mean lifetime of the longest lived granules. Such exponential fit retrieved $\tau_l \simeq 3\ min$.

In order to investigate the time evolution of persistent sites, time-integrated images have been analyzed by $H'_{hex}(r)$.

Such time-integrated images are obtained by summing up single binarized images, obtained by applying a dynamical threshold (cfr. 5.2.1: Eq. 5.2), in

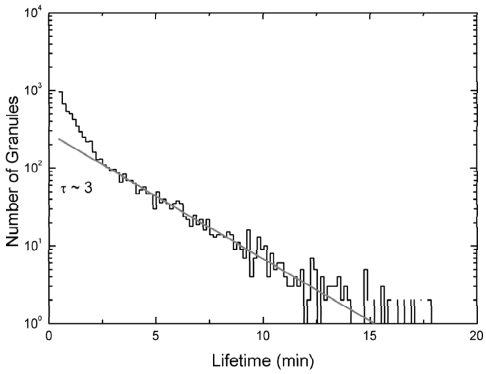

Figure 7.2: Granule lifetimes histogram with superimposed exponential decay fit for $t \geq 2.5$ *min.*

different temporal sliding windows, corresponding to 5, 10, 15, 20 and 25 minutes. We therefore obtained 5 image sequences with 5, 10, 15, 20 and 25 minutes integration times, where pixel values indicate how often that pixel belonged to a granule. As we summed up binarized images, we avoided assigning a larger statistical weight to brighter objects during the time-integration operation (Rast, 2002).

To define a persistent structure in the time-integrated image sequences we used a threshold equal to $\frac{3}{4}N_{imm}$, where N_{imm} is the number of images used in the time window of the integration process, therefore the thresholds are 3.75, 7.5, 11.25, 15 and 18.75 minutes, respectively. Accordingly, a structure is defined 'persistent on time-scale T' if that structure is present on the same position for at least 75% of the time T.

This approach can also be applied to the original binarized dataset, where, of course, each binarized structure present on an image is 'persitent on time-scale 0 *minutes*'.

The $H'_{hex}(r)$ has been computed for each image of each sequence, and, for each sequence, a mean $< H'_{hex}(r) >$ has been obtained. Consequently, these $< H'_{hex}(r) >$, reported in Figure 7.3, refer to different integration times.

The $< H'_{hex}(r) >$ obtained averaging the $H_{hex}(r)$ of single binarized images shows a strong clustering scale at $r_1 \simeq 1\,Mm$. This scale obviously corresponds to the average granular scale. With increasing integration time, this scale seem to fade away and a larger clustering scale seems to rise at $r_8 \simeq 8\,Mm$, for times longer than 20 minutes, also this scale disappears. In Figure 7.4 the temporal evolution of $< H'_{hex}(r_8) > / < H'_{hex}(r_1) >$, i.e. the ratio between the $< H'_{hex} >$ associated to the 8 Mm and 1 Mm scales, is reported. From an exponential fit to this plot we retrieved $\tau_{gw} = 9.8 \pm 0.8\,min$, i.e., the typical grow time of the contribution of $H'_{hex}(r_8)$ to the whole $H'_{hex}(r)$ signal. Moreover, the $< H'_{hex}(r_8) > / < H'_{hex}(r_1) >$ behaviour indicates that the maximum efficiency in persistent sites clustering is reached at $\sim 6\,min$, i.e. at about $2 \cdot \tau_l$, the granular scale is no more contributing significantly to the $H'_{hex}(r)$ signal.

There is good consistency between this characteristic time and the time scale as-

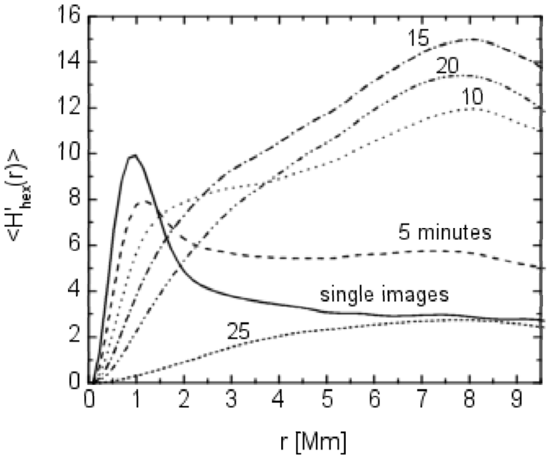

Figure 7.3: The $< H'_{hex}(r) >$ for integration times from 0 (single images) to 25 minutes.

sociated to exploding granule processes (Hirzberger et al., 1999a; Berrilli et al., 2002).

7.5 The Pair Correlation Function: $g_2(r)$

In order to investigate the possible topological order (Ziman, 1979) of the structures present in the images a statistical approach can be applied. We choose to use a spatial point pattern analysis method, the *Pair Correlation Function* $g_2(r)$, which is the probability of finding a structure at distance r, conditional on there being a structure at the origin.

A general correlation function can be defined in terms of the probability distribution function $P^{(N)}$ of a distribution of N particles, according to:

$$g_{(n)}(\vec{r}_1, ..., \vec{r}_n) = \frac{1}{\rho^n}\rho^{(n)}(\vec{r}_1, ..., \vec{r}_n) = \frac{V^n N!}{N^n(N-n)!}\int d\vec{r}_{n+1}...d\vec{r}_N P^{(N)}(\vec{r}_1, ..., \vec{r}_N) \tag{7.13}$$

where $P^{(N)}(\vec{r}_1, ..., \vec{r}_N)d\vec{r}_1...d\vec{r}_N$ represents the probability that particle 1 will be found in a volume element $d\vec{r}_1$ at the point r_1 , particle 2 will be found in a volume element $d\vec{r}_2$ at the point r_2 ,..., particle N will be found in a volume element $d\vec{r}_N$ at the point r_N.
and $\rho^{(n)}(\vec{r}_1, ..., \vec{r}_n)d\vec{r}_1...d\vec{r}_n$ is the probability that *any* particle will be found in the volume element $d\vec{r}_1$ at the point r_1 and *any* particle will be found in the volume element $d\vec{r}_2$ at the point r_2 ,..., *any* particle will be found in the volume element $d\vec{r}_N$ at the point r_N, since the first particle can be chosen in N ways, the second chosen in N-1 ways...

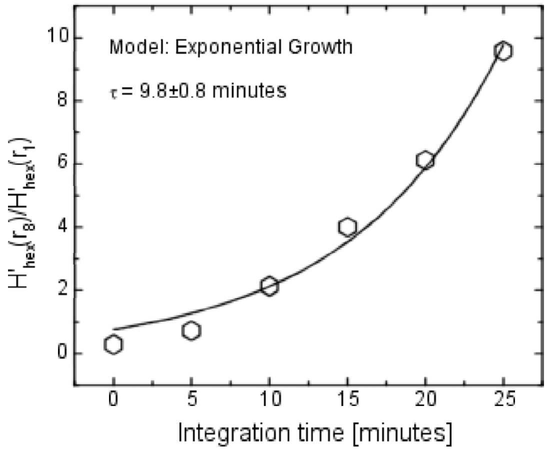

Figure 7.4: The ratio $< H'_{hex}(r_8) > / < H'_{hex}(r_1) >$ between the hexagonal normalized information entropies associated to 8 Mm and 1 Mm, respectively and superimposed exponential growth fit ($\tau_{gw} = 9.8 \ \pm \ 0.8 \ min$).

Another useful way to write the correlation function is

$$g_{(n)}(\vec{r}_1, ..., \vec{r}_n) = \frac{V^n N!}{N^n (N-n)!} \int d\vec{r}'_1 ... d\vec{r}'_N P^{(N)}(\vec{r}'_1, ..., \vec{r}'_N) \delta(\vec{r}_1 - \vec{r}'_1) ... \delta(\vec{r}_n - \vec{r}'_n) = \tag{7.14}$$

$$= \frac{V^n N!}{N^n (N-n)!} \langle \prod_{i=1}^{n} \delta(\vec{r}_i - \vec{r}'_i) \rangle_{\vec{r}'_1, ..., \vec{r}'_N} \tag{7.15}$$

i.e., the general n-particle correlation function can be expressed as an ensemble average of the product of δ-functions, with the integration being taken over the variables $\vec{r}'_1, ..., \vec{r}'_n$.

Of particular importance is the case $n = 2$, or the correlation function $g_2(\vec{r}_1, \vec{r}_2)$ known as the *Pair Correlation Function.* The explicit expression for $g_2(\vec{r}_1, \vec{r}_2)$ is

$$g_2(\vec{r}_1, \vec{r}_2) = \frac{V^2 N!}{N^2 (N-2)!} \langle \delta(\vec{r}_1 - \vec{r}'_1) \delta(\vec{r}_2 - \vec{r}'_2) \rangle = \tag{7.16}$$

$$= \frac{N(N-1)}{\rho^2} \langle \delta(\vec{r}_1 - \vec{r}'_1) \delta(\vec{r}_2 - \vec{r}'_2) \rangle_{\vec{r}'_1, ..., \vec{r}'_N} \tag{7.17}$$

In general, for homogeneous systems, there are no special points in space, so that g_2 should depend only on the relative position of the particles or the difference $\vec{r}_1 - \vec{r}_2$. In this case, it proves useful to introduce the change of variables

$$\vec{r} = \vec{r}_1 - \vec{r}_2 \tag{7.18}$$

$$\vec{R} = \frac{\vec{r}_1 + \vec{r}_2}{2} \tag{7.19}$$

Then, we obtain a new function g_2, a function of $\vec{r}$ and $\vec{R}$:

$$g_2(\vec{r},\vec{R}) = \frac{N(N-1)}{\rho^2}\langle\delta(\vec{R}+\frac{1}{2}\vec{r}-\vec{r}_1')\delta(\vec{R}-\frac{1}{2}\vec{r}-\vec{r}_2')\rangle_{\vec{r}_1',\ldots,\vec{r}_N'} \tag{7.20}$$

In general, we are only interested in the dependence on $\vec{r}$. Thus, we integrate this expression over $\vec{R}$ and obtain a new correlation function defined by

$$g_2(\vec{r}) = \frac{1}{V}\int d\vec{R}g_2(\vec{r},\vec{R}) \tag{7.21}$$

For an isotropic system such as a liquid or gas, where there is no preferred direction in space, only $r = |\vec{r}|$ is of relevance. Thus, as we seek a choice of coordinates that involves r explicitly, the spherical-polar coordinates are the most natural choice.
In the bidimensional polar coordinates

$$\vec{r} = r\vec{n} \tag{7.22}$$

where

$$\vec{n} = (sin\theta, cos\theta) \tag{7.23}$$

where θ is the polar angle. Thus, the *Pair Correlation Function* that depends only on the distance r between two particles is defined to be:

$$g_2(r) = \frac{1}{2\pi}\int g_2(\vec{r})d\theta \tag{7.24}$$

and, integrating $g_2(r)$ over the radial dependence, one finds that:

$$2\pi\rho\int g_2(r)dr = N-1 \simeq N \tag{7.25}$$

For the photospheric fields we are investigating, it is convenient to interpret $g_2(r)$ as the probability of finding a target structure, identified by its barycentre, within an annulus of radius r and thickness dr from a chosen starting structure, also identified by its barycentre. The total number of structures in the annulus is $N(r)$:

$$N(r)dr = 2\pi r\rho_{st}g_2(r)dr \tag{7.26}$$

where ρ_{st} is structure number density. Therefore, the $g_2(r)$ can be easily calculated as

$$g_2(r) = \frac{1}{N(r)}\sum_{i\neq j}\delta(r-r_{ij}) \tag{7.27}$$

where the summation is performed over all the structures present in the annulus of area $2\pi rdr$, but only once for each pair. If the system we are investigating is completely disordered, we would expect to find the same number density of structures at any distance r. Therefore, we expect $g_2(r)$ to be constant. If we apply a normalization procedure to the function, taking into account the probability function for a full random distribution, the constant equals unity.

On the contrary, $g_2(r)$ will show a multi-peak behaviour if we consider an ensemble of completely ordered structures. Starting from an initial structure we will find no other structure in the immediate vicinity. So $g_2(r)$ will start from zero at $r = 0$ and, as soon as r approaches the nearest neighbour structure at distance r_1, a peak will occur. The second peak in the $g_2(r)$ will correspond to the most probable location for the next-nearest neighbours and so on. The relative positions of these peaks depend on the topological ordering of the structures. If the system is not a perfect lattice, i.e., there are dislocations or it is the result of a simple packing procedure, the order is present only at small spatial scales and the amplitudes of this oscillation dampen as r increases. Hence, the position and height of the $g_2(r)$ peaks provide information on the topological order of the system. Particularly, the positions correspond to spatial regularity, while the amplitude damping is linked to local disorder. Thus, the deviation from unity of $g_2(r)$, normalized with respect to the random distribution, provides a measure of the degree of spatial correlation between structures.

7.5.1 $g_2(r)$ analysis template

In our implementation of the $g_2(r)$ algorithm, the pair distances are computed using the location of structures barycentres derived from the application of the first part of the Two-level Structure Tracking (TST) procedure (Del Moro, 2004) to the images. The $g_2(r)$ is calculated for each structure in the central region of the image, normalized to the random distribution with the same numerical density and then averaged over all the utilized structures.

The computed $g_2(r)$ functions are analyzed into the physical framework of a *hard sphere random close packing* model. This kind of packing has been recently investigated by Torquato and Stillinger (2002). The authors explored a family of $g_2(r)$ models describing random packing of hard spheres of the same size, that incorporates the known features of core exclusion, contact pairs, and dampened oscillatory short-range order beyond contact. Since our structures have a size distribution, we choose to relax the condition (i) of Torquato and Stillinger (2002), where $g_2(r)$ is assumed to be equal zero for $r < R_{sphere}$. Consequently we found it suitable to fit the $g_2(r)$ with the dampened cosine function,

$$y(r) = Ae^{-(r/\lambda_0)}cos(2\pi r/P_0) + K \tag{7.28}$$

to derive the characteristic scales at which long-range order is suppressed (λ_0) and short-range order is controlled (P_0). It is worth noting that the dampened cosine fit assumes a statistically homogeneous and isotropic field.

7.6 Applying $g_2(r)$ to Granulation and Supergranulation Datasets

We present here some results obtained by applying TST to a flow-map series extracted by helioseismology from MDI data and to a broadband granulation time series acquired at Tenerife. The divergence signal maps used in this analysis are described in 4.3.2 and in paragraph 2 of Duvall and Gizon (2000).

The granulation image sequence (hereafter THEMIS99) has been acquired at the THEMIS telescope (Observatorio del Teide, Tenerife, Spain) in IPM observing mode on 1 July 1999. It was originally made up of 608 broad-band (central wavelength 538.0 nm, band-pass 4 nm) 30" × 30" images with 0.04 s exposure time and 0.13" pixel scale. After the standard correction, the acoustic mode patterns were removed by a $k_h - \omega$ filter, with a cut-off velocity of 6 $km \cdot s^{-1}$, and a Wiener filter was applied to the images. A more detailed description of observations and data reduction procedures can be found in Berrilli et al. (2002).

In order to directly compare the $g_2(r)$ functions extracted from the granulation and supergranulation timeseries, the two datasets should have

(a) the same spatial sampling;

(b) a similar number of structures in the FoV;

(c) a similar time length and sampling of the series with respect to typical lifetime of the structures.

Point (a) is already accomplished, as segmented structures in both datasets have about the same number of pixels. Points (b) and (c) may be accomplished by reducing the FoV of the THEMIS99 series in order to have an equal mean number of granular and supergranular structures in analyzed images, and diluting the time resolution of THEMIS99 series in order to obtain the required time sampling. We compared the spatial and temporal scales of granulation and supergranulation and suitably rescaled the granulation dataset. For this purpose we used as 'typical' cell size of 1 Mm and 30 Mm, respectively, and as 'typical' lifetime 4 min and 22 hr, respectively. We want to stress that the values used for the granulation and supergranular cell sizes and lifetimes are derived using the same TST algorithm (cfr. 5.3). In practice, we condensed the THEMIS99 data to a 12 image (90 s spaced) time-series with a central sub-field of 28.5" × 28.5". To investigate the possible topological order in granular and supergranular structures, we analyzed the $g_2(r)$ properties obtained both from single images, which form the two dataset, and from the time-averaged images. In order to probe the existence of dislocation order in the persistent patterns, we studied the image obtained by time averaging the MDI series and the reduced THEMIS series. To emphasize persistent structures and reduce confusion from bright, but short-lived features, the averaging procedure is accomplished by summing up binarized images, i.e., images without intensity information. In fact, in the binarized images, pixels belonging to structure are set to 1 and all the other pixels are set to 0. As in 7.4, the binarization has been achieved by applying a dynamical threshold (cfr. 5.2.1: Eq. 5.2). The computed time-averaged image for the MDI and THEMIS datasets are shown in Figures 7.5 and 7.6, respectively.

We applied to the MDI average image a threshold to extract structures that were present in the series for more than 64 hours, i.e., pixels whose value is greater than 8. We choose this threshold to select recurrent sites, as the probability of a single supergranule to survive for 64 hours is only $\sim 5\%$ (Del Moro (2004) and cfr. 5.3.2). As the 147 permanent structures in the time-averaged image are significantly more than 5% of the structures in the single images (about 400), we infer that most are due to the recurrence of distinct supergranules in the same site.

Applying the same scheme, the THEMIS average image has been thresholded with the same value in order to extract structures that were present in the series for more than 12 minutes.

On all the images the $g_2(r)$ has been computed according to the procedure described in the previous section. Moreover, in order to enhance the statistic significance of the histogram we found it appropriate to use 10 Mm sliding bins, spaced by 1 Mm, achieving a running mean of the $g_2(r)$ signal.

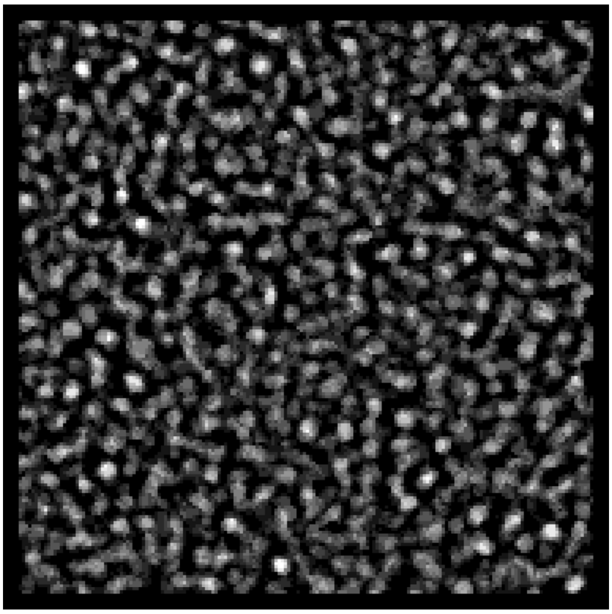

Figure 7.5: The pattern of persistent supergranular structures obtained by time-averaging the SOHO-MDI helioseismology dataset.

7.6.1 Applying $g_2(r)$ to Supergranulation dataset

To investigate the topological order in the single divergence maps, we produced a $< g_2(r) >$ by averaging the $g_2(r)$ functions extracted from the individual maps which form the timeseries. The resulting $< g_2(r) >$ function, shown in Figure 7.7, presents five well-defined peaks. From the application of the dampened cosine fit (cfr. 7.5.1) we obtained $P_0 = 28.7 \pm 0.6\ Mm$ and $\lambda_0 = 23 \pm 3\ Mm$, the reduced χ^2 is obtained directly from the fit procedure and is equal to $\chi^2_R = 0.002$.

When the $g_2(r)$ analysis is applied to the time-averaged image, we obtain the signal reported in Figure 7.8. The fitting of the $g_2(r)$ with the dampened cosine retrieved $P_0 = 26.5 \pm 0.4\ Mm$ and $\lambda_0 = 24 \pm 2\ Mm$ ($\chi^2_R = 0.025$). This non-trivial behaviour disagrees with a Gaussian field of structure and supports our suggestion of a topological order resembling that of a hard sphere random close packing.

Moreover, a closer look at Figures 7.7 and 7.8 shows that the fits, while properly matching the first peaks, fail to correspond to the rest of the histograms. We believe this ensues from the two assumptions, implicit in the dampened cosine fit, of statistical homogeneity and isotropy of the field. This implies that minor residual distortions due, for example, to the projection of the solar sphere over

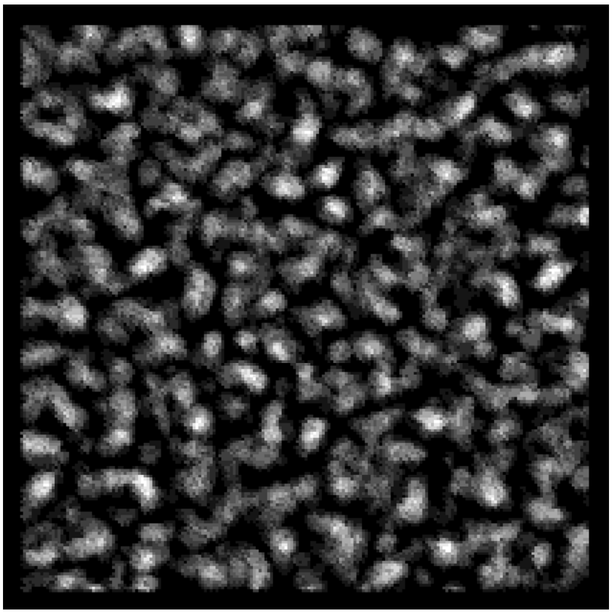

Figure 7.6: The pattern of persistent granular structures obtained by time-averaging the THEMIS99 dataset.

the plane, would slightly alter the distances between the structures, with the consequence of making the fit less accurate in the periphery of the map.

7.6.2 Applying $g_2(r)$ to Granulation dataset

In analogy to the $g_2(r)$ analysis we performed for the MDI time series, we investigate the order topology of both instantaneous and persistent granulation patterns using the reduced THEMIS99 time series.
In Figure 7.9 we report the $< g_2(r) >$ signal computed from 12 single granulation images. The dampened cosine fit procedure applied to this $< g_2(r) >$ signal, produced $P_0 = 1.20 \pm 0.01\ Mm$ and $\lambda_0 = 0.19 \pm 0.02\ Mm$ ($\chi^2_R = 0.005$).
In Figure 7.10 we report the $g_2(r)$ function obtained by applying the $g_2(r)$ algorithm to the time averaged granulation field. The dampened cosine fit to this function retrieved $P_0 = 1.20 \pm 0.02\ Mm$ and $\lambda_0 = 0.4 \pm 0.1\ Mm$ ($\chi^2_R = 0.06$).
A close look at Figure 7.10 reveals that the $g_2(r)$ of the granulation time averaged image presents a modulation at least to the 5 Mm distance, suggesting next persistent structures configurations. By excluding the first peak, this modulation is periodic with $P \sim 0.6\ Mm$. Therefore the granulation persistent pattern seems to be organized, with a topological order incompatible with the hard sphere random close packing model. This organization, as suggested by preliminary numerical simulations, is possibly due to clustering effects in the pattern.

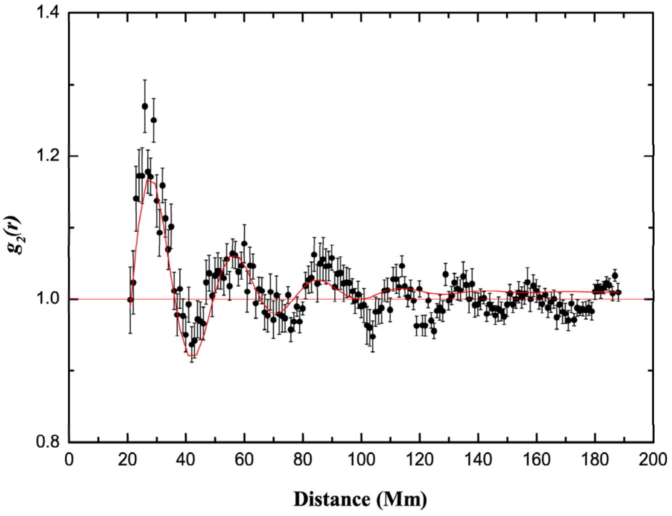

Figure 7.7: $< g_2(r) >$ of 12 single divergence maps from MDI dataset. Error bars represent the standard error of the sample mean. The superimposed red solid line is a dampened cosine fit (cfr. Eq. 7.5.1).

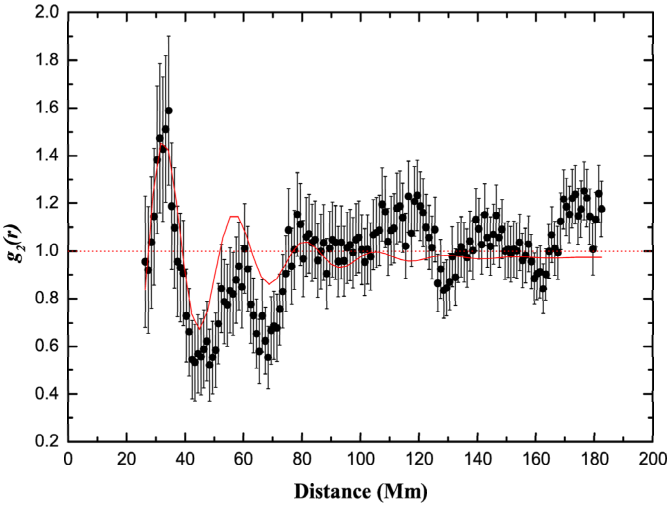

Figure 7.8: $g_2(r)$ signal extracted from the time-averaged MDI dataset. Error bars represent the standard deviation from the mean. The superimposed red solid line is a dampened cosine fit (cfr. Eq. 7.5.1).

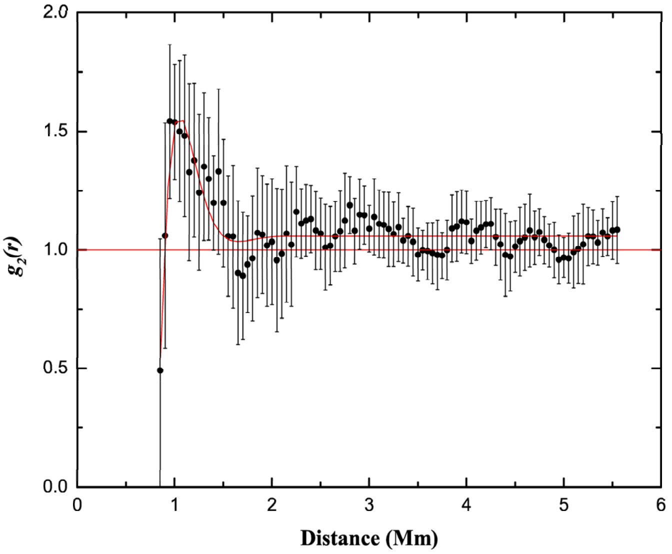

Figure 7.9: $< g_2(r) >$ of 12 single divergence maps from THEMIS99 dataset. Error bars represent the standard error of the sample mean. The superimposed red solid line is a dampened cosine fit (cfr. Eq. 7.5.1).

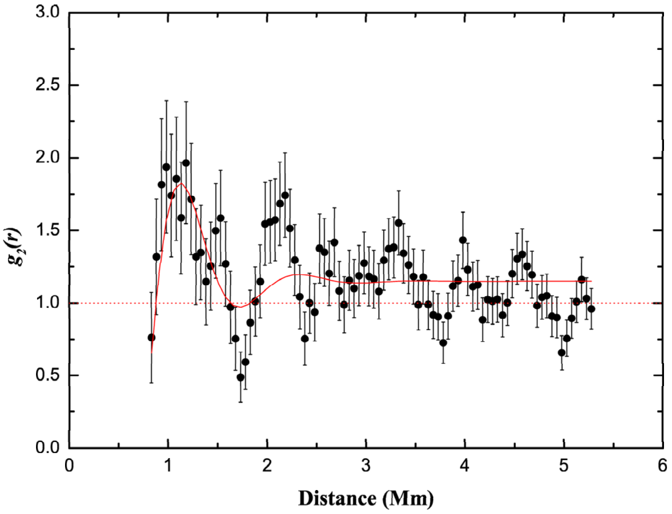

Figure 7.10: $g_2(r)$ signal extracted from the time-averaged THEMIS99 dataset. Error bars represent the standard deviation from the mean. The superimposed red solid line is a dampened cosine fit (cfr. Eq. 7.5.1).

Chapter 8

Conclusions

In this work the dynamics, the evolution and the topology of photospheric plasma features at different spatial and temporal scales has been investigated. In particular, the characteristics of the three 'classic' scales of photospheric convection, namely, granulation, mesogranulation and supergranulation, have been studied.

8.1 Discussion of the Results Presented in This Thesis

The results presented in this thesis can be recapitulated as follow:

1. In order to describe the granule lifetime distributions, an exponential decay law has been employed by several authors, therefore retrieving a 'typical' lifetime for the granulation (Alissandrakis et al., 1987).
   This function, when fitted to lifetime distributions obtained by the TST procedure (Figures 5.3 and 7.2), results inappropriate to represent the distribution behaviours, either for short or for long granule duration.
   In particular, the decay law seems to be at least twofold, indicating different regimes for $t <\sim 2.5$ or $t >\sim 2.5$ minutes. This result can be explained by the existence of a population with an extended range of decay times. Moreover, comparable distributions were reported by Brandt et al. (1991); Title et al. (1989), with a similar excess of short lived granules in their lifetime histograms.
   Instead, a stretched exponential decay law (cfr. Eq. 5.5) is much more suited to describe the granulation lifetime histogram (Figure 5.3).
   As a consequence, defining a 'typical' time for granulation is an oversimplification, as a stretched exponential decay law implies a whole range of decay time, suggesting a dynamic heterogeneity of the granulation phenomenon.
   Moreover, this dynamic heterogeneity is detected also in the size distribution of granular structures: the granulation presents a monotonic size distribution, without a preferential spatial scale.

Therefore, neither a 'typical' spatial scale can be detected for granulation, with the notable exception of the upper limit: the size distributions essentially range from the observation resolution limit to 1.5"-2" granular structures, with the largest structures very often, if not always, associated to exploding granules.

2. The analysis of persistent sites points out that a mesogranular clustering scale emerges at time scales typical of evolution of energetic (exploding) granules.
   More in detail, for times shorter than 5 minutes, the hexagonal information entropy has a peak in the granulation spatial scale range; successively, on time scales of about 15-20 minutes, the persistent sites form clusters characterized by a spatial scale around 8 Mm, classically associated to mesogranulation (Figure 7.3).
   The maximum of large scale entropy is reached after about 15 minutes, indicating that at this time we attain the maximum efficiency in persistent sites clustering.
   The properties described above appear consistent with the hypothesis that large-scales structures arise naturally from a collective interaction of many small-scale features (Cattaneo et al. (2001); Rast (2003b)).

3. To support the hypothesis that clustering occurs mainly under the influence of granulation dynamics, we investigate the time dependence of the ratio $H'_{hex}(r_8)/H'_{hex}(r_1)$ between the hexagonal normalized information entropies associated, respectively, to the 8 Mm and 1 Mm length-scales (Figure 7.4). We retrieved that the typical grow time of the contribution of $H'_{hex}(r_8)$ to the whole $H'_{hex}(r)$ signal is $\tau_{gw} \sim 10\ min$. Moreover, the $< H'_{hex}(r_8) > / < H'_{hex}(r_1) >$ behaviour indicates that the maximum efficiency in persistent sites clustering is reached at $\sim 6\ min$, i.e. at about twice the classic 'typical' granulation time-scale, the granular spatial-scale is no more contributing significantly to the $H'_{hex}(r)$ signal.
   We remember that the temporal behaviour of $H'(r)$ maximum describes the time evolution of the mean ordering length scale of long living granular structures and that in this analysis very small granules are filtered out by the strict selection rules we imposed. We are confident that small granules would not modify our results because small granules are statistically short lived and therefore not important on time scales longer than 1-2 minutes.

4. The results presented in this thesis point towards the interpretation of mesogranulation as a complex time-scale process involving energetic granules or as a natural extension of the granulation spatial and temporal scales (Straus and Bonaccini, 1997).
   The analysis of the horizontal velocity field near an exploding granule seems to support these conclusions, as it shows how an exploding granule may create a divergence signal on the mesogranular scale by displacing its neighbours. We conclude that there is a good consistency between these spatial and time scales and those associated to the exploding granule process (Hirzberger et al. (1999a); Berrilli et al. (2002)).

5. By applying the $g_2(r)$ analysis to suitably rescaled granulation and supergranulation image series, a comparison of supergranular and granular order topology is performed.
   More in detail, we comput the $< g_2(r) >$ signal (Fig. 7.7), obtained averaging the $g_2(r)$ signals extracted from single divergence maps, and the $g_2(r)$ of the persistent field (Fig. 7.8), i.e., of the image obtained summing up the single binarized divergence maps (Figure 7.5). These two signals, both showing dampened oscillatory behaviours, are analyzed in the context of a hard sphere random packing model, detecting no interaction but the first-neighbourhood one.
   The results obtained for single and time averaged maps seem to suggest that the supergranulation pseudo-organized pattern persists for at least 4 days. This leads us to conclude that the supergranular structures topological order is irreconcilable with a completely random field, and is suitably described by a simple hard sphere model, i.e., a collection of plasma blobs, mutually impenetrable, close packed and without, or with a very weak, long-range interaction.
   Instead, the analysis of the $< g_2(r) >$ retrieved by single granulation images (Figure 7.9) reveals that the topological order of the instantaneous granulation pattern is not consistent with the hard sphere model, but it is compatible with a random distribution of soft features with a very wide distribution in sizes (Ziman, 1979).
   Some kind of organization is detected in the $g_2(r)$ analysis of persistent granulation pattern, which is still irreconcilable with a hard sphere model, but more ordered than instantaneous granulation patterns, nevertheless.
   It is worth noting that this emerging spatial scale is a sort of correlation length scale for these structures.
   From these analyses, it can be deduced that supergranulation and granulation patterns present a different topological order.
   Specifically, the granulation behaves as a quite random distribution of soft plasma features with a very wide distribution in size, while supergranulation behaves as a random distribution of close packed, coherent stiff features with a rather defined mean size.
   In the case of single fields (Figures 7.9 and 7.7), this fact could be related to the greater malleability of the granular structures and to the broader distribution of granules sizes. As already stated, while in the case of supergranulation a mean cell size can be easily defined, the size distribution of granulation does not show a clear maximum up to the resolution limit of the used images (Del Moro, 2004). In the case of time averaged fields (Figures 7.10 and 7.8), a secondary topological organization seems to emerge only in granulation patterns, while the supergranulation seems to loosen a bit its spatial coherence.
   As a consequence of these results we can state that the analyzed granulation and supergranulation patterns present very different ordering topologies and that the conclusion that supergranulation and granulation geometry is similar, apart from scale (Schrijver et al., 1997), cannot be extended to the topological location of supergranular and granular structures.

6. The computation of a mean supergranular lifetime is performed by fitting an exponential decay function to the lifetimes retrieved by the TST procedure when applied to MDI heliotomographic divergence maps. The value obtained by such a fit ($\simeq 18$ hours) is corrected by taking into account the effect introduced by the limited temporal window. After this correction the final estimate for supergranule mean lifetime is $\simeq 22$ hours. It is worth noting that in the case of supergranulation a simple exponential decay is well suited to describe the retrieved lifetime histogram.

7. The study of the full 3D velocity field of a supergranule shows that strong downflow are located on the border and in the centre of the supergranular structure, but also that the mean granular flow regresses from the centre to the periphery of the SG. Moreover, tracked granules are denser near the periphery of the SG, denoting a tendency of granular scale structures characteristic to vary with the relative position in the supergranule. Since the work of November et al. (1981), several authors have tried to correlate granular properties with their position in mesogranular cells (see for example Brandt et al. (1991)). This seems to occur also with their position in supergranular cells.

8.2 Future Research

Further studies can improve and verify the results given in this work.

In fact, it is worth remembering that the ordering topology analysis proposed in this work is far from being a conclusive approach to the study of the complex topology of convective plasma structures observed on the Sun. Different proxies for supergranulation and granulation fields and different analytical describers of topology in such structures are necessary to finally answer the questions about the actual nature of supergranulation and granulation and completely define the convective regime of the outer layer of our star.

Additional analysis involving photospheric intensity and velocity fields would be important in confirming our insights. Polarimetric and photometric high precision observations, coupled with clever radiative transport models in presence of weak and strong magnetic features, would be necessary to definitely confirm or disprove the convective origin of temperature fluctuation associated to large-scale photospheric features.

The agreement between the computed evolutionary times and typical time scale associated to energetic granules makes the hypothesis of a collective origin for mesogranulation more likely, but the hypothesis of a purely convective mesogranulation can not be completely ruled out.

Nevertheless, this work would represent a first step in the analysis of global properties of different photospheric plasma structures.

8.3 Personal Bibliography

The research work presented in this thesis led to the publication of the following referred papers and conference communications:

Granulation structure and information entropy
Berrilli, F., Consolini, G., Florio, A., Del Moro, D. and Pietropaolo, E.
Astronomische Nachrichten /AN vol. 324, No. 4, pag. 405, 2003a
Characterization of supergranular features via topological measures
Berrilli, F., Del Moro, D., Giordano, S., Consolini G., Kosovichev, A.
ESA SP-535 *for ISCS2003*, pag. 47, 2003b
Granules and Supergranules properties derived from solar timeseries
Del Moro, D., Berrilli, F., Bonet, J.A., Consolini, G., Kosovichev, A., Pietropaolo, E.
Memorie della Societá Astronomica Italiana vol. 74 N.3, pag. 584, 2003a
Phase diversity at THEMIS : first implementation
Del Moro, D., Criscuoli, S., Bonet, J.A., Marquez, I., Lemen, C., Briand, S.
Memorie della Societá Astronomica Italiana vol. 74 N.3, pag. 811, 2003b
Phase diversity at THEMIS : first implementation
Del Moro, D., Lemen, C., Bonet, J.A., Marquez, I., Criscuoli, S., Briand, S.
Astronomische Nachrichten /AN vol. 324, No. 4, pag. 299, 2003c
Structure Properties of Supergranulation and Granulation
Berrilli, F., Del Moro, D., Consolini G., Pietropaolo, E. and Duvall, T.L., Jr., Kosovichev, A.G.
Solar Physics vol. 221, pag. 33, 2004
Dynamics and Structure of Supergranulation
Del Moro, D., Berrilli, F., and Duvall, T.L., Jr., Kosovichev, A.G.
Solar Physics vol. 221, pag. 23, 2004
Solar granulation properties derived from three different time series
Del Moro, D.
Astronomy and Astrophysics vol. 428, pag. 1007, 2004
The sensitivity of the C I 538.0 nm Fe I 537.9 nm and Ti II 538.1 nm lines to the active region presence
Penza, V., Caccin, B., Del Moro, D.
Astronomy and Astrophysics vol. 427, pag. 345, 2004
Segmentation of solar features
Berrilli, F., Del Moro, D., Florio, A., Santillo, L.
Solar Physics (accepted), 2005a
Magnetic network dynamics in photosphere
Berrilli, F., Del Moro, D., Giordano, S., Pietropaolo, E.
Advances in Space Research: COSPAR04 (submitted), 2005b
Spatial clustering of photospheric structures
Berrilli, F., Del Moro, D., Russo, S., Consolini, G., Straus, Th.
Astrophysical Journal (accepted), 2005c
First implementation of Phase Diversity at THEMIS
Criscuoli, S., Del Moro, D., Bonet, J.A., Marquez, I.
Solar Physics (accepted), 2005

Bibliography

Öhman, Y. (1938). Über den Quarz-Säule-Monochromator. In *Professor Östen Bergstrand Vetenskapsmannen Och Läraren*, page 138.

Abdussamatov, H. I. (1993). The fine structure of solar granulation and its relationship to large-scale photospheric structures. *Astronomy and Astrophysics*, 272:580.

Abdussamatov, H. I. (2000). Mesostructure of the Solar Granulation. *Astronomy Letters*, 26:192–197.

Abdussamatov, H. I. and Zlatopolo'skii, A. G. (1997). Variation of fine-structure properties of solar granulation on a mesogranular scale. *Astronomy Letters*, 23:752–757.

Aki, K. and Richards, P. G. (1980). *Quantitative Seismology Theory and Methods*. W.H.Freeman and Company.

Alissandrakis, C. E., Dialetis, D., and Tsiropoula, G. (1987). Determination of the mean lifetime of solar features from photographic observations. *Astronomy and Astrophysics*, 174:275–280.

Andraud, C., Beghdadi, A., Haslund, E., Hilfer, R., Lafait, J., and Virgin, B. (1997). Local entropy characterization of correlated random microstructures. *Physica A*, 235:307.

Andraud, C., Beghdadi, A., and Lafait, J. (1994). Entropic analysis of random morphologies. *Physica A*, 207:208.

Böhm-Vitense, E. (1958). Über die Wasserstoffkonvektionszone in Sternen verschiedener Effektivtemperaturen und Leuchtkräfte. Mit 5 Textabbildungen. *Zeitschrift fur Astrophysics*, 46:108.

Bachmann, K. T., Khatri, G., Petitto, J. M., and Hathaway, D. H. (1997). Mesogranulation as a Distinct Scale of Convection in the Sun. *Bulletin of the American Astronomical Society*, 29:1324.

Backus, G. E. and Gilbert, J. F. (1970). Uniqueness in the Inversion of Inaccurate Gross Earth Data. *Royal Society of London Philosophical Transactions Series A*, 266:123–192.

Beck, C. and Schlogl, F. (1993). Books-Received - Thermodynamics of Chaotic Systems - an Introduction. *Science*, 262:2073.

Beckers, J. M. and Milkey, R. W. (1975). The line response function of stellar atmospheres and the effective depth of line formation. *Solar Physics*, 43:289–292.

Bellot Rubio, L. R., Ruiz Cobo, B., and Collados, M. (1997). (Erratum) Response functions for the inversion of data from unresolved solar magnetic elements. *Astronomy and Astrophysics*, 319:1036–1036.

Ben-Menahem, A. (1964). Seismology. *Bulletin of the Seismologists Society of America*, 54:1315.

Berger, T. E. (1996). Observation and Analysis of Small-scale Solar Magnetic Structure. *Bulletin of the American Astronomical Society*, 28:869.

Berger, T. E., Löfdahl, M. G., Shine, R. S., and Title, A. M. (1998). Measurements of Solar Magnetic Element Dispersal. *Astrophysical Journal*, 495:973.

Berger, T. E., Schrijver, C. J., Shine, R. A., Tarbell, T. D., Title, A. M., and Scharmer, G. (1995). New Observations of Subarcsecond Photospheric Bright Points. *Astrophysical Journal*, 454:531.

Berger, T. E. and Title, A. M. (2001). On the Relation of G-Band Bright Points to the Photospheric Magnetic Field. *Astrophysical Journal*, 553:449–469.

Berrilli, F., Consolini, G., Florio, A., Del Moro, D., and Pietropaolo, E. (2003a). Granulation structure and information entropy. *Astronomische Nachrichten*, 324:405.

Berrilli, F., Consolini, G., Florio, A., and Pietropaolo, E. (2001). Solar granulation: properties of velocity fields from THEMIS-IPM observations. *Memorie della Societá Astronomica Italiana*, 72:669–672.

Berrilli, F., Consolini, G., Pietropaolo, E., Caccin, B., Penza, V., and Lepreti, F. (2002). 2-D multiline spectroscopy of the solar photosphere. *Astronomy and Astrophysics*, 381:253–264.

Berrilli, F., Del Moro, D., Consolini, G., Pietropaolo, E., Duvall, T. L., and Kosovichev, A. G. (2004). Structure Properties of Supergranulation and Granulation. *Solar Physics*, 221:33–45.

Berrilli, F., Del Moro, D., Florio, A., and Santillo, L. (2005a). Segmentation of photospheric and chromospheric solar features. *Accepted by Solar Physics.*

Berrilli, F., Del Moro, D., Giordano, S., Consolini, G., and Kosovichev, A. (2003b). Characterization of supergranular features via topological measures. In *ESA SP-535: Solar Variability as an Input to the Earth's Environment*, pages 47–52.

Berrilli, F., Del Moro, D., Giordano, S., and Pietropaolo, E. (2005b). Magnetic network dynamics in photosphere. In *Advances in Space Research: COSPAR04 (submitted).*

Berrilli, F., Del Moro, D., Russo, S., Consolini, G., and Straus, T. (2005c). Spatial clustering of photospheric structures. *Accepted by Astrophysical Journal.*

Berrilli, F., Ermolli, I., Florio, A., and Pietropaolo, E. (1999). Average properties and temporal variations of the geometry of solar network cells. *Astronomy and Astrophysics*, 344:965–972.

Biermann, L. (1948). Konvektion in rotierenden Sternen. *Zeitschrift fur Astrophysics*, 25:135.

Blum, H. (1967). A transformation for extracting new descriptors of shape. In Wathen-Dunn, W., editor, *Proc. Models for the Perception of Speech and Visual Form*, pages 362–380, Cambridge, MA. MIT Press.

Boltzmann, L. (1872). Further studies on the Thermal Equilibrium of Gas Molecules. *Sitzungsberichte der kaiserlichen Akademie der Wissenschaften*, 66:275– 370.

Boltzmann, L. (1877). On the Relation of a General Mechanical Theorem to the Second Law of Thermodynamics. *Sitzungsberichte der kaiserlichen Akademie der Wissenschaften*, 75:67–73.

Boltzmann, L. (1896). Reply to Zermelo's remarks on the Theory of Heat. *Annalen der Physik*, 57:773–784.

Boltzmann, L. (1897). On Zermelo's paper "On the Mechanical Explanation of Irreversible Processes". *Annalen der Physik*, 60:392.

Bonaccini, D., Righini, A., Cavallini, F., and Ceppatelli, G. (1989). High resolution solar bidimensional spectroscopy with a universal birefringent filter in tandem with a Fabry-Perot interferometer. *Astronomy and Astrophysics*, 217:368–374.

Bonet, J. A., Márquez, I., Muller, R., Sobotka, M., and Tritschler, A. (2004). Phase diversity restoration of sunspot images. I. Relations between penumbral and photospheric features. *Astronomy and Astrophysics*, 423:737–744.

Bousquet, P. (1969). *Spectroscopie instrumentale.* Dunod Universite, Paris: Dunod, 1969.

Bovelet, B. and Wiehr, E. (2001). A New Algorithm for Pattern Recognition and its Application to Granulation and Limb Faculae. *Solar Physics*, 201:13–26.

Bracewell, R. N. (1968). *The Fourier Transform and its Applications.* McGraw-Hill.

Brandt, P. N., Ferguson, S., Shine, R. A., Tarbell, T. D., and Scharmer, G. B. (1991). Variation of granulation properties on a mesogranular scale. *Astronomy and Astrophysics*, 241:219–226.

Braun, D. C., Duvall, T. L., and Labonte, B. J. (1987). Acoustic absorption by sunspots. *Astrophysical Journal Letters*, 319:L27–L31.

Bray, R. J., Loughhead, R. E., and Durant, C. J. (1984). Book-Review - the Solar Granulation. *Astronomy Express*, 1:39.

Brown, D. R. (1975). An empirical study of chromospheric fine structure based on simultaneous spectrograms in the H, K, 8498 A and 8542 A lines of CaII. *Ph.D. Thesis.*

Brown, T. M., Christensen-Dalsgaard, J., Dziembowski, W. A., Goode, P., Gough, D. O., and Morrow, C. A. (1989). Inferring the sun's internal angular velocity from observed p-mode frequency splittings. *Astrophysical Journal*, 343:526–546.

Brune, R. and Woehl, H. (1982). On the size and structure of bright solar Ca^+-network cells depending on the heliographic position. *Solar Physics*, 75:75–78.

Buonaura, B. and Caccin, B. (1982). Velocity fields and spectral line asymmetries - A linearized analytical approach to the theory of the line bisector in a Milne-Eddington atmosphere. *Astronomy and Astrophysics*, 111:113–116.

Caccin, B., Gomez, M. T., Marmolino, C., and Severino, G. (1977). Response functions and contribution functions of photospheric lines. *Astronomy and Astrophysics*, 54:227–231.

Caccin, B. and Marmolino, C. (1980). On the retrieval of velocity gradients from photospheric line asymmetries - A linearized approach. *Astronomy and Astrophysics*, 83:73–78.

Caccin, B. and Penza, V. (2000). Line-Depth and T_{eff} Variations with the Solar Cycle due to Possible Size-Changes of Photospheric Granulation. In *ESA SP-463: The Solar Cycle and Terrestrial Climate, Solar and Space weather*, page 293.

Caccin, B. and Penza, V. (2002). Line-depth and T_{eff} variations with the solar cycle. In *ESA SP-477: Solspa 2001, Proceedings of the Second Solar Cycle and Space Weather Euroconference*, pages 205–208.

Canfield, R. C. (1976). The height variation of granular and oscillatory velocities. *Solar Physics*, 50:239–254.

Canfield, R. C. and Mehltretter, J. P. (1973). Fluctuations of Brightness and Vertical Velocity at Various Heights in the Photosphere. *Solar Physics*, 33:33.

Canfield, R. C. and Stencel, R. E. (1976). Emission lines in the wings of CA II H and K. I - Initial solar observations and implications. *Astrophysical Journal*, 209:618–620.

Canuto, V. M. and Mazzitelli, I. (1991). Stellar turbulent convection - A new model and applications. *Astrophysical Journal*, 370:295–311.

Canuto, V. M. and Mazzitelli, I. (1992). Further improvements of a new model for turbulent convection in stars. *Astrophysical Journal*, 389:724–730.

Carlier, A., Chauveau, F., Hugon, M., and Rösch, J. (1968). Cinématographie à Haute Résolution Spatiale de la Granulation Photosphérique. *Academie des Science Paris Comptes Rendus Serie B Sciences Physiques*, 266:199–201.

Carreras, R. A. (1993). Image restoration using nonlinear optimization techniques with a knowledge-based constraint. In *Proc. SPIE Vol. 2029, p. 209-226, Digital Image Recovery and Synthesis II, Paul S. Idell; Ed.*, pages 209–226.

Cattaneo, F., Lenz, D., and Weiss, N. (2001). On the Origin of the Solar Mesogranulation. *Astrophysical Journal*, 563:L91–L94.

Cauzzi, G., Consolini, G., Berrilli, F., Smaldone, L. A., Straus, T., Bavassano, B., Bruno, R., Caccin, B., Carbone, V., Egidi, A., Ermolli, I., Florio, A., and Pietropaolo, E. (1998). Properties of solar granulation cells in quiet regions as derived from a time series of white light images. *Memorie della Societá Astronomica Italiana*, 69:647.

Chapman, G. A., Walton, S. R., Bird, M., Bulharowski, T., Cordero, E., Gluszczak, M., Mach, C., Manes, J., Parker, D., and Wagner, J. (1988). Full Disk CaII K-line Observations of the Sun with a One-Inch Telescope (CFDT). *Bulletin of the American Astronomical Society*, 20:910.

Chavanne, X., Chillà, F., Castaing, B., Hébral, B., Chabaud, B., and Chaussy, J. (1997). Observation of the Ultimate Regime in Rayleigh-Bénard Convection. *Physics Review Letters*, 79:3648–3651.

Chavanne, X., Chillà, F., Chabaud, B., Castaing, B., and Hébral, B. (2001). Turbulent Rayleigh–Bènard convection in gaseous and liquid He. *Physics of Fluids*, 13(5):1300–1320.

Chen, H., Chou, D., Chang, H., Sun, M., Yeh, S., Labonte, B., and The TON Team (1998). Probing the Subsurface Structure of Active Regions with the Phase Information in Acoustic Imaging. *Astrophysical Journal Letters*, 501:L139+.

Chevalier, S. (1908). Contribution to the Study of the Photosphere. *Astrophysical Journal*, 27:12.

Chiam, K. H., Paul, M. R., Cross, M. C., and Greeside, H. S. (2003). Mean flow and spiral defect chaos in Rayleigh–Bènard convection. *Physical Review E*, 67:056206– 056219.

Chou, D.-Y., Chen, C.-S., Ou, K.-T., and Wang, C.-C. (1992). Power spectra of median- and small-scale solar convection. *Astrophysical Journal*, 396:333–339.

Chou, D.-Y., Labonte, B. J., Braun, D. C., and Duvall, T. L. (1991). Power spectra of solar convection. *Astrophysical Journal*, 372:314–320.

Christensen-Dalsgaard, J., Schou, J., and Thompson, M. J. (1990). A comparison of methods for inverting helioseismic data. *Monthly Notices of the Royal Astronomical Society*, 242:353–369.

Consolini, G., Berrilli, F., Florio, A., Pietropaolo, E., and Smaldone, L. A. (2003). Information entropy in solar atmospheric fields. I. Intensity photospheric structures. *Astronomy and Astrophysics*, 402:1115–1127.

Couvidat, S., García, R. A., Turck-Chièze, S., Corbard, T., Henney, C. J., and Jiménez-Reyes, S. (2003). The Rotation of the Deep Solar Layers. *Astrophysical Journal*, 597:L77–L79.

Craig, I. J. D. and Brown, J. C. (1986). *Inverse problems in astronomy: A guide to inversion strategies for remotely sensed data.* Research supported by SERC. Bristol, England and Boston, MA, Adam Hilger, Ltd., 1986, 159 p.

Criscuoli, S., Del Moro, D., Bonet, J. A., and Márquez, I. (2005). First implementation of Phase Diversity at THEMIS. *Accepted by Solar Physics.*

Cross, M. C. and Hohenberg, P. C. (1993). Pattern formation outside of equilibrium. *Reviews of Modern Physics*, 65:851–1112.

Dame, L. and Martic, M. (1987). Observation and oscillatory properties of mesostructures in the solar chromosphere. *Astrophysical Journal*, 314:L15–L19.

de Boer, C. R., Kneer, F., and Nesis, A. (1992). Speckle observations of solar granulation. *Astronomy and Astrophysics*, 257:L4–L6.

de Jager, C. (1952). The hydrogen spectrum of the sun. *Recherches Astronomiques de l'Observatoire d'Utrecht*, 1.

De Rosa, M., Duvall, T. L., and Toomre, J. (2000). Near-Surface Flow Fields Deduced Using Correlation Tracking and Time-Distance Analyses. *Solar Physics*, 192:351–361.

Del Moro, D. (2004). Solar granulation properties derived from three different timeseries. *Astronomy and Astrophysics*, 428:1007–1015.

Del Moro, D., Berrilli, F., Bonet, J. A., Consolini, G., Kosovichev, A., and Pietropaolo, E. (2003a). Granule and Supergranule properties derived from solar timeseries. *Memorie della Societtá Astronomica Italiana*, 74:584.

Del Moro, D., Berrilli, F., Duvall, T. L., and Kosovichev, A. G. (2004). Dynamics and Structure of Supergranulation. *Solar Physics*, 221:23–32.

Del Moro, D., Criscuoli, S., Bonet, J. A., Márquez, I., Lemen, C., and Briand, C. (2003b). Phase diversity at THEMIS : first implementation. *Memorie della Societá Astronomica Italiana*, 74:811.

Del Moro, D., Lemen, C., Bonet, J. A., Márquez, I., Criscuoli, S., and Briand, C. (2003c). Phase diversity at THEMIS : first implementation. *Astronomische Nachrichten*, 324:299.

Deubner, F. (1971). Some Properties of Velocity Fields in the Solar Photosphere. III: Oscillatory and Supergranular Motions as a Function of Height. *Solar Physics*, 17:6.

Deubner, F. (1989). Mesogranulation - A convective phenomenon. *Astronomy and Astrophysics*, 216:259–264.

Deubner, F.-L. (1975). Observations of low wavenumber nonradial eigenmodes of the sun. *Astronomy and Astrophysics*, 44:371–375.

Dialetis, D., Macris, C., Prokakis, T., and Muller, R. (1988). A possible relation between lifetime and location of solar granules. *Astronomy and Astrophysics*, 204:275–278.

Dialetis, D., Macris, C., Prokakis, T., and Sarris, E. (1986). The lifetime and evolution of solar granules. *Astronomy and Astrophysics*, 168:330–334.

Domínguez Cerdeña, I., Sánchez Almeida, J., and Kneer, F. (2003). Internetwork magnetic fields observed with sub-arcsec resolution. *Astronomy and Astrophysics*, 407:741–757.

Duvall, T. L. (1980). The equatorial rotation rate of the supergranulation cells. *Solar Physics*, 66:213–221.

Duvall, T. L. (1998). Recent Results and Theoretical Advances in Local Helioseismology. In *Structure and Dynamics of the Interior of the Sun and Sun-like Stars SOHO 6/GONG 98 Workshop Abstract, June 1-4, 1998, Boston, Massachusetts, p. 581*, page 581.

Duvall, T. L. and Gizon, L. (2000). Time-Distance Helioseismology with f Modes as a Method for Measurement of Near-Surface Flows. *Solar Physics*, 192:177–191.

Duvall, T. L., Jefferies, S. M., Harvey, J. W., and Pomerantz, M. A. (1993). Time-distance helioseismology. *Nature*, 362:430–432.

Duvall, T. L., Kosovichev, A. G., Scherrer, P. H., Bogart, R. S., Bush, R. I., de Forest, C., Hoeksema, J. T., Schou, J., Saba, J. L. R., Tarbell, T. D., Title, A. M., Wolfson, C. J., and Milford, P. N. (1997). Time-Distance Helioseismology with the MDI Instrument: Initial Results. *Solar Physics*, 170:63–73.

Duvall, T. L. J., D'Silva, S., Jefferies, S. M., Harvey, J. W., and Schou, J. (1996). Downflows Under Sunspots Detected by Helioseismic Tomography. *Nature*, 379:235.

Engvold, O. (1966). *Measurements of the center-limb variation in the H- and K-lines of CaII in undisturbed and active regions on the sun.* Oslo, Universitetsforlagets tryknings sentral, 1966.

Florio, A. and Berrilli, F. (1998). A skeletonizing algorithm for granulation and super-granulation cell finding. *Memorie della Societá Astronomica Italiana*, 69:655.

Frank, Z., Muller, R., Roudier, T., Vigneau, J., Shine, R., Tarbell, T., Title, A., Topka, K., and Simon, G. (1989). Proper Motion and Lifetime of Mesogranules. *Bulletin of the American Astronomical Society*, 21:841.

Frazier, E. N. (1970). Multi-Channel Magnetograph Observations. II. Supergranulation. *Solar Physics*, 14:89.

Gadun, A. S., Hanslmeier, A., Pikalov, K. N., Ploner, S. R. O., Puschmann, K. G., and Solanki, S. K. (2000). Size-dependent properties of simulated 2-D solar granulation. *Astronomy and Astrophysics Supplement*, 146:267–291.

Gates, E. L., Restaino, S. R., Carreras, R. A., Dymale, R. C., and Loos, G. C. (1994). Phase diversity as an on-line wavefront sensor: experimental results. In *Image Reconstruction and Restoration, Proc. Soc. Photo-Opt. Instrum. Eng., SPIE 2302*, page 330.

Getling, A. V. and Brandt, P. N. (2002). Regular structures of the solar photosphere. (Persistence of the granular field and trenching in the brightness relief). *Astronomy and Astrophysics*, 382:L5–L8.

Ginet, G. P. and Simon, G. W. (1992). On the evidence for mesogranules in solar power spectra. *Astrophysical Journal*, 386:359–363.

Gingerich, O., Noyes, R. W., Kalkofen, W., and Cuny, Y. (1971). The Harvard-Smithsonian reference atmosphere. *Solar Physics*, 18:347–365.

Giovanelli, R. G. (1980). The supergranule velocity field. *Solar Physics*, 67:211–228.

Giovanelli, R. G. and Slaughter, C. (1978). Motions in solar magnetic tubes. I - The downflow. *Solar Physics*, 57:255–260.

Gizon, L. and Birch, A. C. (2002). Time-Distance Helioseismology: The Forward Problem for Random Distributed Sources. *Astrophysical Journal*, 571:966–986.

Glazier, J. A., Segawa, T., Naert, A., and Sano, M. (1999). Evidence Against Ultrahard Thermal Turbulence at Very High Rayleigh Numbers. *Nature*, 398:307–310.

Gonsalves, R. A. (1982). Phase retrieval and diversity in adaptive optics. *Optical Engineering*, 21:829–832.

Gonsalves, R. A. and Childlaw, R. (1979). Wavefront Sensing by Phase Retrieval. In Teschner, A. G., editor, *Proc. SPIE, 32, Applications of Digital Image Processing III*, page 32.

Gonzalez, R. and Wintz, P. (1987). *Digital Image Processing*. Addison-Wesley, 2nd edition.

Gough, D. and Toomre, J. (1991). Seismic observations of the solar interior. *Annual Review of Astronomy and Astrophysics*, 29:627–685.

Gough, D. O. (1978). New Data from Solar Oscillations. *Nature*, 274:739.

Hagenaar, H. J., Schrijver, C. J., and Title, A. M. (1997). The Distribution of Cell Sizes of the Solar Chromospheric Network. *Astrophysical Journal*, 481:988.

Hansky, A. (1908). Mouvement des granules sur la surface DU soleil. *Mitteilungen der Nikolai-Hauptsternwarte zu Pulkowo*, 3.

Hart, A. B. (1954). Motions in the Sun at the photospheric level. IV. The equatorial rotation and possible velocity fields in the photosphere. *Monthly Notices of the Royal Astronomical Society*, 114:17.

Hart, A. B. (1956). Motions in the Sun at the photospheric level. VI. Large-scale motions in the equatorial region. *Monthly Notices of the Royal Astronomical Society*, 116:38.

Hathaway, D. H., Beck, J. G., Bogart, R. S., Bachmann, K. T., Khatri, G., Petitto, J. M., Han, S., and Raymond, J. (2000). The Photospheric Convection Spectrum. *Solar Physics*, 193:299–312.

Hathaway, D. H., Beck, J. G., Han, S., and Raymond, J. (2002). Radial Flows in Supergranules. *Solar Physics*, 205:25–38.

Havel, I. (1995). Scale Dimensions in Nature. *International Journal of General Systems*, 23(2):303–332.

Herschel, W. (1801). Observations Tending to Investigate the Nature of the Sun, in Order to Find the Causes or Symptoms of Its Variable Emission of Light and Heat; With Remarks on the Use That May Possibly Be Drawn from Solar Observations. *Philosophical Transaction Royal Society of London*, 91:265.

Hill, F. (1988). Rings and trumpets - Three-dimensional power spectra of solar oscillations. *Astrophysical Journal*, 333:996–1013.

Hirzberger, J., Bonet, J. A., Sobotka, M., Vázquez, M., and Hanslmeier, A. (2002). Fine structure and dynamics in a light bridge inside a solar pore. *Astronomy and Astrophysics*, 383:275–282.

Hirzberger, J., Bonet, J. A., Vázquez, M., and Hanslmeier, A. (1999a). Time Series of Solar Granulation Images. II. Evolution of Individual Granules. *Astrophysical Journal*, 515:441–454.

Hirzberger, J., Bonet, J. A., Vázquez, M., and Hanslmeier, A. (1999b). Time Series of Solar Granulation Images. III. Dynamics of Exploding Granules and Related Phenomena. *Astrophysical Journal*, 527:405–414.

Hirzberger, J., Vazquez, M., Bonet, J. A., Hanslmeier, A., and Sobotka, M. (1997). Time Series of Solar Granulation Images. I. Differences between Small and Large Granules in Quiet Regions. *Astrophysical Journal*, 480:406.

Hoekzema, N. M. and Brandt, P. N. (2000). Small-scale topology of solar atmosphere dynamics. IV. On the relation of photospheric oscillations to meso-scale flows. *Astronomy and Astrophysics*, 353:389–395.

Holweger, H. and Mueller, E. A. (1974). The photospheric barium spectrum - Solar abundance and collision broadening of BA II lines by hydrogen. *Solar Physics*, 39:19–30.

Janssen, M. (1878). M. Janssen's photographs of the Sun. *Monthly Notices of the Royal Astronomical Society*, 38:202.

Janssens, T. J. (1970). Long Term Observations of the Hα Chromospheric Network. *Solar Physics*, 11:222.

Jefferies, S. M., Osaki, Y., Shibahashi, H., Duvall, T. L., Harvey, J. W., and Pomerantz, M. A. (1994). Use of acoustic wave travel-time measurements to probe the near-surface layers of the Sun. *Astrophysical Journal*, 434:795–800.

Jensen, J. M., Jacobsen, B. H., and Christensen-Dalsgaard, J. (1999). Sensitivity Kernels for Time-Distance Inversion. In *SOHO-9 Workshop on Helioseismic Diagnostics of Solar Convection and Activity.*

Kawaguchi, I. (1980). Morphological study of the solar granulation - The fragmentation of granules. *Solar Physics*, 65:207–220.

Keenan, P. C. (1938). Dimensions of the Solar Granules. *Astrophysical Journal*, 88:360.

Keil, S. L. (1980a). The Structure of Solar Granulation - Part Two - Models of Vertical Motion. *Astrophysical Journal*, 237:1035.

Keil, S. L. (1980b). The structure of solar granulation. I - Observations of the spatial and temporal behavior of vertical motions. II - Models of vertical motion. *Astrophysical Journal*, 237:1024–1042.

Keller, C. U. (1995). Properties of Solar Magnetic Fields from Speckle Polarimetry. (Ludwig Biermann Award Lecture 1994). *Reviews of Modern Astronomy*, 8:27–60.

Kendrick, R. L., Acton, D. S., and Duncan, A. L. (1994). Phase-diversity wavefront sensor for imaging systems. *Applied Optics*, 33:6533–6546.

Kentischer, T. J., Schmidt, W., Sigwarth, M., and Uexkuell, M. V. (1998). TESOS, a double Fabry-Perot instrument for solar spectroscopy. *Astronomy and Astrophysics*, 340:569–578.

Kerr, R. M. (1996). Rayleigh numberscaling in numerical convection. *Journal of Fluid Mechanics*, 310:139–179.

Kippenhahn, R. and Weigert, A. (1994). *Stellar Structure and Evolution.* Springer-Verlag Berlin Heidelberg New York. Also Astronomy and Astrophysics Library.

Kitai, R. and Kawaguchi, I. (1979). Morphological study of the solar granulation. I - Dark dot formation in the cell. *Solar Physics*, 64:3–12.

Kosovichev, A. G. and Duvall, T. L. (1997). Acoustic tomography of solar convective flows and structures. In *ASSL Vol. 225: SCORe'96 : Solar Convection and Oscillations and their Relationship*, pages 241–260.

Kosovichev, A. G., Duvall, T. L., Birch, A. C., Gizon, L., Scherrer, P. H., and Zhao, J. (2001). Heliotomography of the outer layers of the Sun. In *ESA SP-464: SOHO 10/GONG 2000 Workshop: Helio- and Asteroseismology at the Dawn of the Millennium*, pages 701–706.

Koutchmy, S. and Lebecq, C. (1986). The solar granulation. II - Photographic and photoelectric analysis of photospheric intensity fluctuations at the mesogranulation scale. *Astronomy and Astrophysics*, 169:323–328.

Krieg, J., Kneer, F., Koschinsky, M., and Ritter, C. (2000). Granular velocities of the Sun from speckle interferometry. *Astronomy and Astrophysics*, 360:1157–1162.

Küveler, G. (1983). Velocity fields of individual supergranules. *Solar Physics*, 88:13–29.

Löfdahl, M. G., Berger, T. E., and Seldin, J. H. (2001). Two dual-wavelength sequences of high-resolution solar photospheric images captured over several hours and restored by use of phase diversity. *Astronomy and Astrophysics*, 377:1128–1135.

Löfdahl, M. G. and Scharmer, G. B. (1993). Phase-Diversity Restoration of Solar Images. In *Real time and post facto solar image correction, proc. 13th NSO/Sac Peak Summer Workshop, NSO/SP summer workshop series No. 13, ed. Richard R. Radick, pp. 89-104*, pages 89–104.

Löfdahl, M. G. and Scharmer, G. B. (1994). Wavefront sensing and image restoration from focused and defocused solar images. *Astronomy and Astrophysics Supplement*, 107:243–264.

Löfdahl, M. G., Scharmer, G. B., and Wei, W. (2000). Calibration of a deformable mirror and Strehl ratio measurements by use of phase diversity. *Applied Optics*, 39:94–103.

Lawrence, J. K., Cadavid, A. C., and Ruzmaikin, A. (2001). Mesogranulation and Turbulence in Photospheric Flows. *Solar Physics*, 202:27–39.

Lee, D. J., Roggemann, M. C., and Welsh, B. M. (1999). CramerRao analysis of phase-diverse wave-front sensing. *Optical Society of America Journal*, 16:1005–1015.

Lee, D. J., Welsh, B. M., Roggemann, M. C., and Ellerbroek, B. L. (1997). Diagnosing unknown aberrationsin an adaptive optics system by use of phase diversity. *Optics Letters*, 22:952–954.

Leibacher, J. and Stein, R. F. (1970). A New Description of the Solar Five-Minute Oscillation. *Astrophysical Letters*, 7:191.

Leighton, R. B. (1963). The Solar Granulation. *Annual Review of Astronomy and Astrophysics*, 1:19.

Leighton, R. B., Noyes, R. W., and Simon, G. W. (1962). Velocity Fields in the Solar Atmosphere. I. Preliminary Report. *Astrophysical Journal*, 135:474.

Libchaber, A. (1987). Quasiperidic transition to chaos. *Proceedings of the Royal Society of London (A)*, 413:63.

Lindsey, C., Braun, D., Jefferies, S., Fan, Y., Gu, Y., and Redfield, S. (1996). Doppler Acoustic Diagnostics of Subsurface Solar Magnetic Structure. *Bulletin of the American Astronomical Society*, 28:955.

Lisle, J., De Rosa, M., and Toomre, J. (2000). New Approach to Study Extended Evolution of Supergranular Flows and Their Advection of Magnetic Elements. *Solar Physics*, 197:21–30.

Lites, B. W. (2001). Space-Based Instrumentation for Inference of the Solar Magnetic Field. In *ASP Conf. Ser. 248: Magnetic Fields Across the Hertzsprung-Russell Diagram*, page 553.

Lites, B. W., Rutten, R. J., and Berger, T. E. (1999). Dynamics of the Solar Chromosphere. II. Ca II H_2V and K_2V Grains versus Internetwork Fields. *Astrophysical Journal*, 517:1013–1033.

Loughhead, R. E., Bray, R. J., and Brown, N. (1978). Instrumental profile of a triple Fabry-Perot interferometer for use in solar spectroscopy. *Applied Optics*, 17:415–419.

Ludwig, H., Freytag, B., and Steffen, M. (1999). A calibration of the mixing-length for solar-type stars based on hydrodynamical simulations. I. Methodical aspects and results for solar metallicity. *Astronomy and Astrophysics*, 346:111–124.

Lyot, B. (1944). Le filtre monochromatique polarisant et ses applications en physique solaire. *Annales d'Astrophysique*, 7:31.

Müller, D. A. N., Steiner, O., Schlichenmaier, R., and Brandt, P. N. (2001). Time-slice diagrams of solar granulation. *Solar Physics*, 203:211–232.

Macris, C. (1953). Recherches sur la granulation photosphérique. *Annales d'Astrophysique*, 16:19.

Marr, D. (1982). *Vision.* W.H.Freeman and Company.

Mehltretter, J. P. (1978). Balloon-borne imagery of the solar granulation. II - The lifetime of solar granulation. *Astronomy and Astrophysics*, 62:311–316.

Mein, P. (1971). Inhomogeneities in the Solar Atmosphere from the Ca II Infra-Red Lines. *Solar Physics*, 20:3.

Meynadier, L., Michau, V., Velluet, M., Conan, J., Mugnier, L. M., and Rousset, G. (1999). Noise Propagation in Wave-Front Sensing with Phase Diversity. *Applied Optics*, 38:4967–4979.

Miller, P., Foukal, P., and Keil, S. (1984). On the interpretation of Fraunhofer line Doppler shifts at supergranule boundaries. *Solar Physics*, 92:33–46.

Muller, R. (1985). . *Solar Physics*, 100:237.

Muller, R., Auffret, H., Roudier, T., Vigneau, J., Simon, G. W., Frank, Z., Shine, R. A., and Title, A. M. (1992). Evolution and advection of solar mesogranulation. *Nature*, 356:322–325.

Muller, R. and Roudier, T. (1984). The fine structure of the quiet sun. *Solar Physics*, 94:33.

Muller, R., Roudier, T., and Vigneau, J. (1990). The large-scale pattern formed by the spatial distribution of granules. *Solar Physics*, 126:53–67.

Munk, W. and Wunsch, C. (1979). *Ocean acoustic tomography: A scheme for large scale monitoring*, volume 26A. Deep Sea Res.

Musman, S. and Rust, D. M. (1970). Vertical Velocities and Horizontal Wave Propagation in the Solar Photosphere. *Solar Physics*, 13:261.

Namba, O. (1986). Evolution of 'exploding granules'. *Astronomy and Astrophysics*, 161:31–38.

Namba, O. and Diemel, W. E. (1969). A Morphological Study of the Solar Granulation. *Solar Physics*, 7:167.

Nesis, A., Hammer, R., Hanslmeier, A., Schleicher, H., Sigwarth, M., and Staiger, J. (1997). Dynamics of the solar granulation. IV. Granular shear flow. *Astronomy and Astrophysics*, 326:851–859.

Nesis, A., Hammer, R., Roth, M., and Schleicher, H. (2001). Dynamics of the solar granulation. VII. A nonlinear approach. *Astronomy and Astrophysics*, 373:307–317.

Nesis, A., Hanslmeier, A., Hammer, R., Komm, R., Mattig, W., and Staiger, J. (1992). Dynamics of the solar granulation. I - A phenomenological approach. *Astronomy and Astrophysics*, 253:561–566.

Nesis, A., Hanslmeier, A., Hammer, R., Komm, R., Mattig, W., and Staiger, J. (1993). Dynamics of the solar granulation. 2: A quantitative approach. *Astronomy and Astrophysics*, 279:599–609.

Nicolis, G. (1989). Physics of far-from-equilibrium systems and self organization. In Davies, P., editor, *The New Physics*, pages 316–347. Cambridge University Press, New York, NY, USA.

Noll, R. J. (1976). Zernike polynomials and atmospheric turbulence. *Optical Society of America Journal*, 66:207–211.

Nordlund, Å., Spruit, H. C., Ludwig, H. G., and Trampedach, R. (1997). Is stellar granulation turbulence? *Astronomy and Astrophysics*, 328:229–234.

Nordlund, Å. and Stein, R. (1995). Convection; significance for stellar structure and evolution. In Noels, A., Fraipont-Caro, D., Gabriel, M., Grevesse, N., and Demarque, P., editors, *Stellar Evolution: What Should be Done, Proceedings of the 32nd Lige International Astrophysical Colloquium*, page 75, Liege, Belgium.

November, L. J. (1986). Precise Proper Motion Measurement of Solar Granulation. *Bulletin of the American Astronomical Society*, 18:932.

November, L. J. (1989). Proper motion measurements of solar granulation: the case for mesogranulation. In *High spatial resolution solar observations*, page 457.

November, L. J. (1994). Inferring the depth extent of the horizontal supergranular flow. *Solar Physics*, 154:1–17.

November, L. J. and Simon, G. W. (1988). Precise proper-motion measurement of solar granulation. *Astrophysical Journal*, 333:427–442.

November, L. J., Simon, G. W., Tarbell, T. D., Title, A. M., and Ferguson, S. H. (1987). Large-scale horizontal flows from SOUP observations of solar granulation. In *Theoretical Problems in High Resolution Solar Physics*, pages 121–127.

November, L. J., Toomre, J., Gebbie, K. B., and Simon, G. W. (1981). The detection of mesogranulation on the sun. *Astrophysical Journal*, 245:L123–L126.

November, L. J., Toomre, J., Gebbie, K. B., and Simon, G. W. (1982). Vertical flows of supergranular and mesogranular scale observed on the sun with OSO 8. *Astrophysical Journal*, 258:846–859.

Oda, N. (1984). Morphological study of the solar granulation. III - The mesogranulation. *Solar Physics*, 93:243–255.

Palmieri, R., Piotto, G., Saviane, I., Girardi, L., and Castellani, V. (2002). Does the mixing length parameter depend on metallicity?. Further tests of evolutionary sequences using homogeneous databases. *Astronomy and Astrophysics*, 392:115–129.

Parker, R. L. (1977). Understanding inverse theory. *Annual Review of Earth and Planetary Sciences*, 2:35–64.

Paxman, R. G. and Seldin, J. H. (1993). Fine-resolution astronomical imaging with phase-diverse speckle. In Paul, S. I., editor, *Proc. SPIE Vol. 2029, Digital Image Recovery and Synthesis II*, pages 287–298.

Paxman, R. G., Seldin, J. H., Loefdahl, M. G., Scharmer, G. B., and Keller, C. U. (1996). Evaluation of Phase-Diversity Techniques for Solar-Image Restoration. *Astrophysical Journal*, 466:1087.

Pearson, F. I. (1990). *Map Projections: Theory and Applications.* CRC Press, Boca Raton, FL, USA.

Pearson, J. R. A. (1958). On convection cells induced by surface tension. *Journal of Fluid Mechanics*, 4:489–500.

Penza, V., Caccin, B., and Del Moro, D. (2004). The sensitivity of the C I 538.0 nm Fe I 537.9 nm and Ti II 538.1 nm lines to solar active regions. *Astronomy and Astrophysics*, 427:345–351.

Plaskett, H. H. (1954). Motions in the Sun at the photospheric level. V. Velocities of granules and of other localized regions. *Monthly Notices of the Royal Astronomical Society*, 114:251.

Ploner, S. R. O., Solanki, S. K., and Gadun, A. S. (2000). Is solar mesogranulation a surface phenomenon? *Astronomy and Astrophysics*, 356:1050–1054.

Prigogine, I. and Kondepudi, D. (2002). *Termodinamica: dalle macchine termiche alle strutture dissipative.* Bollati-Boringhieri.

Qu, Z. Q. and Xu, Z. (2002). Key properties of solar chrmospheric line formation process. *Chinese Journal of Astronomy and Astrophysics*, 2(1):71–80.

Rösch, J. (1959). Observations sur la photosphère solaire: II. Numération et photométrie photographique des granules dans le domaine spectral 5 900-6 000 Å. *Annales d'Astrophysique*, 22:584.

Rösch, J. and Hugon, M. (1959). Sur l'Evolution dans le Temps de la Granulation Photosphérique. *Academie des Science Paris Comptes Rendus Serie B Sciences Physiques*, 249:625–627.

Raju, K. P., Srikanth, R., and Singh, J. (1999). Lifetimes and sizes of supergranular cells. *Bulletin of the Astronomical Society of India*, 27:65.

Rast, M., Ermolli, I., Sands, J., and Berrilli, F. (2002). The supergranular intensity contrast. In *COSPAR, Plenary Meeting.*

Rast, M. P. (1991). High Wavenumber Thermal Convection Enhanced in Regions of Partial Ionization. *Lecture Notes in Physics, Berlin Springer Verlag*, 388:179.

Rast, M. P. (1995). On the nature of 'exploding' granules and granule fragmentation. *Astrophysical Journal*, 443:863–868.

Rast, M. P. (1999). Thermal starting plumes, solar granulation, and the excitation of solar acoustic oscillations. In Rimmele, T. R., Balasubramaniam, K. S., and Radick, R. R., editors, *High Resolution Solar Physics: Theory, Observations, and Techniques, ASP Conference Series 183*, page 443.

Rast, M. P. (2002). A comment on 'Regular structures of the solar photosphere'. *Astronomy and Astrophysics*, 392:L13–L15.

Rast, M. P. (2003a). Supergranulation: new observation, possible explanation. In *ESA SP-517: GONG+ 2002. Local and Global Helioseismology: the Present and Future*, pages 163–172.

Rast, M. P. (2003b). The Scales of Granulation, Mesogranulation, and Supergranulation. *Astrophysical Journal*, 597:1200–1210.

Rast, M. P., Lisle, J. P., and Toomre, J. (2004). The Spectrum of the Solar Supergranulation: Multiple Nonwave Components. *Astrophysical Journal*, 608:1156–1166.

Reardon, K. and Cavallini, A. (2003). Characterization of the IBIS Tra mission Profile. *Memorie della Societá Astronomica Italiana*, 74:815–818.

Restaino, S. R. (1992). Wavefront Sensing and Image Deconvolution of Solar Data. *Applied Optics*, 31:7442–7449.

Richardson, R. S. and Schwarzchild, M. (1950). On the Turbulent Velocities of Solar Granules. *Astrophysical Journal*, 111:351.

Rieutord, M., Roudier, T., Ludwig, H.-G., Nordlund, Å., and Stein, R. (2001). Are granules good tracers of solar surface velocity fields? *Astronomy and Astrophysics*, 377:L14–L17.

Rieutord, M., Roudier, T., Malherbe, J. M., and Rincon, F. (2000). On mesogranulation, network formation and supergranulation. *Astronomy and Astrophysics*, 357:1063–1072.

Rimmele, T. and Schroeter, E. H. (1989). The variation of the cell size and velocities of the supergranulation with heliographic latitude. *Astronomy and Astrophysics*, 221:137–145.

Roudier, T., Lignières, F., Rieutord, M., Brandt, P. N., and Malherbe, J. M. (2003). Families of fragmenting granules and their relation to meso- and supergranular flow fields. *Astronomy and Astrophysics*, 409:299–308.

Roudier, T., Malherbe, J. M., Vigneau, J., and Pfeiffer, B. (1998). Solar mesogranule lifetime measurements. *Astrophysical Journal*, 330:1136–1144.

Roudier, T. and Muller, R. (1987). Structure of the solar granulation. *Solar Physics*, 107:11–26.

Roudier, T., Rieutord, M., Malherbe, J. M., and Vigneau, J. (1999). Determination of horizontal velocity fields at the sun's surface with high spatial and temporal resolution. *Astronomy and Astrophysics*, 349:301–311.

Ruiz Cobo, B. and del Toro Iniesta, J. C. (1992). Inversion of Stokes profiles. *Astrophysical Journal*, 398:375–385.

Sánchez Almeida, J., Márquez, I., Bonet, J. A., Domínguez Cerdeña, I., and Muller, R. (2004). Bright Points in the Internetwork Quiet Sun. *Astrophysical Journal Letters*, 609:L91–L94.

Sýkora, J. (1970). Time and Shape Changes of the Supergranular Network. *Solar Physics*, 13:292.

Sanchez Almeida, J., Landi degl'Innocenti, E., Martinez Pillet, V., and Lites, B. W. (1996a). Line Asymmetries and the Microstructure of Photospheric Magnetic Fields. *Astrophysical Journal*, 466:537.

Sanchez Almeida, J., Ruiz Cobo, B., and del Toro Iniesta, J. C. (1996b). Heights of formation for measurements of atmospheric parameters. *Astronomy and Astrophysics*, 314:295–302.

Scharmer, G. B., Bjelksjo, K., Korhonen, T. K., Lindberg, B., and Petterson, B. (2003). The 1-meter Swedish solar telescope. In *Innovative Telescopes and Instrumentation for Solar Astrophysics. Edited by Stephen L. Keil, Sergey V. Avakyan . Proceedings of the SPIE, Volume 4853, pp. 341-350 (2003).*, pages 341–350.

Scharmer, G. B., Gudiksen, B. V., Kiselman, D., Löfdahl, M. G., and Rouppe van der Voort, L. H. M. (2002). Dark cores in sunspot penumbral filaments. *Nature*, 420:151–153.

Scherrer, P. H., Bogart, R. S., Bush, R. I., Hoeksema, J. T., Kosovichev, A. G., Schou, J., Rosenberg, W., Springer, L., Tarbell, T. D., Title, A., Wolfson, C. J., Zayer, I., and MDI Engineering Team (1995). The Solar Oscillations Investigation - Michelson Doppler Imager. *Solar Physics*, 162:129–188.

Schrijver, C. J., Hagenaar, H. J., and Title, A. M. (1997). On the Patterns of the Solar Granulation and Supergranulation. *Astrophysical Journal*, 475:328.

Schüssler, M. (2002). *Solar Convection & Magnetism Lectures.* Max Planck Institut für Aeronomie, Katlenburg, Lindau, Germany.

Secchi, A. (1870). *Le Soleil.* Paris : Gauthier-Villars, 1870.

Seldin, J. H. and Paxman, R. G. (1994). Phase-Diverse Speckle Reconstruction of Solar Data. In *Image Reconstruction and Restoration, Proc. Soc. Photo-Opt. Instrum. Eng., SPIE 2302*, page 268.

Seldin, J. H., Paxman, R. G., Zarifis, V. G., Benson, L., and Stone, R. E. (2000). Closed-loop wavefront sensing for a sparse-aperture multitelescope array using broadband phase diversity. In *Proc. SPIE Vol. 4091, p. 48-63, Imaging Technology and Telescopes, James W. Bilbro; James B. Breckinridge; Richard A. Carreras; Stanley R. Czyzak; Mark J. Eckart; Robert D. Fiete; Paul S. Idell; Eds.*, pages 48–63.

Shannon, C. E. (1948). A mathematical theory of communication. *The Bell System Technical Journal*, 27:379–423.

Shannon, C. E. and Weaver, W. (1949). *The mathematical theory of communication.* University of Illinois Press.

Shchukina, N. G., Bueno, J. T., and Kostik, R. I. (1997). The NLTE Formation of Iron Lines Used in Solar Polarimetry. *Solar Physics*, 172:117–124.

Shine, R. A., Simon, G. W., and Hurlburt, N. E. (2000). Supergranule and Mesogranule Evolution. *Solar Physics*, 193:313–331.

Siggia, E. D. (1994). High Rayleigh Number Convection. *Annual Review of Fluid Mechanics*, 26:137–168.

Simon, G. W. and Leighton, R. B. (1964). Velocity Fields in the Solar Atmosphere. III. Large-Scale Motions, the Chromospheric Network, and Magnetic Fields. *Astrophysical Journal*, 140:1120.

Simon, G. W., Title, A. M., Topka, K. P., Tarbell, T. D., Shine, R. A., Ferguson, S. H., Zirin, H., and SOUP Team (1988). On the relation between photospheric flow fields and the magnetic field distribution on the solar surface. *Astrophysical Journal*, 327:964–967.

Simon, G. W., Title, A. M., and Weiss, N. O. (1995). Kinematic models of supergranular diffusion on the Sun. *Astrophysical Journal*, 442:886–897.

Simon, W. G. (1967). Observations of Horizontal Motions in Solar Granulation: Their Relation to Supergranulation. *Zeitschrift fur Astrophysics*, 65:345.

Singh, J. and Bappu, M. K. V. (1981). A dependence on solar cycle of the size of the Ca^{+} network. *Solar Physics*, 71:161–168.

Skumanich, A., Smythe, C., and Frazier, E. N. (1975a). On the statistical description of inhomogeneities in the quiet solar atmosphere. I - Linear regression analysis and absolute calibration of multichannel observations of the Ca II emission network. *Astrophysical Journal*, 200:747–764.

Skumanich, A., Smythe, C., and Frazier, E. N. (1975b). On the statistical description of inhomogeneities in the quiet solar atmosphere. I - Linear regression analysis and absolute calibration of multichannel observations of the Ca/+/ emission network. *Astrophysical Journal*, 200:747–764.

Snodgrass, H. B. and Ulrich, R. K. (1990). Rotation of Doppler features in the solar photosphere. *Astrophysical Journal*, 351:309–316.

Sobotka, M., Vázquez, M., Bonet, J. A., Hanslmeier, A., and Hirzberger, J. (1999). Temporal Evolution of Fine Structures in and around Solar Pores. *Astrophysical Journal*, 511:436–450.

Solanki, S. K. and Stenflo, J. O. (1984). Properties of solar magnetic fluxtubes as revealed by Fe I lines. *Astronomy and Astrophysics*, 140:185–198.

Spruit, H. C. (1981). Motion of magnetic flux tubes in the solar convection zone and chromosphere. *Astronomy and Astrophysics*, 98:155–160.

Spruit, H. C. (1997). Convection in stellar envelopes: a changing paradigm. *Memorie della Societá Astronomia Italiana*, 68:397–414.

Spruit, H. C., Nordlund, Å., and Title, A. M. (1990). Solar convection. *Annual Review of Astronomy and Astrophysics*, 28:263–303.

Srikanth, R., Singh, J., and Raju, K. P. (2000). Distribution of Supergranular Sizes. *Astrophysical Journal*, 534:1008–1019.

Starck, J. L., Murtagh, F., and Bijaoui, A. (1998). *Image Processing and Data Analysis: The Multiscale Approach.* Cambridge University Press, Cambridge.

Stein, R. F. and Nordlund, Å. (1989). Topology of convection beneath the solar surface. *Astrophysical Journal Letters*, 342:L95–L98.

Steiner, O., Bruls, J., and Hauschildt, P. H. (2001). Why are G-Band Bright Points Bright? In *ASP Conf. Ser. 236: Advanced Solar Polarimetry – Theory, Observation, and Instrumentation*, page 453.

Stenflo, J. O. and Harvey, J. W. (1985). Dependence of the properties of magnetic fluxtubes on area factor or amount of flux. *Solar Physics*, 95:99–118.

Stenflo, J. O., Solanki, S., Harvey, J. W., and Brault, J. W. (1984). Diagnostics of solar magnetic fluxtubes using a Fourier transform spectrometer. *Astronomy and Astrophysics*, 131:333–346.

Straus, T. and Bonaccini, D. (1997). Dynamics of the solar photosphere. I. Two-dimensional spectroscopy of mesoscale phenomena. *Astronomy and Astrophysics*, 324:704–712.

Straus, T., Deubner, F.-L., and Fleck, B. (1992). Is mesogranulation a distinct regime of convection? *Astronomy and Astrophysics*, 256:652–659.

Strous, L. H. (1995). Feature Tracking: Deriving Horizontal Motion and More. In Hoeksema, J. T., Domingo, V., Fleck, B., and Battrick, B., editors, *Helioseismology. ESA SP, Proceedings of the 4th Soho Workshop, held Pacific Grove, California, USA, 2-6 April 1995*, page 213P.

Stuart, F. E. and Rush, J. H. (1954). Correlation Analyses of Turbulent Velocities and Brightness of the Photospheric Granulation. *Astrophysical Journal*, 120:245.

Thelen, B. J., Paxman, R. G., Carrara, D. A., and Seldin, J. H. (1999). Maximum a posteriori estimation of fixed aberrations, dynamic aberrations, and the object from phase-diverse speckle data. *Optical Society of America Journal*, 16:1016–1025.

Tindle, C. T. and Guthrie, K. M. (1974). Rays as interfering modes in underwater acoustics. *Journal of Sound and Vibration*, 34(2):291–5.

Title, A. M., Tarbell, T. D., Topka, K. P., Ferguson, S. H., Shine, R. A., and SOUP Team (1989). Statistical properties of solar granulation derived from the SOUP instrument on Spacelab 2. *Astrophysical Journal*, 336:475–494.

Torquato, S. and Stillinger, F. H. (2002). Controlling the short-range order and packing densities of many-particle systems. *Journal of Physical Chemistry B*, 106 (33):8354–8359.

Tritschler, A., Schmidt, W., Langhans, K., and Kentischer, T. (2002). High-resolution solar spectroscopy with TESOS - Upgrade from a double to a triple system. *Solar Physics*, 211:17–29.

Ueno, S. and Kitai, R. (1998a). 3D Velocity-Field Observation of Solar Convection I. Characteristics of Mesogranulation. *Publications of the Astronomical Society of Japan*, 50:125–139.

Ueno, S. and Kitai, R. (1998b). Observational relationship between meso-sized convection and 5-min oscillation in the solar atmosphere. In *IAU Symp. 185: New Eyes to See Inside the Sun and Stars*, page 457.

Ulrich, R. K. (1970). The Five-Minute Oscillations on the Solar Surface. *Astrophysical Journal*, 162:993.

Unsöld, A. (1930). Konvektion in der Sonnenatmosphäre. *Zeitschrift für Astrophysik*, 1:138.

van Ballegooijen, A. A. and Nisenson, P. (2002). High-Resolution Imaging of the Solar Photosphere Using Simultaneous G-Band and Continuum Observations. *Bulletin of the American Astronomical Society*, 34:698.

van Siclen, C. (1997). Information entropy of complex structures. *Physical Reviews E*, 56:5211.

Venkatakrishnan, P. (1984). Convection and the Phenomenon of Kilogausss Magnetic Fields on the Sun. *Kodaikanal Observatory Bulletins*, 4:19–24.

Vitense, E. (1953). Die Wasserstoffkonvektionszone der Sonne. Mit 11 Textabbildungen. *Zeitschrift fur Astrophysics*, 32:135.

Wang, H. (1989). Do mesogranules exist? *Solar Physics*, 123:21–32.

Wang, H., Tang, F., Zirin, H., and Wang, J. (1996). The Velocities of Intranetwork and Network Magnetic Fields. *Solar Physics*, 165:223–235.

Wang, H. and Zirin, H. (1989). Study of supergranules. *Solar Physics*, 120:1–17.

Wang, Y., Noyes, R. W., Tarbell, T. D., and Title, A. M. (1995). Vorticity and Divergence in the Solar Photosphere. *Astrophysical Journal*, 447:419.

Wilken, V., de Boer, C. R., Denker, C., and Kneer, F. (1997). Speckle measurements of the centre-to-limb variation of the solar granulation. *Astronomy and Astrophysics*, 325:819–824.

Williams, G. and Watts, D. C. (1970). Non-symmetrical dielectric relaxation behavior arising from a simple empirical decay function. *Transaction of the Faraday Society*, 66:80.

Worden, S. P. and Simon, G. W. (1976). A study of supergranulation using a diode array magnetograph. *Solar Physics*, 46:73–91.

Zhang, H., Scharmer, G., Lofdahl, M., and Yi, Z. (1998a). Fine Structures of Magnetic Field in Solar Quiet Region. *Solar Physics*, 183:283–290.

Zhang, J., Lin, G., Wang, J., Wang, H., and Zirin, H. (1998b). The evolution of intranetwork magnetic elements. *Astronomy and Astrophysics*, 338:322–328.

Zhang, T. Y. and Suen, C. Y. (1984). A fast parallel algorithm for thinning digital patterns. *Communications of the ACM*, 27(3):236–239.

Zhao, J. and Kosovichev, A. G. (2003). On the inference of supergranular flows by time-distance helioseismology. In *ESA SP-517: GONG+ 2002. Local and Global Helioseismology: the Present and Future*, pages 417–420.

Ziman, J. M. (1979). *Models of Disorder.* Cambridge University Press, Cambridge.